ESTIMATING GLACIER ICE THICKNESS AND MASS BALANCE USING MULTIPLE SPACEBORNE GEODETIC TECHNIQUES

A Dissertation

Presented to

the Faculty of the Department of Civil and Environmental Engineering

University of Houston

In Partial Fulfillment

of the Requirements for the Degree

Doctor of Philosophy

in Geosensing Systems Engineering and Sciences

by

Zhiyue Sun

May 2019

ESTIMATING GLACIER ICE THICKNESS AND MASS BALANCE USING

MULTIPLE SPACEBORNE GEODETIC TECHNIQUES

Zhiyue Sun

Approved:

Chair of the Committee
Hyongki Lee, Ph.D.
Associate Professor
Civil & Environmental Engineering

Committee Members:

Ramesh L. Shrestha, Ph.D.
Hugh Roy & Lillie Cranz Cullen
Distinguished Professor
Civil & Environmental Engineering

Craig L. Glennie, Ph.D.
Associate Professor
Civil & Environmental Engineering

Yushin. Ahn, Ph.D.
Assistant Professor
Geomatics Engineering
California State University, Fresno, CA

Alexander. Braun, Ph.D.
Professor
Geological Sciences and Geological Engineering
Queen's University, Kingston, Canada

Suresh K. Khator, Ph.D.
Associate Dean
Cullen College of Engineering

Craig L. Glennie, Ph.D.
Geosensing Systems Engineering &
Science Program Director

ESTIMATING GLACIER ICE THICKNESS AND MASS BALANCE USING MULTIPLE SPACEBORNE GEODETIC TECHNIQUES

An Abstract

of a

Dissertation

Presented to

the Faculty of the Department of Civil and Environmental Engineering

University of Houston

In Partial Fulfillment

of the Requirements for the Degree

Doctor of Philosophy

in Geosensing Systems Engineering and Sciences

by

Zhiyue Sun

May 2019

Abstract

The melting of glaciers and ice caps makes a significant contribution to present-day sea level rise. Recently, multiple space-borne remote sensing techniques have been successfully used to obtain geodetic observations, which were used to estimate the contribution of global glacier melt to sea level rise. However, estimates from different approaches yield large discrepancies in certain glacierized areas such as the Eastern Nyainqen Tanglha. Moreover, other glacierized regions such as the Novaya Zemlya in the Russian Arctic have been under-studied. Therefore, to characterize and quantify accurate glacier mass balance estimates over Eastern Nyainqen Tanglha and Novaya Zemlya, an iterative velocity-based method is proposed to estimate glacier thickness.

First, a new iterative method is presented, which estimates ice thickness using surface velocity and surface topography. The temperature-related rate factor for temperate glaciers is empirically obtained based on multiple in-situ measurements, while the rate factor for non-temperate glaciers follows the assumption made by previous studies. A validation was performed with 15 previous methods over 8 glaciers. Based on the comparative results, the proposed method in glacierized areas where direct observations are limited is promising.

Second, multiple traditional spaceborne techniques for observing surface mass balance were tested in the Novaya Zemlya. The mass variation trend was obtained based on observations from Gravity Recovery and Climate Experiment (GRACE) and radar altimeter over 4 selected glaciers. The glacier outflow and influx were also determined using surface velocity and snowfall observations. Additionally, the contributions of outflow and influx to mass change for Novaya Zemlya were identified.

Finally, the proposed thickness estimate method is applied to 4 largest glaciers in Nyainqen Tanglha. Surface velocity estimates were calculated from Advanced Land Observing Satellite (ALOS)/ALOS-2 Phased Array type L-band SAR (PALSAR) image pairs via speckle matching. Surface slope distribution was calculated from the Advanced Spaceborne Thermal Emission and Reflection Radiometer (ASTER) Digital Elevation Model (DEM) data. Consequently, the thickness distribution map from 2008 to 2016 was obtained. Furthermore, the mass balance and thickness changes were determined. These estimates have an agreement with previous ones from GRACE and ASTER DEM differencing approaches.

TABLE OF CONTENTS

LIST OF FIGURES

LIST OF TABLES

1 Introduction

Glacial ice, as the largest freshwater store, covers approximately 10 percent of the land surface at present; this number was triple during the ice ages (*Paterson*, 2010). Based on the location of the terminus, glaciers can be classified into land-terminating and marine-terminating glaciers. Land-terminating glaciers are considered as key indicators of regional climate change (*Barry*, 2006). In addition, land-terminating glaciers often play an important role as supplying water to human inhabitants. In High Mountain Asia (HMA) region, 45% of the total river flow in Indus, Ganges and Brahmaputra Rivers comes from the spring glacier melt (*Kehrwald et al.*, 2008). Recently, the contribution of glacier mass loss due to global warming to sea level rise has been highlighted (*Meier et al.*, 2007; *Pfeffer et al.*, 2008). Despite discrepancies among different estimates, the impact of glacier melt on sea level rise has been clearly identified (*Gardner et al.*, 2013; *Jacob et al.*, 2012).

Typically, in-situ measurements for glacial study are limited or not publicly available (*Gao and Liu*, 2001). Recently, space-borne remote sensing techniques, such as satellite radar/laser altimetry, Gravity Recovery and Climate Experiment (GRACE), Synthetic Aperture Radar (SAR)/optical sensing, have been successfully used to provide contemporary observations of elevation changes, mass changes, and ice flow velocities with better temporal and spatial coverages. This dissertation aims at quantifying and characterizing glacier thickness changes and mass balance over two relatively under-studied glacierized areas, Novaya Zemlya in Russian Arctic and Nyainqen Tanglha in Himalaya using multiple space-borne geodetic techniques.

1.1 Backgrounds

1.1.1 Glacier Studies Using In-Situ Measurements

Measuring glaciers began in the 1830s in the Alps and aimed at determining glacier surface velocity (*Paterson*, 2010). *Agassiz* (1840) collected these observations and claimed that glacier's speed was fastest in the central part and decreased rapidly towards the edges. The surface velocity at the head and terminus were also discovered to be smaller than elsewhere (*Paterson*, 2010). *Finsterwalder* (1897a) observed the seasonal change of surface velocity in Me de Glace, France. This study was also a pioneer in developing the photogrammetric method for mapping glaciers (*Finsterwalder*, 1897b). In the early 1900s, the first attempt to measure ice velocity beneath the surface was made by Blumcke and Hess (*Hughes and Seligman*, 1939). Eleven holes were drilled to bedrock of a glacier in the Tyrol, Austria using a thermal drill. The basal velocity was discovered to be much smaller than the surface velocity. Then, people started to explore other regions outside the Alps. In 1930, Koch and Wegener first obtained ice temperature measurements in Greenland at a depth of 24 m (*Loewe*, 1935). The ice thickness was also measured using a seismic method. The relationship between climate change and glacier melt became an emerging area of studies, and *Ahlmann* (1919, 1935, 1949) investigated glaciers in Scandinavia, Spitsbergen, Iceland and Greenland to identify the reaction of glacier melting to climate change. *Nye* (1952) first noted the relationship between ice thickness and basal stress, and *Glen* (1959) prepared a model for it, known as the "Glen's flow law" (*Glen*, 1959). This model is still regarded as one of the fundamental principles in glacial mechanics (*Hooke*, 2005; *Van der Veen*, 2013). In the 1960s, the first computational model

for simulating glacial accumulation and ablation processes was developed (*Anderson*, 1972; *Crawford*, 1973). This early attempt provided glacier melt water inputs for watershed models (*Anderson*, 1973; *Brun et al*., 1989; *Braun et al*., 1994). Growing concern for global warming have led to studies focusing on exploring the contribution of glacier melt to sea level rise (*Braithwaite and Olesen*, 1990; *Braithwaite and Zhang*, 1999; *Oerlemans and Fortuin*, 1992).

This brief historical review indicates that traditional glaciological research has focused on specific glaciers where in-situ measurements are available. Based on these observations, physical models have been calibrated and validated accordingly (*Van der Veen*, 2013). However, the lack of in-situ data limits the comprehensive understanding of glaciers (*Hock*, 2005). After the 1990s, space-borne remote sensing techniques provided various glacial observations such as mass balance, volumes, boundaries, and temperatures with higher spatial and temporal resolutions (*Cogley*, 2012, 2009; *Gardelle et al.*, 2012; *Gardner et al.*, 2013; *Jacob et al.*, 2012).

1.1.2 Remote Sensing of Glaciers

Remote sensing of glaciers began with the launch of the Earth Resource Technology Satellite (renamed Landsat) in the 1970s (*Gao and Liu*, 2001). However, only a few studies were carried out until the 1990s after several review papers had been published between 1987 and 1990 (*Knight*, 1992). Most of the early remote sensing techniques for glaciers were based on visible/near infrared (VNIR) sensors. For example, aerial photographs taken from VNIR cameras were used for the delineation of glacier tongues, glacial terminus and the snow lines (*Dowdeswell*, 1986; *Espizua*, 2010; *Krimmel and Meier*, 1975). Landsat images with better spatial and temporal coverages were also

been used to generate global glacial outlines (*MacDonald*, 1976; *Williams et al.*, 1975). Recently, a co-registration based approach known as "feature tracking" with Landsat or other optical image pairs has been widely used to obtain surface velocity (*Ahn and Howat*, 2011; *Erten et al*., 2009; *Joughin et al.*, 2004, 2010).

Other space-based remote sensing techniques have been also used to obtain different surface measurements such as surface velocity, surface elevation, thickness, and mass balance. Recently, interferometric Synthetic Aperture Radar (InSAR) technique have been successfully used to estimate glacier velocities with m-level accuracy for annual velocity, especially after the launch of ERS-1/2 tandem mission (*Goldstein et al.*, 1993; *Joughin et al.*, 1996; *Rignot*, 1997; *Mohr et al.*, 1998). However, it has poor performance over fast-moving glaciers due to decorrelation (*Strozzi et al.*, 2002). The so-called speckle matching (or intensity offset-tracking) has been studied based on a similar co-registration approach to the feature-tracking technique (*Joughin*, 2002; *Strozzi et al.*, 2008). Since it uses the intensity images, speckle matching can be applied to fast-moving glaciers with an accuracy of approximately 10 – 20 m/year (*Strozzi et al.*, 2002).

Altimetry has also been successfully used to measure glacier elevation changes. Airborne laser altimeters (ALA) have provided reliable elevation measurements along the aircraft flight track with about 20 cm accuracy (*Krabill et al.*, 1995) over glaciers, for example, in the Alps, Svalbard, Greenland and Antarctica (*Baltsavias et al.*, 2001; *Bamber et al.*, 2005; *Joughin et al.*, 2004). In 2003, spaceborne laser altimetry, called the Ice Cloud and land Elevation Satellite (ICESat) was launched to provide elevation measurement of glaciers around the globe with unprecedented accuracy (<5%) (*Schutz et al.*, 2005). Other than laser altimetry, *Lee et al.* (2013) first applied satellite radar altimetry to obtain

elevation changes in the Bering Glacier, Alaska from 1992 to 2010.

Direct mass balance estimates can be obtained from GRACE data, which have been used to quantify the contribution of global glacier melt to sea-level rise (*Gardner et al.*, 2013). However, since GRACE measures changes in the total water column, other potential sources such as groundwater storage changes may contaminate the estimates of ice mass balance (*Ramillien et al.*, 2008). Therefore, a significant discrepancy in regional mass balance estimates exists, especially where groundwater plays an important role in mass balance (*Gardner et al.*, 2013; *Jacob et al.*, 2012; *Yi and Sun*, 2014; *Zhang et al.*, 2013). Furthermore, GRACE's large footprint size (~200,000 km^2) makes it difficult to obtain mass change estimates with a fine spatial scale.

1.2 Motivation and Objectives

1.2.1 Motivation

Based on a literature review, the mass balance of global glacierized regions in different studies are in agreement except in HMA (*Cogley*, 2009; *Gardner et al.*, 2013; *Jacob et al.*, 2012). Multiple techniques based on GRACE, ICESat and Digital Elevation Model (DEM) datasets have been applied, but have led to different mass balance estimates in HMA, with discrepancies as large as 20 Gt/year (*Gardelle et al.*, 2013, 2012; *Gardner et al.*, 2013; *Jacob et al.*, 2012; *Kääb et al.*, 2012; *Matsuo and Heki*, 2010; *Yi and Sun*, 2014; *Zhao et al.*, 2016). Potential reasons for these differences include the influence of groundwater storage changes and different hydrological models used in GRACE data processing, and the fundamental differences between ICESat and GRACE observations (*Gardner et al.*, 2013; *Kääb et al.*, 2012). Specifically, the difference in mass balance

estimates that are as large as 16 Gt/year between ICESat and GRACE data exists in the Eastern Himalaya, especially in the Nyainqen Tanglha region (*Jacob et al.,* 2012; *Kääb et al.,* 2012). Moreover, recent estimates of thickness change based on DEM differencing also show discrepancies with ICESat observations in 5 different regions of Himalaya (*Brun et al.,* 2017). Since few in-situ measurements are available in this region, it is difficult to determine which estimate is correct. On the other hand, the amount of studies performed over Eastern Himalaya is smaller compared to other regions in HMA (*Bolch et al.,* 2012). Accordingly, in this dissertation, an attempt was made to estimate glacier mass changes in Nyainqen Tanglha, Eastern Himalaya based on a proposed new method, and a comparison was made with previous estimates.

There still exists other under-studied regions such as the Russian Arctic, which is the 6th largest glacierized area on the globe (*Radić et al.*, 2014). Recent studies indicate that the Russian Arctic has experienced ice mass loss of -6.6 Gt/year during 2012 – 2014 (*Melkonian et al.*, 2016). In addition, the Russian Arctic is predicted to make the 3rd largest contribution among all glacierized regions to sea-level rise of 20.29 to 28.31 mm by 2100 (*Melkonian et al.*, 2016; *Radić et al.*, 2014). Novaya Zemlya (NVZ), as the largest island in Russia Arctic, experienced the greatest ice mass loss in this region of –5.8 Gt/year from 2004 to 2009 (*Carr et al.*, 2014; *Moholdt et al.*, 2012). However, only one meteorological station on NVZ has recorded long-term temperature data which became even limited after 2000 (*Zhao et al.*, 2014). Therefore, space-borne techniques are the only option for glacial studies on NVZ. For marine-terminating glaciers along the coast of NVZ, one important contributor to sea level rise is calving flux. Several recent studies estimated calving flux using surface velocity obtained from optical or SAR image pairs and thickness from a DEM

at the glacier terminus (*Carr et al.*, 2014; *Melkonian et al.*, 2016). However, since the velocity estimates typically have larger errors near the terminus due to the decorrelation, this approach may lead to an erroneous estimates (*Sun et al.*, 2017). Therefore, it becomes necessary to have a complete distribution of glacier thickness towards more accurate estimates of the calving flux distant from the terminus. In this dissertation, over NVZ, multiple traditional spaceborne techniques for estimating surface mass balance were tested, such as GRACE and radar altimety. The contribution of influx and outflow to mass changes are also fully discussed.

1.2.2 Objectives and Contribution

The objective of this dissertation is to provide a comprehensive understanding of two under-studied glacierized regions, Novaya Zemlya and Eastern Himalaya, representing marine-terminating and land-terming glaciers, respectively. To achieve this goal, a new velocity-based iterative method of estimating thickness is proposed. The influence of temperature on thickness change is considered in this method. Based on our new thickness estimation method and multiple space-borne geodetic techniques, the glacier velocity, thickness, temporal thickness change, and mass balance are provided. The following contributions are made in this dissertation.

1. A new iterative velocity-based ice thickness estimation method is developed for temperate and non-temperate glaciers. The temperate-related Glen's flow law factor for this method is empirically determined based on in-situ measurements. The proposed method is validated and compared for 6 temperate glaciers, 1 non-temperate glacier, and 1 non-temperate ice cap.
2. Multiple traditional spaceborne techniques for observing surface mass balance

were applied to Novaya Zemlya. The mass loss for Novaya Zemlya in the period from 2003 to 2015 was fully explored. The contribution of calving flux to mass loss was also determined.

3. Thickness estimates of selected glaciers in Nyainqen Tanglha, Himalaya were generated using the proposed method from 2008 to 2016. The estimated thickness changes and mass changes were compared with previous estimates from Advanced Spaceborne Thermal Emission and Reflection Radiometer (ASTER) DEM and GRACE data, respectively.

1.3 Dissertation Structure

The dissertation is structured towards a complete dissertation. The current outline is shown as follows:

- Chapter 2 introduces five different spaceborne techniques used in this dissertation.
- Chapter 3 presents a new iterative velocity-based ice thickness estimate method.
- Chapter 4 describes the case study over Novaya Zemlya. Traditional spaceborne techniques were tested to obtain surface mass balance.
- Chapter 5 describes the case study over Nyainqen Tanglha. The proposed method was applied to obtain thickness change and surface mass balance estimates.
- Chapter 6 draws the conclusion and suggests future work.

2 Theoretical Background

2.1 Speckle Matching & Feature Tracking

Speckle matching (or intensity offset-tracking) is a widely-used technique in estimating glacier surface velocity. Based on cross-correlation, speckle matching is capable of detecting large horizontal displacement between two SAR images, which is not available via In-SAR. Another advantage is that speckle matching can obtain displacements in both range and azimuth directions while InSAR provides only range motion.

The speckle matching procedure can be summarized as follows. First, co-registration is performed to remove the initial offsets between the SAR image pairs using the geometric information obtained from the SAR satellite orbital parameters. The accuracy of this co-registration is at the pixel level. Then, cross-correlation is used to estimate accurate offsets for each selected pixel. A least squares method is applied to generate offsets polynomials which consequently improves the accuracy of offset estimation to a sub-pixel level. Finally, the pixel offsets are transformed into displacements along azimuth and range directions, and the velocity is estimated.

The cross-correlation method, as a traditional displacement estimation solution, has been applied in glacier motion estimation via multiple algorithms, including feature offset-tracking and speckle matching (*Ahn and Howat*, 2011; *Berthier et al.*, 2004; *Bindschadler et al.*, 1996; *Bindschadler and Scambos*, 1991; *Paul et al.*, 2015). In order to have a complete understanding, an example of the cross-correlation process in the speckle matching procedure is presented below. The process for feature-tracking follows a similar procedure.

First, assume that a pair of SAR images of size M×N pixels is provided as master and slave images. A patch window of size m×n pixels is first set for both master and slave images, translating the image into (M/m) × (N/n) scale. It is essential to note that in choosing a patch window size, there is a trade-off between resolution and processing time. Next, the search area size is set based on an initial estimation of the glacier velocity, because a large search area will not only take more processing time but also reduce cross-correlation accuracy. After determining these two parameters, the matched patch windows are selected for the search area. For example, a patch window (1, 1) (block A) is used in the master image as our target. Next, a search area (Area B) is set around a patch window (1, 1) (block B) in the slave image and moved over the patch window. Then, every cross-correlation factor between block A and block B is calculated while moving block B in Area B. After generating all available cross-correlation factors within Area B, these factors are averaged, and the ratio of each cross-correlation factor to this mean value is used as the correlation signal-to-noise ratio (SNR). To determine the match patch window pairs, an SNR threshold needs to be set. Similar to the patch window size, there is also a trade-off between accuracy and coverage for the cross-correlation SNR threshold. If a high threshold is applied, it will lead to fewer matched patch window pairs. Hence, this will increase the number of null pixels in the velocity map. However, if the threshold is low, the error due to low correlation will be significant, especially near the frontal position with high stream velocity. For each glacier, several different relative SNR are tested to ascertain the most suitable value with a default value of 0.2, which corresponds to a standard SNR of 2.0. Finally, if the highest SNR was larger than the chosen threshold, the corresponding offset is used to calculate the displacement for the patch window (1, 1) in the master image. Then,

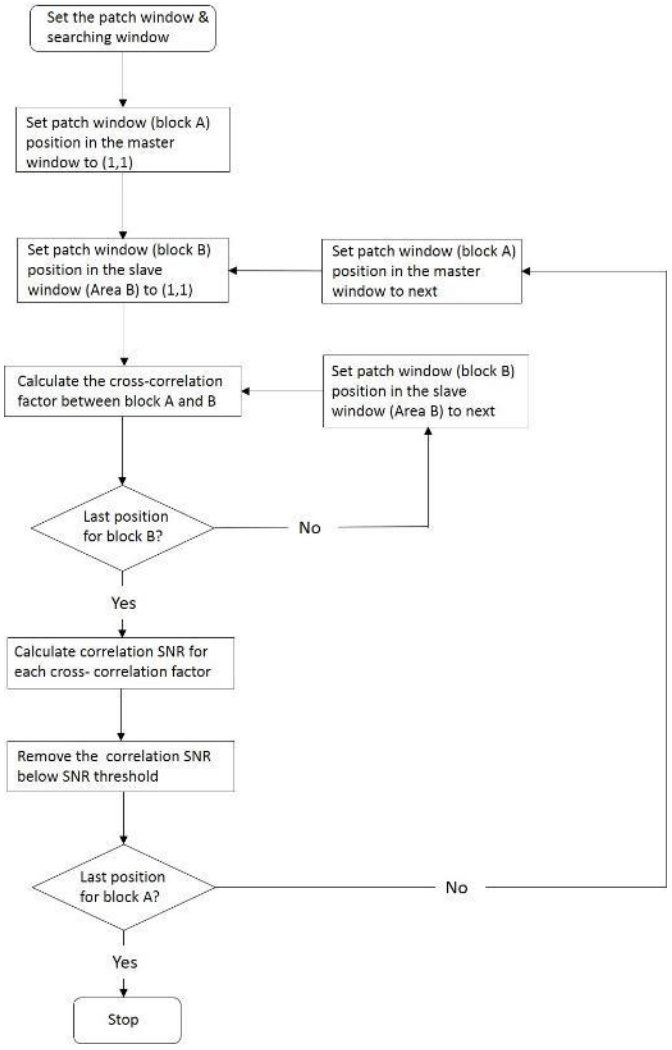

Figure 2-1 Flow chart of speckle matching by cross-correlation.

the patch window is moved to the next position within the master image, and the procedure is repeated until all available positions in the master image are calculated. The procedure is summarized in Figure 2-1.

Unlike speckle matching, feature tracking uses pairs of optical images instead of SAR images. The most widely used algorithm is the normalized cross-correlation of two subsets which is similar to the speckle matching technique (*Scambos et al.*, 1992). Like the procedure in Figure 2-1, the normalized cross-correlation can be computed by moving windows in the spatial domain. However, two-dimensional discrete Fourier transform in

the frequency domain, which is theoretically equivalent spatial convolution with a moving window, has been more widely used. Once the correlation map containing the correlation coefficient is created, a correlation peak is identified, and then sub-pixel displacement is computed using a 3×3 quadratic surface fitting (*Ahn and Howat*, 2011).

2.2 Principle of Radar Altimetry

Satellite radar altimetry is a remote sensing technique which has been extensively used to estimate surface elevation change. A nadir-looking electromagnetic pulse is transmitted from a satellite towards the surface at the speed of light. By measuring the two-way travel time T, the distance R between the satellite and the surface can be computed by Eq. (2-1) as

$$R = \frac{cT}{2}, \tag{2-1}$$

where c is the speed of light. Since the coordinate of the satellite are known as a priori, the surface elevation can be computed. Additionally, multiple corrections including propagation correction, surface correction, instrument correction and geophysical correction need to be considered to get the correct results (*ESA*, 2007).

In satellite altimetry, onboard reception and tracking are required to determine the return time of the transmitted pulses. The antenna transmits a short pulse of microwave radiation towards the surface. As shown in Figure 2-2 (*Rosmorduc*, 2016), the return pulse consists of a leading edge and a trailing edge. When the leading edge of the pulse hits the surface, the power of the return signal rises. The illuminated area of the pulse on the surface expands and forms a disc footprint. When the trailing edge arrives at the surface, the returned energy reaches a maximum value and starts to decay. The illuminated area then

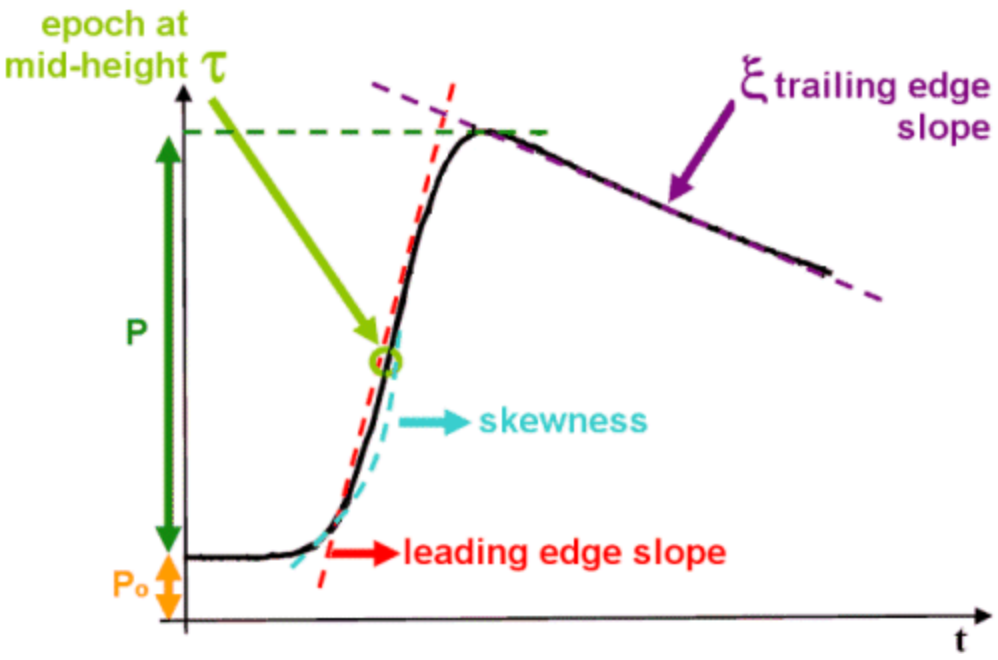

Figure 2-2 The returned waveform of radar altimeter on sea surface.

transforms into an annular shape. The change of the illuminated footprint and the return power are both shown in Figure 2-3 (*Rosmorduc*, 2016). It is clear that the return waveform has a steeper leading edge slope over a calm sea surface than a rough surface due to the more regular surface footprint.

Although the satellite altimeter was initially developed to estimate the elevation change of the sea surface, it has been successfully implemented over other non-ocean surfaces, including wetlands, rivers, lakes, and ice sheets. Due to the different surface characteristics, multiple retracking methods have been developed, including NASA β-retracker, surface/threshold retracker, ICE-1, ICE-2 and Sea Ice retracker (*Bamber*, 1994; *Davis*, 1996; *Laxon*, 1994; *Legrésy and Rémy.*, 1997; *Wingham et al.*, 1986). 18-Hz (~350 m along-track sampling) ICE-1 retracked measurements were used in this study according to the surface features of glacier (*Lee et al.*, 2013). The data are available in the Envisat RA-2 Geophysical Data Record (GDR) from cycle 9 to 93 (April 2002 – September 2010)

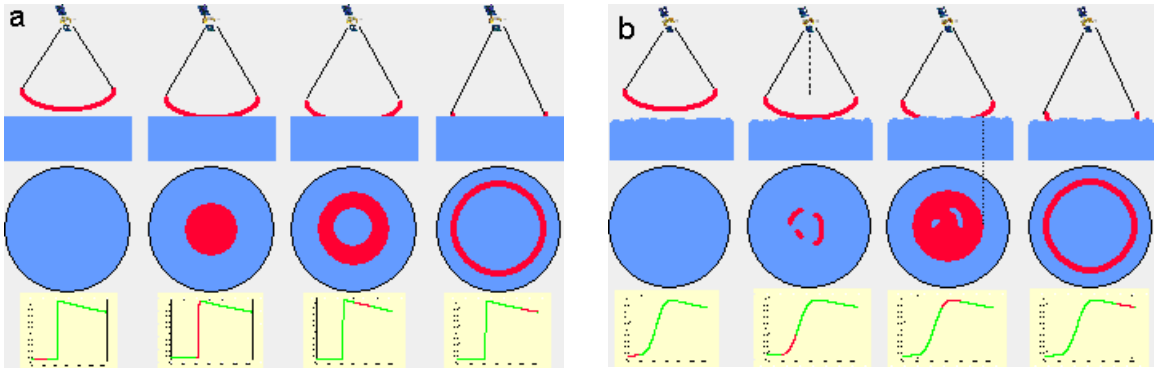

Figure 2-3 The interaction of the transmitted pulse and the illuminated area on the sea surface (a) and a rough surface (b).

with a 35-day repeat period.

2.3 GRACE Data Processing

GRACE is a spaceborne technique which is widely used to estimate surface mass balance by observing the time-variable gravity field. The geoid shape N, which is commonly used to describe the Earth's global gravity field, is expanded as a sum of spherical harmonic coefficients:

$$N(\theta,\phi) = a\sum_{l=0}^{\infty}\sum_{m=0}^{l}\tilde{P}_{lm}(\cos\theta)(C_{lm}\cos(m\phi) + S_{lm}\sin(m\phi)) \qquad (2\text{-}2)$$

where a is the radius of Earth, θ and ϕ are latitude and longitude, C_{lm} and S_{lm} are the spherical harmonic coefficients, and $\tilde{P}_{lm}$ is the fully-associated Legendre

The time-variable change in the geoid, ΔN, therefore represents change in the mass density distribution of the Earth. Hence the time-dependent spherical harmonic coefficients ΔC_{lm} and ΔS_{lm} could be expanded using the Earth density distribution function $\Delta\rho(\gamma,\theta,\phi)$ (*Chao and Gross*, 1987) as

$$\begin{Bmatrix}\Delta C_{lm}\\ \Delta S_{lm}\end{Bmatrix} = \frac{3}{4\pi a\rho_{ave}(2l+1)}\int \Delta\rho(r,\theta,\phi)\,\tilde{P}_{lm}(\cos\theta)$$

$$\times \left(\frac{r}{a}\right)^{l+2} \begin{Bmatrix} \cos(m\phi) \\ \sin(m\phi) \end{Bmatrix} \sin\theta d\theta d\phi dr \ , \tag{2-3}$$

where the average density of Earth, ρ_{ave} = 5517 kg/m^3.

To apply the inversion solution of the surface density distribution, the Earth's surface is approximated as a spherical shell (*Chao*, 2005). The mass is concentrated in a thin layer with a thickness of H. The surface density distribution $\Delta\sigma(\theta,\phi)$ can be expressed as the integral of $\Delta\rho$,

$$\Delta\sigma(\theta,\phi) = \int \Delta\rho(r,\theta,\phi)dr \ , \tag{2-4}$$

For the GRACE mission, H is assumed to be thin enough that $(r/a)^{l+2} \approx 1$. Thus Eq (2-3) can be expressed as

$$\begin{Bmatrix} \Delta C_{lm} \\ \Delta S_{lm} \end{Bmatrix}_{surface} = \frac{3}{4\pi a\rho_{ave}(2l+1)} \int \Delta\sigma(\theta,\phi)\, \tilde{P}_{lm}(\cos\theta) \times \begin{Bmatrix} \cos(m\phi) \\ \sin(m\phi) \end{Bmatrix} \sin\theta d\theta d\phi \ . \tag{2-5}$$

Eq. (2-5) describes the contribution to the geoid of surface mass redistribution. In addition, to relate ΔC_{lm} and ΔS_{lm}, $\Delta\sigma(\theta,\phi)$ can be expanded as

$$\Delta\sigma(\theta,\phi) = a\rho_w \sum_{l=0}^{\infty}\sum_{m=0}^{l} \tilde{P}_{lm}(\cos\theta)\left(\Delta\hat{C}_{lm}\cos(m\phi) + \Delta\hat{S}_{lm}\sin(m\phi)\right), \tag{2-6}$$

where ρ_w is the density of water which ensures that the $\Delta\hat{C}_{lm}$ and$\Delta\hat{S}_{lm}$ in the equation are dimensionless. Similar to (ΔC_{lm}, ΔS_{lm}):

$$\begin{Bmatrix} \Delta\hat{C}_{lm} \\ \Delta\hat{S}_{lm} \end{Bmatrix} = \frac{1}{4\pi a\rho_w} \int_0^{2\pi} d\phi \int_0^{\pi} \Delta\sigma(\theta,\phi)\, \tilde{P}_{lm}(\cos\theta) \times \begin{Bmatrix} \cos(m\phi) \\ \sin(m\phi) \end{Bmatrix} \sin\theta d\theta \ . \tag{2-7}$$

Thus, a relationship between (ΔC_{lm}, ΔS_{lm}) and ($\Delta\hat{C}_{lm}$, $\Delta\hat{S}_{lm}$) is obtained as

$$\begin{Bmatrix}\Delta C_{lm}\\ \Delta S_{lm}\end{Bmatrix} = \frac{3\rho_w}{\rho_{ave}}\frac{1+k_l}{2l+1}\begin{Bmatrix}\Delta \hat{C}_{lm}\\ \Delta \hat{S}_{lm}\end{Bmatrix}, \quad (2\text{-}8)$$

where k_l is the load deformation Love number of degree l, which represents the contribution of the underlying solid Earth to the geoid during surface mass redistribution.

From Eq. (2-6) and Eq. (2-8), surface mass density is determined to change based on changes ($\Delta C_{lm},\ \Delta S_{lm}$) from GRACE monthly gravity field observations:

$$\Delta\sigma(\theta,\phi) = \frac{a\rho_{ave}}{3}\sum_{l=0}^{\infty}\sum_{m=0}^{l}\tilde{P}_{lm}(\cos\theta)\left(\Delta\hat{C}_{lm}\cos(m\phi) + \Delta\hat{S}_{lm}\sin(m\phi)\right) \quad (2\text{-}9)$$

Ideally, the global surface mass redistribution can be directly obtained using the GRACE observations based on Eq. (2-9). However, strong spurious north-south stripes are observed as in Figure 2-4 (a) (*Duan*, 2014) due to the large systematic errors in GRACE. To eliminate these errors, post-processing including smoothing and filtering is required. A decorrelation filter and a Gaussian filter with a radius of 300 km are applied in the GRACE data utilized in this dissertation. Figure 2-4 (b) (*Duan*, 2014) shows the result of a global monthly mass anomaly after applying filtering. It is evident that, although most of the stripes on land in Figure 2-4 (a) (*Duan*, 2014) have been removed, a leak of mass loss has been added to the coastal ocean from the land, especially in Greenland. A leakage recovery method is applied to correct the regional mass changes as proposed by *Guo et al.* (2010). Two assumptions are made for this algorithm: 1) by applying the appropriate smoothing/ decorrelation process, most of the strips and high-degree noise are removed. This means that the remaining error is introduced by leakage; 2) the amount of reduced signal over the ocean due to de-aliasing is negligible. Thus, only the contribution of the signal from land to ocean is considered in the leakage recovery. Details of this leakage recovery method are given in *Guo et al.* (2010). Figure 2-5 (*Guo et al.*, 2010) represents the Global annual

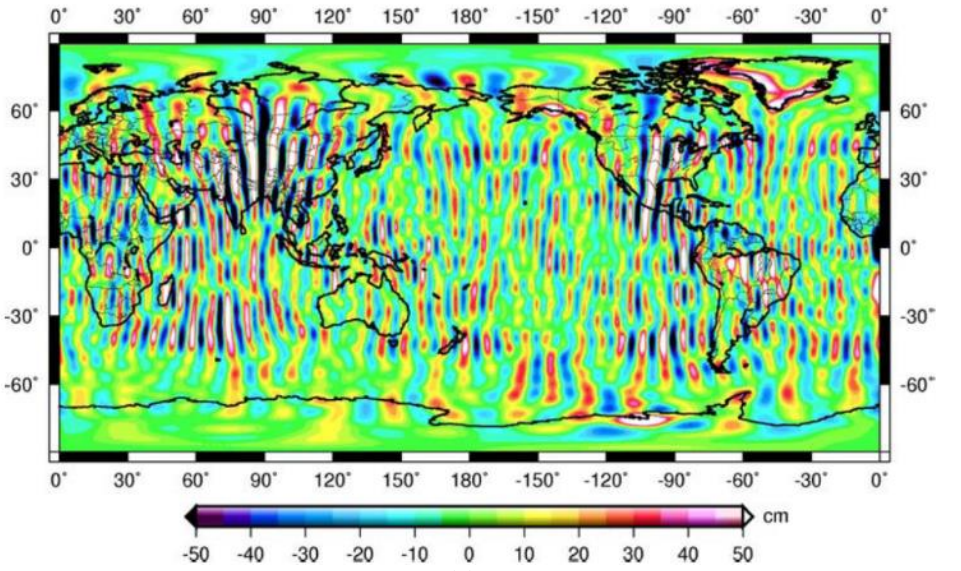

(a)

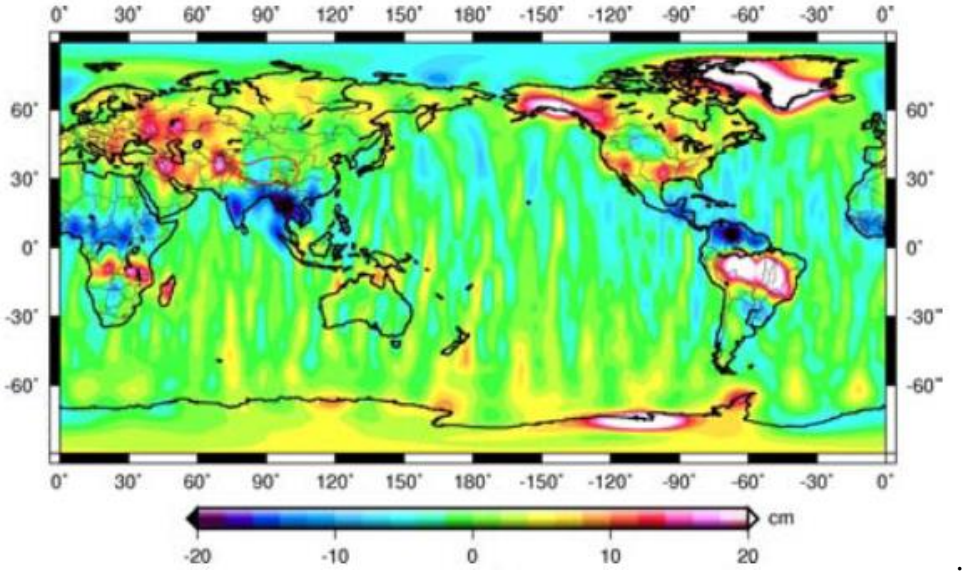

(b)

Figure 2-4 (a) Original monthly changes of surface mass anomaly in Equivalent Water Height (EWH) for March, 2005; (b) Filtered monthly changes of surface mass anomaly in EWH for March, 2005.

change of a surface mass anomaly in EWH after applying leakage correction in (b) and the difference between the original result and corrected result in (c). It is clear that the removal of the leakage error only affects the areas close to the coast.

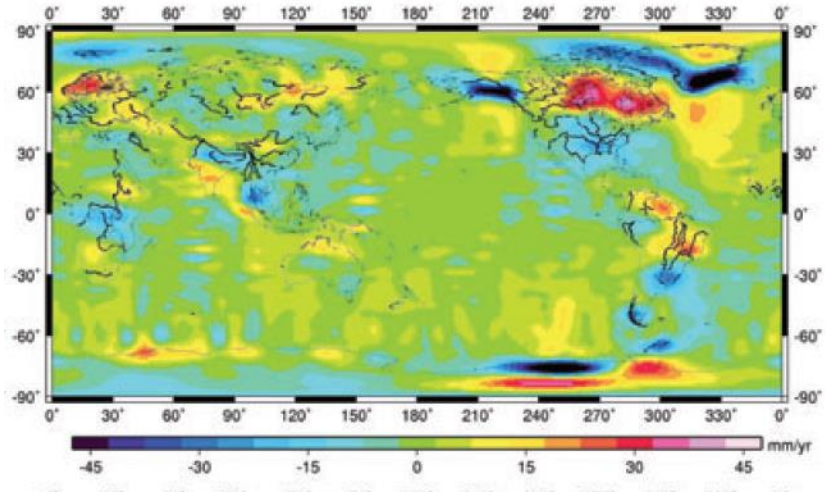

(a)

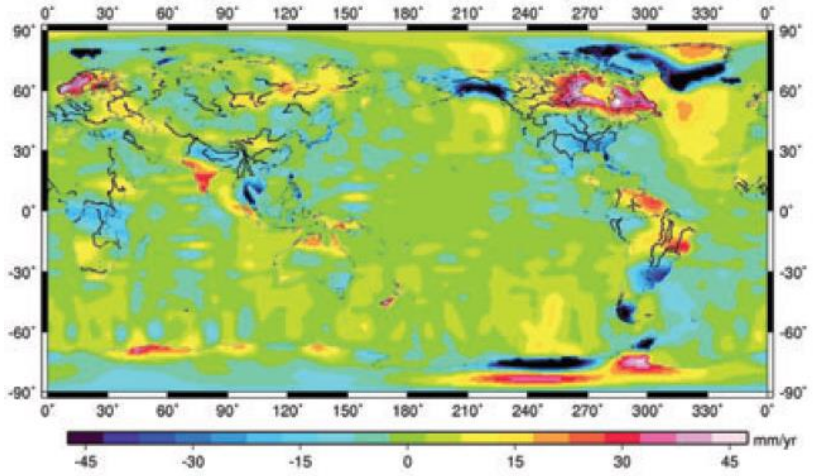

(b)

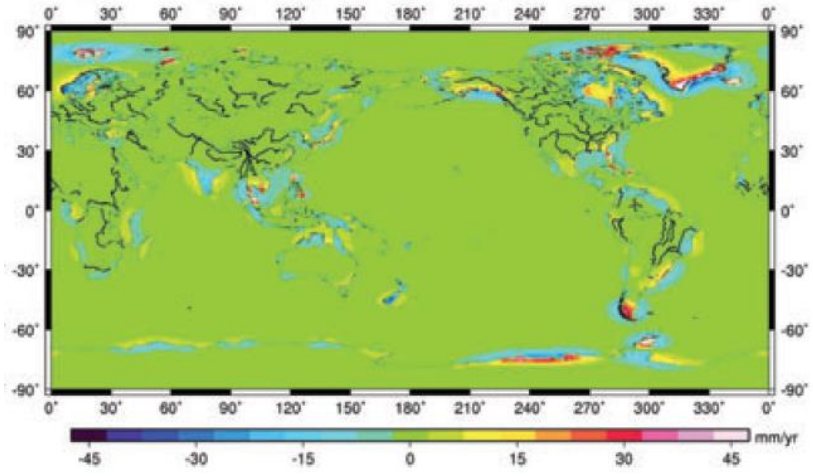

(c)

Figure 2-5 Global annual changes of surface mass anomaly in EWH (a) before applying leakage correction; (b) after applying leakage correction; (c) the difference between (a) and (b).

2.4 ERA-Interim Reanalysis Data Processing

ERA-Interim is an open-access database founded by the European Centre for Medium-Range Weather Forecasts (ECMWF). It provides global atmospheric analysis results from 1979 with a 12-hour analysis window. The spatial resolution of ERA-Interim is approximately 80 km in the horizontal direction with 60 different levels from the surface to 0.1 hPa in a vertical direction. In each 12-hour cycle, all available observations are combined with prior results from the forecast model to estimate global atmospheric parameters. Then the estimates of the current cycle are added to the updated prior state estimates which are used for the next cycle. Therefore, the atmospheric results we obtained from ERA-Interim is constrained by all available observations from the period of reanalysis due to data assimilation. The forecast model in ERA-Interim is adopted from the ECMWF IFS model designed for the ERA-40 (*Beljaars et al.*, 2006). A new release Cy31r2 is used for ERA-Interim process, which includes three completed components for the atmosphere, land surface, and ocean waves (*Uppala et al.*, 2011).

The atmospheric model is based on the spectral representation of the basic dynamic variables including cloud cover, solar radiation, precipitation, and moisture boundary. For each variable, a relevant stepping scheme is provided. The land-surface model in ERA-Interim is identical to that of ERA-40. A Tiled ECMWF Scheme for Surface Exchanges over Land (TESSEL) scheme is used to obtain thermal and water storage in 4 land layers at different depths that are provided in ERA-Interim. The ocean waves model reconstructs and represents the impact of ocean waves on airflow when transferring energy across the interface. It is based on both the transmitting atmospheric parameters that influence the wave growth to wave model and the returning information of the impact on the interface.

A Weighted Averaged Method (WAM) approach is applied to the ocean model in ERA-Interim.

In this dissertation, three monthly-mean-of-daily-mean products were extracted, namely, air temperature, sea surface temperature (SST) and snow depth. A series of Gridded Binary (GRIB) data were processed by the portal to generate distributed atmospheric estimates with a spatial resolution of 0.1°×0.1°.

3 New Velocity-Based Glacier Thickness Estimation Method

3.1 Background

Ice thickness is a fundamental parameter for evaluating the status and predicting the evolution of glaciers. It determines the total volume of water stored in glaciers. The seasonal melt of glaciers can be an important source of freshwater by feeding rivers such as in the Himalaya region where 45% of the total river flow is contributed by glacier melt (*Armstrong et al.*, 2018; *Kehrwald et al.*, 2008; *World Resources Institute*, 2003; *Wulf et al.*, 2016). Thickness variation, and therefore, the glacier mass balance can be reflected as a contributor to regional water resource change (*Kääb et al.*, 2012). To estimate ice thickness, an empirical scaling approach, relating the glacier's total volume to its area, has been widely used (*Bahr et al.*, 2015; *Chen and Ohmura*, 1990). However, via this simple model, the thickness distribution of a glacier is not available. Unlike the length and width of a glacier, which can be readily obtained from satellite imagery, glacier thickness is difficult to obtain. Due to prohibitive cost and topographical constraints, in-situ measurements of thickness are available only over selected regions (*Gärtner-Roer et al.*, 2014).

Based on physical principles and an assumption of constant basal shear stress (*Nye*, 1952, 1965), *Haeberl and Hoelzle* (1995) extended the study of *Nye* (1952) and summarized the relationship between thickness, basal stress, and surface topography. This approach has been employed in a series of recent studies (*Frey et al.*, 2014; *Linsbauer et al.*, 2012, 2009; *Paul and Linsbauer*, 2012).

An approach developed by *Farinotti et al.* (2009) used surface mass balance (SMB)

and surface topography to estimate the thickness. Based on the apparent mass balance, the ice flux was calculated over ice flowlines of selected ice catchment. The ice thickness was then computed using Glen's flow law (*Glen,* 1959). Later, *Huss and Farinotti* (2012) applied this method to generate the first global map of glacier thickness estimates. *Clarke et al.* (2013) used a similar mass-balance based method without restricting the analysis to flowlines. *McNabb et al.* (2012) combined surface velocity with the apparent mass balance to calculate ice flux and derived an ice thickness distribution of Columbia Glacier in Alaska. In addition to the surface velocity and SMB, rates of surface elevation change and the ice thickness at the boundary are required to implement a McNabb's method. Recently, *Rabatel et al.* (2018) proposed a similar approach to estimating the thickness of Argentière Glacier using SMB and velocity without requiring a surface elevation change rate.

Nevertheless, mass-balance data are not easily obtained and could be inaccurate in certain cases (*Zemp et al.*, 2013). *Gantayat et al*. (2014) proposed an approach to estimate glacier thickness only using surface velocity and surface topography in Himalaya regions where mass-balance data is unavailable. To simplify the model, the basal velocity was assumed to be proportional to the surface velocity.

Other than the approaches based on surface measurements, artificial neural networks have been employed to estimate glacier thickness using a Digital Elevation Model (DEM) and ice extents (*Clarke et al.*, 2009). By assuming consistent landscape features between the glacierized area and its neighboring region, prior topographic variation of ice-free terrain is trained to estimate the bedrock of adjacent ice-covered regions. *Brinkerhoff et al*. (2016) developed a Bayesian model with *a priori* hypothesis that the along-flow ice thickness is represented as a Gaussian process with unknown mean and

deterministic variance. This approach also requires observations of SMB, surface elevation change, and surface velocity.

To assess the performance of existing glacier thickness estimation methods, *Farinotti et al.* (2017) proposed the Ice Thickness Models Intercomparison eXperiment (ITMIX). The experiment compared thickness estimates from 17 different methods developed by 13 different research groups. The estimates from different approaches were compared over 15 glaciers and 3 ice caps. It was shown that the average composite estimates from all available methods are generally closer to the in-situ measurements than any individual estimate. Most of the thickness estimation methods in *Farinotti et al*. (2017) are based on SMB, surface velocity, or both. The SMB-based methods appear to provide more accurate estimates than velocity-based approaches. However, over certain regions, like Himalaya large glaciers, SMB-based methods are limited where the SMB estimates are unavailable or inaccurate (*Bolch et al.*, 2012; *Gantayat et al.*, 2014).Therefore, it is important to find a method which can be applied to any glacierized area while maintaining the accuracy similar to that of current SMB-based methods.

It is notable that most of the previous methods employ constant values for the rate factor in Glen's flow law (see A in Eq. (3-1)), except for Huss and Farinotti (2012) and Van Pelt et al. (2013) in which A is a variable. To determine the value of A, *Hooke* (1981) proposed an empirical relation based on englacial temperature. *Cuffey and Paterson* (2010) provided an in-depth summary of this rate factor based on field measurements and laboratory tests. The value of 2.4×10^{-24} $Pa^{-3}s^{-1}$ for temperate glaciers (*Cuffey and Paterson*, 2010) has been widely used in various thickness studies (*Clarke et al.*, 2013; *Farinotti et al.*, 2009).

In this study, an attempt was made to estimate the thickness of both temperate and non-temperate glaciers. By employing multiple spaceborne remote sensing datasets, an improved velocity-based method is proposed to estimate the thickness of glaciers in different geographic and climatic conditions. This method is based on the study of *Gantayat et al*. (2014). However, an iterative process is proposed to discard the assumption regarding basal and surface velocities used in *Gantayat et al*. (2014). The estimated englacial temperature is also obtained for temperate glaciers and nontemperate glaciers to determine the temperature-dependent Glen's flow rate factor A. This chapter is organized as follows. The study sites and data used are introduced in section 3.2. In section 3.3, the methodology is presented followed by the results in section 3.4. Finally, conclusions are provided in section 3.5.

3.2 Study Site & Data

Six temperate glaciers, one non-temperate glacier, and one ice cap are selected as test cases to consider different geographic and climatic conditions. The geographical distribution and glacial characteristics are presented in Figure 3-1 and Table 3-1. All data with '*' are referred to Farinotti et al. (2017) in Table 3-1. Most of the test glaciers are valley glaciers where surface velocity measurements are available or can be obtained. Crater glaciers and small ice caps are not included due to the lack of initial velocity inputs. For each case, the essential inputs include surface velocity and surface elevation for the proposed method. The surface velocities were either obtained from previous studies or estimated by using an intensity correlation-based method on Advanced Land Observing

Table 3-1 Overview of used data for each test case in this study. The following abbreviations are used: simple basin (SB); compound basin (CB); Shuttle Radar Topography Mission (SRTM); Randolph Glacier Inventory (RGI).

Glacier Name	Type	Thickness	DEM	Outline	Surface Velocity
Austfonna	Ice cap	Dowdeswell el al. (1986)*	Moholdt and Kääb (2012)*	Moholdt and Kääb (2012)*	Dowdeswell et al. (2008) *
Columbia	CB valley gl.	McNabb et al. (2012)	McNabb et al. (2012)	McNabb et al. (2012)	McNabb et al. (2012)
Corbassière	CB valley gl.	Gabbi et al. (2012)	SRTM DEM	RGI 2.0	This study
Freya	SB valley gl.	Unpub. ZAMG*	Unpub. ZAMG*	Unpub. ZAMG*	This study
North Glacier	SB valley gl.	Wilson et al. (2013)*	Wilson et al. (2013)*	Wilson et al. (2013)*	This study
South Glacier	SB valley gl.	Wilson et al. (2013)*	Wilson et al. (2013)*	Wilson et al. (2013)*	This study
Tasman	CB valley gl.	Anderton (1975)*	Columbus et al. (2011)*	LINZ (2013)*	This study
Unteraar	CB valley gl.	Bauder et al. (2003)*	Unpub. VAW-ETHZ*	Unpub. VAW-ETHZ*	This study

Satellite (ALOS) Phased Array type L-band SAR (PALSAR) image pairs of Fine Beam Single polarization (FBS) mode *(Sun et al.,* 2017*)*. The DEMs used are either from previous studies or the Shuttle Radar Topography Mission (SRTM). All the gridded in-situ bedrock elevations and glacier outlines are provided by *Farinotti et al.* (2017). An overview of the datasets is given in Table 3-1.

3.3 Methodology

3.3.1 Equations for Thickness Estimates

The proposed method extends the study of *Gantayat et al.* (2014), by introducing an iterative process to determine the ratio between basal and deformational velocities (ϕ in Eq. 3-2), which was assumed as a constant in *Gantayat et al.* (2014). A modified flow rate factor and revised slope estimation are also suggested in this study.

By applying the laminar flow equation, the relationship among velocity, basal stress

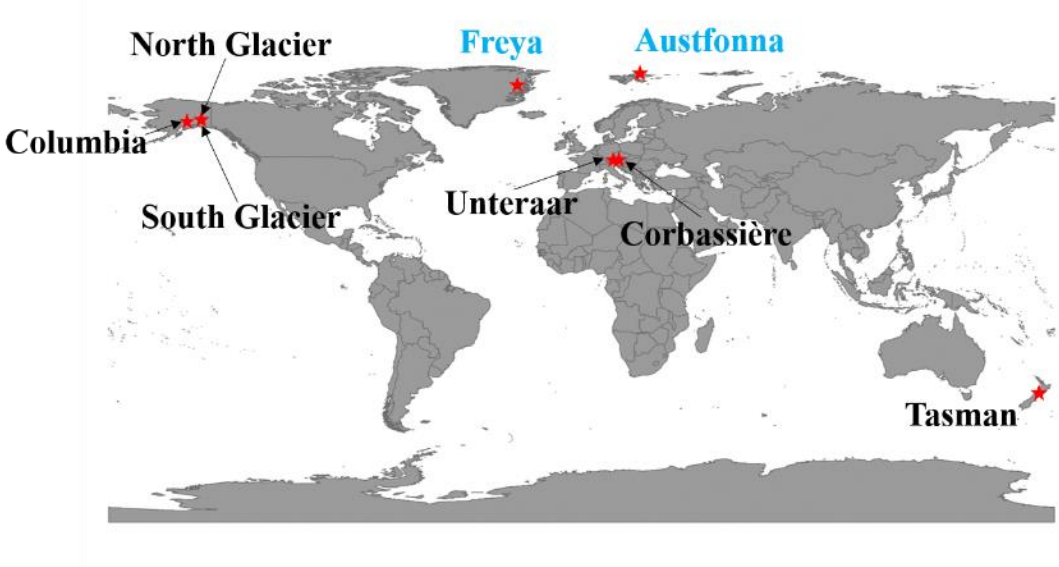

Figure 3-1 Geographic locations of the 8 test sites included in this study (red stars). Unteraar is shortened from Unteraargletscher for convenience. Black and blue color names represent temperate and non-temperate glacier, respectively.

and thickness can be described as (*Cuffey and Paterson*, 2010)

$$U_s = U_b + \frac{2A}{n+1}\tau^n H \ , \tag{3-1}$$

where U_s and U_b represent the surface and basal velocities, respectively; H is the ice thickness; τ is the driving stress, and n and A are the parameters from Glen's flow law. The second term on the right-hand side of Eq. (3-1) is called the deformational velocity (*Adhikari and Marshall*, 2011). Eq. (3-1) can be rewritten using a shape ratio ϕ between the basal sliding and deformational velocities such as

$$U_s = (1+\phi)\frac{2A}{n+1}\tau^n H \ . \tag{3-2}$$

Once surface velocity U_s is determined, H can be computed using the following equation derived from Eq. (3-2)

$$H = \frac{U_s}{(1+\phi)\frac{2A}{n+1}\tau^n} \ . \tag{3-3}$$

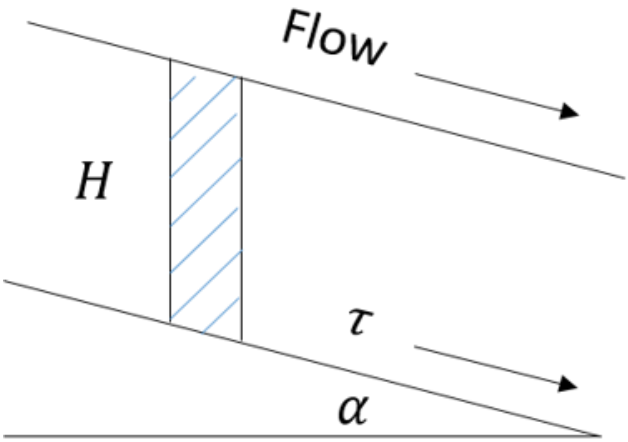

Figure 3-2 Schematic diagram of the basal stress for an ice element in a longitudinal glacier profile.

Typically, the parameter n is taken as a constant with n=3 (*Cuffey and Paterson*, 2010). Hence, there are three unknowns in Eq. (3-3), namely τ , ϕ and A. Notably, ϕ was assumed to be a constant value of 0.333 in *Gantayat et al.* (2014). Here, τ represents a basal stress introduced by vertically accumulated ice and snow in the longitudinal direction as shown in Figure 3-2. If the ice on the basal rock layer reaches stable status (either stays static or moves uniformly), the driving force, τ should be identical to the basal friction. Therefore, τ is assumed to vary identically to the basal friction which is related to the mass of accumulated ice and snow (M_{ice}) on the vertical direction. This variation can be divided into two parts as shown in Figure 3-3. When M_{ice} exceeds the trigger value ($M_{trigger}$), τ becomes a constant τ_{max}, equal to the sliding friction f_{max}. *Fowler* (2011) confirmed that τ_{max} for a moving glacier is nearly a constant. According to *Haeberli and Hoelzle* (1995), this constant τ_{max} can be calculated based on the range of vertical altitude of a glacier, ΔH as

$$\tau_{max}(\text{unit: kPa}) = \begin{cases} 0.5 + 159.8\Delta H - 43.5(\Delta H)^2, \Delta H \leq 1.6\ km \\ 150, \Delta H > 1.6\ km \end{cases}, \qquad (3\text{-}4)$$

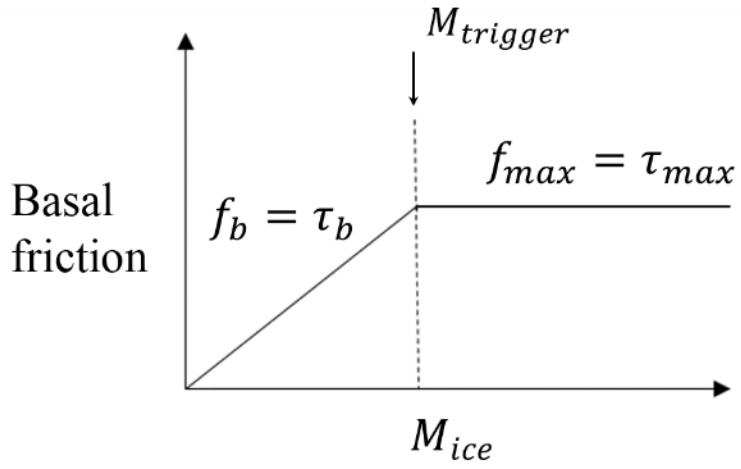

Figure 3-3 Schematic graph illustrating the variation of basal stress in terms of accumulated ice in vertical direction.

where $\Delta H = H_{max} - H_{min}$. H_{max} and H_{min} represent the maximum and minimum altitude of the glacier, respectively.

When M_{ice} is between 0 and $M_{trigger}$, τ becomes identical to the static friction f_b, but not exceeding τ_{max}. In the Shallow Ice Approximation (SIA), the basal stress τ can be expressed as the vertical gravitational force, given as (*Haeberli and Hoelzle*, 1995)

$$\tau_b = f\rho g H \sin\alpha \,, \tag{3-5}$$

where ρ , g , H , α represent ice density, gravity, ice thickness ,and bedrock slope, respectively; and f is the Nye shape factor which represents the fraction of driving stress that is supported by the basal drag (*Van der Veen*, 2013). Based on Eq. (3-5), the variables related to τ_b are the bedrock slope α, ice thickness H and shape factor f. In addition, f can be expressed as a product of two longitudinal stress factors L_d and L_s, such as (*Adhikari and Marshall*, 2011)

$$f = f_n \cdot L_d \cdot L_s \,, \tag{3-6}$$

where f_n is the uniform Nye shape factor which has been typically assumed to be 0.8 (*Adhikari and Marshall*, 2011; *Haeberli and Hoelzle*, 1995); L_d is the deformational factor,

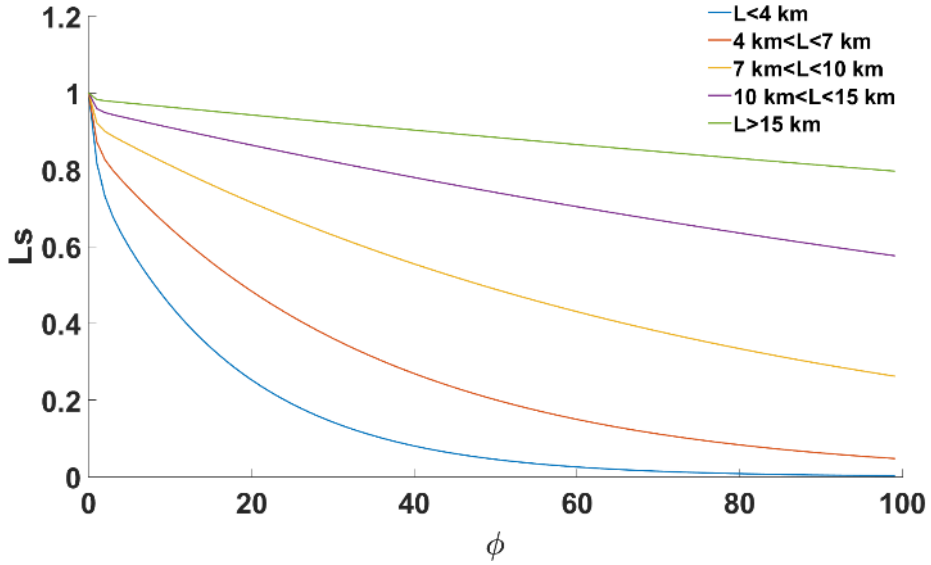

Figure 3-4 Variation of L_s with respect to glacier length L and shape ratio ϕ.

representing the ratio between the driving stress and the basal drag; and L_s is the sliding factor, describing the slip condition. L_d can be computed using Eq. (3-7) following *Adhikari and Marshall* (2011)

$$L_d = 1.00 - 0.18\alpha - 0.7\alpha^2 \, . \tag{3-7}$$

On the other hand, L_s can be expressed as a function of ϕ with a polynomial regression model for different ranges of the glacier length L (*Adhikari and Marshall*, 2011). The variations of L_s based on different ϕ and L are illustrated in Figure 3-4. For each given ϕ, L_s is determined accordingly. As expected, $L_s = 1$ when the basal movement status is static ($\phi = 0$). With updated f from Eq. (3-6), Eq. (3-5) can be rewritten as

$$\tau_b = f_n L_d L_s \rho g H \sin\alpha \, . \tag{3-8}$$

The thickness H_b (from τ_b) for the static case and H_{min} (from τ_{max}) for the uniformly moving case can then be calculated based on Eq. (3-3), Eq. (3-4) and Eq. (3-8):

$$H_b = \sqrt[n+1]{\frac{(n+1)U_s}{2A(1+\phi)(f_n L_d L_s \rho g \sin\alpha)^n}} \quad \text{and} \tag{3-9}$$

$$H_{min} = \frac{(n+1)U_s}{2A(1+\phi)\tau_{max}^n} \, , \tag{3-10}$$

where n is Glen's flow law exponent and chosen to be n=3 (*Farinotti et al.*, 2009; *Gantayat et al.*, 2014; *Huss and Farinotti*, 2012; *McNabb et al.*, 2012); ρ is the ice density (900 kg/m^3) (*Gardelle et al.*, 2012; *Gardner et al.*, 2013); and g is the gravitational acceleration (9.8 m s^{-2}).

Bedrock slope α, similar to the SIA approach, is assumed to be parallel to the surface slope since the measurements of α are not available. Hence, the surface slope is used as a proxy for α. In order to obtain α, the method described in *Gantayat et al*. (2014) is followed. However, instead of 100 m contour lines, 20 m contour lines are used to generate a map of slope distribution to preserve better spatial details. After obtaining the contour lines from the DEM, central lines of each glacier branch are determined. For every elevation band between two successive contours, the slope is calculated as 20 m/(length of the part of the central line that falls in that band in m).

It should be noted that the distance between contour lines within one band is different along the cross-sectional direction, especially at the junction between stream branches. For this case, one contour band is manually divided into multiple ones. The divisions are performed where the distance between contour lines changed dramatically. Each separated band thus has a similar distance between the contour lines, and details of slope variation at junctions can be preserved.

3.3.2 Iterative Process to Determine ϕ

Based on Eq. (3-9) and Eq. (3-10), the three unknowns to calculate τ_b, ϕ and A in Eq. (3-3) are converted to L_s , ϕ and A. Since L_s is directly related to ϕ, only two unknowns, ϕ and A, are needed to calculate thickness. Since A is independent of ϕ, it will

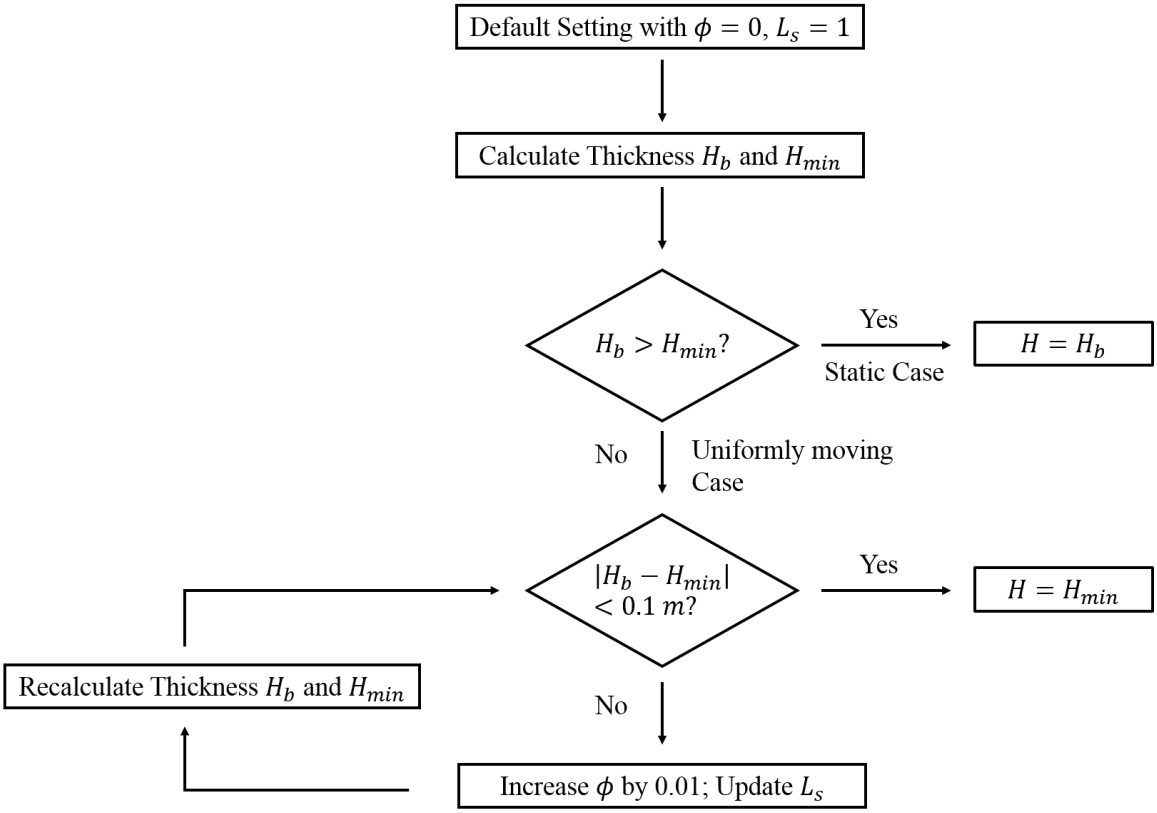

Figure 3-5 Flow chart of iterative thickness estimates.

be solved separately in the following section. A is assumed as a known constant A_0 in this section for now. Here, an iterative process is performed to determine ϕ based on the status of the basal motion of glaciers.

First, the basal motion status is assumed to be static. Under this assumption, ϕ is equal to zero, and L_s corresponds to 1 as can be seen from Figure 4. Then, H_b and H_{min} are calculated with the initial parameters of $\phi = 0, L_s = 1, A = A_0$ using Eq. (3-9) and Eq. (3-10), respectively, since H_b and H_{min} are derived from τ_b and τ_{max}. Under the assumption of static basal motion, τ_b should be smaller than τ_{max}, which means H_b should be larger than H_{min}. If $H_b > H_{min}$, it indicates that our assumption of static basal motion is correct, and H_b is the estimated glacier thickness. Otherwise, it indicates that the assumption is wrong, the basal layer is uniformly moving with $\phi \neq 0$. In this case, τ_b

reaches the $M_{trigger}$ in Figure 3 and is identical to τ_{max}, and indicates that $H_b = H_{min}$. To determine the corresponding ϕ and L_s when $H_b = H_{min}$, the shape ratio ϕ is increased by 0.01 from 0. It is noted that this change in ϕ will also affect the sliding factor L_s as described in section 3.2. With updated ϕ and L_s in Eq. (3-9) and Eq. (3-10), H_b and H_{min}.are recalculated and compared. This procedure is iterated until the difference between H_b and H_{min} becomes smaller than a pre-defined threshold of 0.1 m. Figure 3-5 illustrates this iteration procedure.

3.3.3 Optimal Englacial Temperature

Once ϕ is determined, the only remaining unknown to calculate *H* is Glen's flow law rate factor, *A*. In previous studies, constant values ranging from 0.93×10^{-24} $Pa^{-3}s^{-1}$ to 3.24×10^{-24} $Pa^{-3}s^{-1}$ have been used (*Brinkerhoff et al.*, 2016; *Clarke et al.*, 2013; *Farinotti et al.*, 2017, 2009; *Gantayat et al.*, 2014; *Morlighem et al.*, 2011). However, since *A* depends on temperature, the model proposed by *Hooke* (1981) was adopted as

$$A = A_0 \exp\left(-\frac{Q}{RT} + \frac{3C}{(T_r - T)^k}\right), \tag{3-11}$$

where A_0 = 9.302×10^7 kPa^{-3} yr^{-1}, Q = 78.8 kJ mol^{-1}, R = 8.321 J mol^{-1} K^{-1}, C = 0.16612 K, T_r =273.39° K, k = 1.17, and T is the englacial temperature. All of these parameters have been determined based on in-situ data from temperate Alpine glaciers (*Cuffey and Paterson*, 2010). Figure 3-6 shows the simulated variation of *A* with respect to the englacial temperatures from –40 °C to 0 °C based on Eq. (3-11). It is clear that *A* increases rapidly with the increase of englacial temperature, especially when the temperature is close to 0°C. Since we cannot directly obtain the englacial temperature for each glacier due to the lack of such measurements, we intend to find the estimated englacial temperature (T_{EET}) that is

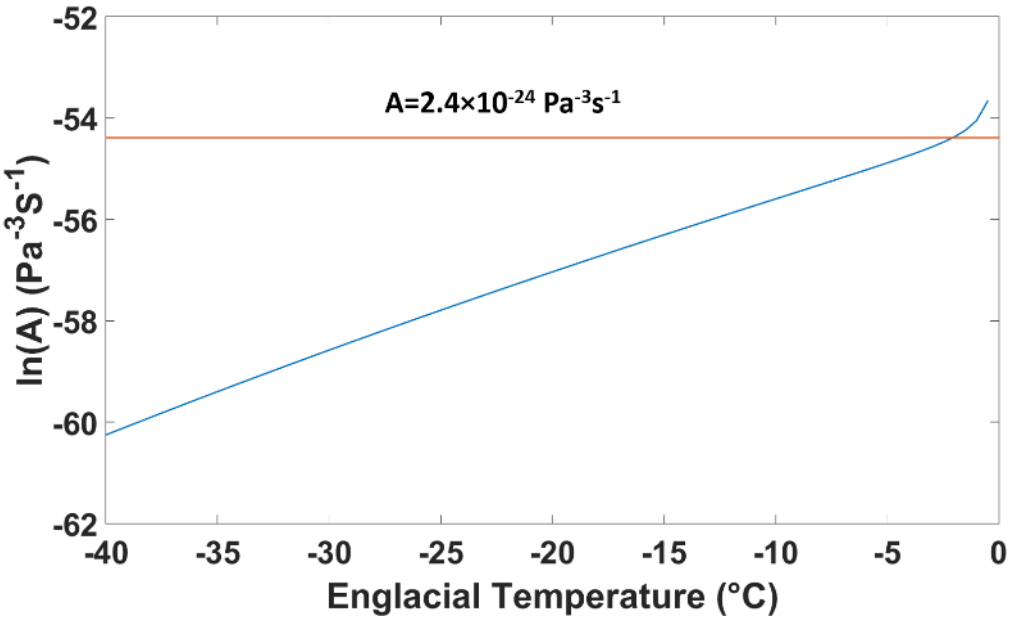

Figure 3-6 Logarithmic plot of Glen's flow law component A due to englacial temperature. Red line represents the value of A used in most previous studies.

applicable to any temperate glaciers where the englacial temperature should be close to 0°C (*Gudmundsson*, 1999; *Huss and Farinotti*, 2012). Accordingly, we attempt to empirically obtain individual T_{EET} based on six temperate glaciers, including Columbia, Corbassière, South Glacier, North Glacier, Tasman and Unteraargletscher (Unteraar). For each glacier, the englacial temperatures were tested ranging from 273.3° K to 270.0° K with a 0.1° K increment. With each assumed englacial temperature, the glacier thickness was computed. Next, the bedrock elevations were computed from the thickness estimates and the available DEMs. Then, the thickness errors were obtained by subtracting the calculated bedrock elevations from the in-situ bedrock elevations. Two error measures, relative mean error and relative mean absolute error (MAE), were computed for each temperature interval, and the englacial temperature value leading to the least sum of relative mean error and relative MAE is determined as T_{EET}. All of the test results can be found in Table 3-2. We obtained T_{EET} for each glacier as listed in Table 3-3.

Table 3-2 T_{EET} and T_{DET} for each temperate glacier in this study.

Profile Name	T_{EET} (K)	In-situ Measurements Quantity	T_{DET} (K)
Corbassière	273.0	285	273.0
Columbia	273.0	85	273.0
South Glacier	273.1	426	273.0
North Glacier	273.0	1010	273.0
Tasman	272.9	30	273.0
Unteraar	253.9	419	273.0

Interestingly, the calculated T_{EET} in Unteraar is significantly below 0°C (253.9 K) while the others are close to 0°C. It may be due to Unteraar's significant debris cover which buries the ice thicker than usual (*Farinotti et al.*, 2017). The debris leads to a large disagreement between the surface slope and the bedrock slope. Since surface slope is estimated much steeper, but assumed to be equal to bedrock slope in section 3.3.2, this slope difference results in an underestimated thickness. In order to balance this underestimation, lower T_{EET} for Unteraar has been obtained because a lower englacial temperature leads to a larger thickness estimate.

The calculated T_{EET} is based on in-situ measurements for each test case which means there is a correlation between T_{EET} and the in-situ measurements for each case. To eliminate this influence, for each case, a decorrelated englacial temperature $\boldsymbol{T_{DET}}$ is derived from T_{EET}. For one certain case, the weighted average of T_{EET} of the other test cases are calculated as the $\boldsymbol{T_{DET}}$. Since T_{EET} in each glacier is only related to the thickness measurements of the same glacier, $\boldsymbol{T_{DET}}$ in each test case is therefore independent from measurements of the same case. Notably, the incorrect T_{EET} in Unteraar is excluded in the calculation of $\boldsymbol{T_{DET}}$ in other cases. For example, the weighted average of T_{EET} in Columbia, South Glacier, North Glacier and Tasman are used as the $\boldsymbol{T_{DET}}$ of Corbassière. In this way, the $\boldsymbol{T_{DET}}$ of Corbassière is independent from the in-situ measurements in Corbassière If we exclude T_{EET} for Unteraar, the mean T_{DET} for each temperate glaciers is determined to

be 273.0° K, which corresponds to a rate flow factor A of 11.38×10^{-24} $Pa^{-3}s^{-1}$. This agrees with the conclusion that the englacial temperature in temperature glacier should be a constant.

Unlike temperate glaciers, the englacial temperature in non-temperate glaciers is related to the regional climate. Due to the lack of in-situ data in non-temperate glaciers, we follow the assumption made by *Huss and Farinotti* (2012) using a constant temperature offset T_{off} of 7° C between the englacial temperature and the mean annual air temperaure at equilibrium line altitude (ELA) in non-temperate glaciers (*Huang*, 1990). Following this assumption, we examined the annual surface air temperature T_{air} of Austfonna and Freya using the ERA-Interim re-analysis database with a gridded resolution of 0.5°. Around the DEM aquistion dates (2002 – 2010), T_{air} of Austfonna and Freya are 266.2 K and 261.1 K, respectively. Hence, after adding T_{off} to T_{air}, the englacial temperature were calculated to be 273.2 K and 268.1 K, respectively. Similar to the temperate glacier cases, T_{OET} of Austfonna and Freya were calculated based on in-situ bedrock elevations to be 273.1 K and 269.0 K, respectively. The offset between T_{OET} and T_{air} for Austfonna and Freya are 6.9 K and 7.9 K, which are close to *Huss and Farinotti* (2012)'s estimate of 7 °C.

Table 3-3 Englacial temperature test for 6 temperate glaciers. Blue color represents T_{DET} for each case. Red color represents T_{EET} for the individual case if it is not identical to T_{DET}.

Tasman

Englacial Temperature (K)	Mean Error (m)	Relative Mean Error (%)	MAE (m)	Relative MAE (%)	Total of Relative Mean Error and Relative MAE (%)
273.3	292.53	83.92	292.53	83.92	167.83
273.2	185.22	45.63	186.55	49.25	94.87
273.1	122.97	23.41	138.14	40.02	63.43
273.0	86.22	9.99	122.89	39.67	49.65
272.9	64.65	2.45	117.35	40.32	42.76
272.8	49.91	-2.73	113.82	40.83	43.56
272.7	38.97	-6.57	111.21	41.21	47.78
272.6	30.46	-9.55	109.27	41.61	51.16
272.5	23.92	-11.89	108.15	42.08	53.97
272.4	18.40	-15.47	108.86	44.44	59.90
272.3	14.31	-16.88	109.88	45.01	61.89
272.2	10.79	-18.11	111.01	45.55	63.66
272.1	7.68	-19.19	112.00	46.03	65.21
272.0	4.90	-20.15	113.00	46.51	66.66

South Glacier

Englacial Temperature (K)	Mean Error (m)	Relative Mean Error (%)	MAE (m)	Relative MAE (%)	Total of Relative Mean Error and Relative MAE (%)
273.3	50.66	76.13	50.66	76.13	58.76
273.2	19.92	19.31	22.82	29.64	31.04
273.1	2.09	-13.65	16.59	31.64	20.85
273.0	-8.47	-33.17	18.12	41.78	20.94
272.9	-15.34	-45.87	21.03	50.82	23.83
272.8	-20.16	-54.77	23.57	57.70	26.79
272.7	-23.73	-61.38	25.82	63.16	29.34
272.6	-26.51	-66.52	27.99	67.78	31.48
272.5	-28.75	-70.66	29.94	71.67	33.28
272.4	-30.61	-74.10	31.60	74.94	34.82
272.3	-32.19	-77.01	33.05	77.76	36.15
272.2	-33.56	-79.54	34.37	80.24	37.33
272.1	-34.76	-81.77	35.55	82.45	38.38
272.0	-35.85	-83.77	36.61	84.42	39.33

North Glacier

Englacial Temperature (K)	Mean Error (m)	Relative Mean Error (%)	MAE (m)	Relative MAE (%)	Total of Relative Mean Error and Relative MAE (%)
273.3	83.23	80.99	83.23	80.99	166.46
273.2	37.91	35.73	37.97	35.79	75.88
273.1	11.53	9.39	25.42	24.56	36.95
273.0	-4.32	-6.46	22.74	22.64	27.06
272.9	-11.63	-13.84	22.54	22.88	34.17
272.8	-16.75	-19.04	24.41	25.01	41.15
272.7	-19.66	-22.02	25.85	26.67	45.51
272.6	-21.46	-23.83	26.80	27.79	48.27
272.5	-22.74	-25.12	27.61	28.73	50.35
272.4	-23.75	-26.12	28.27	29.49	52.02
272.3	-24.55	-26.93	28.85	30.14	53.40
272.2	-25.20	-27.60	29.33	30.68	54.53
272.1	-25.76	-28.17	29.77	31.16	55.53
272.0	-26.23	-28.65	30.15	31.58	56.38

Unteraargletscher

Englacial Temperature (K)	Mean Error (m)	Relative Mean Error (%)	MAE (m)	Relative MAE (%)	Total of Relative Mean Error and Relative MAE (%)
273.3	224.67	90.13	224.67	90.13	180.26
273.2	168.98	66.63	168.98	66.63	133.26
273.1	136.55	52.87	136.95	53.43	106.29
273.0	117.76	45.12	118.71	46.41	91.53
272.9	106.34	40.42	107.78	42.31	82.73
272.8	98.83	37.29	100.82	39.74	77.03
272.7	93.64	35.11	96.19	38.08	73.19
272.6	89.88	33.50	92.89	36.89	70.39
272.5	86.91	32.25	90.24	35.91	68.16
272.4	84.62	31.27	88.22	35.16	66.43
272.3	82.78	30.45	86.60	34.54	64.98
272.2	81.18	29.74	85.25	34.05	63.79
272.1	79.84	29.15	84.11	33.62	62.77
272.0	78.64	28.62	83.05	33.21	61.83
253.9	15.34	0.07	37.18	18.68	18.75

Corbassière

Englacial Temperature (K)	Mean Error (m)	Relative Mean Error (%)	MAE (m)	Relative MAE (%)	Total of Relative Mean Error and Relative MAE (%)
273.3	124.28	82.97	142.71	82.26	165.23
273.2	62.93	42.42	84.83	45.07	87.49
273.1	27.34	18.89	63.50	34.07	52.96
273.0	6.25	4.94	56.47	31.67	36.61
272.9	-7.57	-4.20	56.41	32.71	36.91
272.8	-17.05	-10.51	57.86	34.33	44.84
272.7	-23.89	-15.01	59.39	35.82	50.83
272.6	-29.01	-18.36	60.93	37.16	55.51
272.5	-33.18	-21.08	62.39	38.34	59.41
272.4	-36.65	-23.37	63.76	39.42	62.79
272.3	-39.51	-25.24	65.09	40.40	65.64
272.2	-42.08	-26.93	66.37	41.32	68.25
272.1	-44.27	-28.46	67.50	42.22	70.67
272.0	-46.22	-29.77	68.66	43.07	72.84

Columbia

Englacial Temperature (K)	Mean Error (m)	Relative Mean Error (%)	MAE (m)	Relative MAE (%)	Total of Relative Mean Error and Relative MAE (%)
273.3	345.20	81.91	345.20	81.91	163.83
273.2	168.25	38.86	168.25	38.86	77.71
273.1	65.59	13.88	85.52	19.27	33.14
273.0	4.80	-0.92	75.85	17.97	18.89
272.9	-34.73	-10.54	92.36	22.59	33.13
272.8	-62.24	-17.22	110.73	27.31	44.53
272.7	-82.40	-22.09	124.68	30.89	52.98
272.6	-98.05	-25.88	135.52	33.67	59.55
272.5	-110.65	-28.93	144.23	35.90	64.83
272.4	-120.40	-31.32	152.73	38.03	69.35
272.3	-127.07	-32.96	158.60	39.50	72.45
272.2	-132.55	-34.31	163.76	40.78	75.10
272.1	-137.00	-35.41	167.96	41.83	77.25
272.0	-140.41	-36.24	171.17	42.62	78.86

Table 3-4 List of ALOS PALSAR images used to estimate surface velocity in this study.

Scene No.	Glacier Region	Acquisition Date
ALPSRP107920910	Corbassière	02/02/2008
ALPSRP114630910	Corbassière	03/19/2008
ALPSRP208191210	South Glacier	12/21/2009
ALPSRP214901210	South Glacier	02/05/2010
ALPSRP208191210	North Glacier	12/21/2009
ALPSRP214901210	North Glacier	02/05/2010
ALPSRP109026300	Tasman	02/10/2008
ALPSRP111506290	Tasman	03/27/2008
ALPSRP109670920	Unteraar	02/19/2010
ALPSRP116380920	Unteraar	04/06/2010

3.4 Result

3.4.1 Initial Inputs

To test the proposed method, 8 different glaciers and ice caps were selected as shown in Figure 3-7. The black lines within the glacier outlines are 100 m contour lines derived from DEMs. The red and blue lines in (a) and (e) represent profiles 1 and 2, respectively. The red points with black circles represent starting points for each profile. The cross-sectional profiles in (c) are sorted from North to South and numbered from (1) to (10). A total of 88 solutions using 17 different methods were compared with our estimates in this study. These solutions were obtained over 8 along-flow profiles and 12 cross-sectional profiles. As described in section 3.3.2, two inputs, surface velocity, and bedrock slope, are needed to calculate the ice thickness from our proposed method. In this study, all of the unpublished surface velocities U_s were estimated from ALOS PALSAR pairs listed in Table 3-4 using the speckle matching technique described in section 3.3.1.

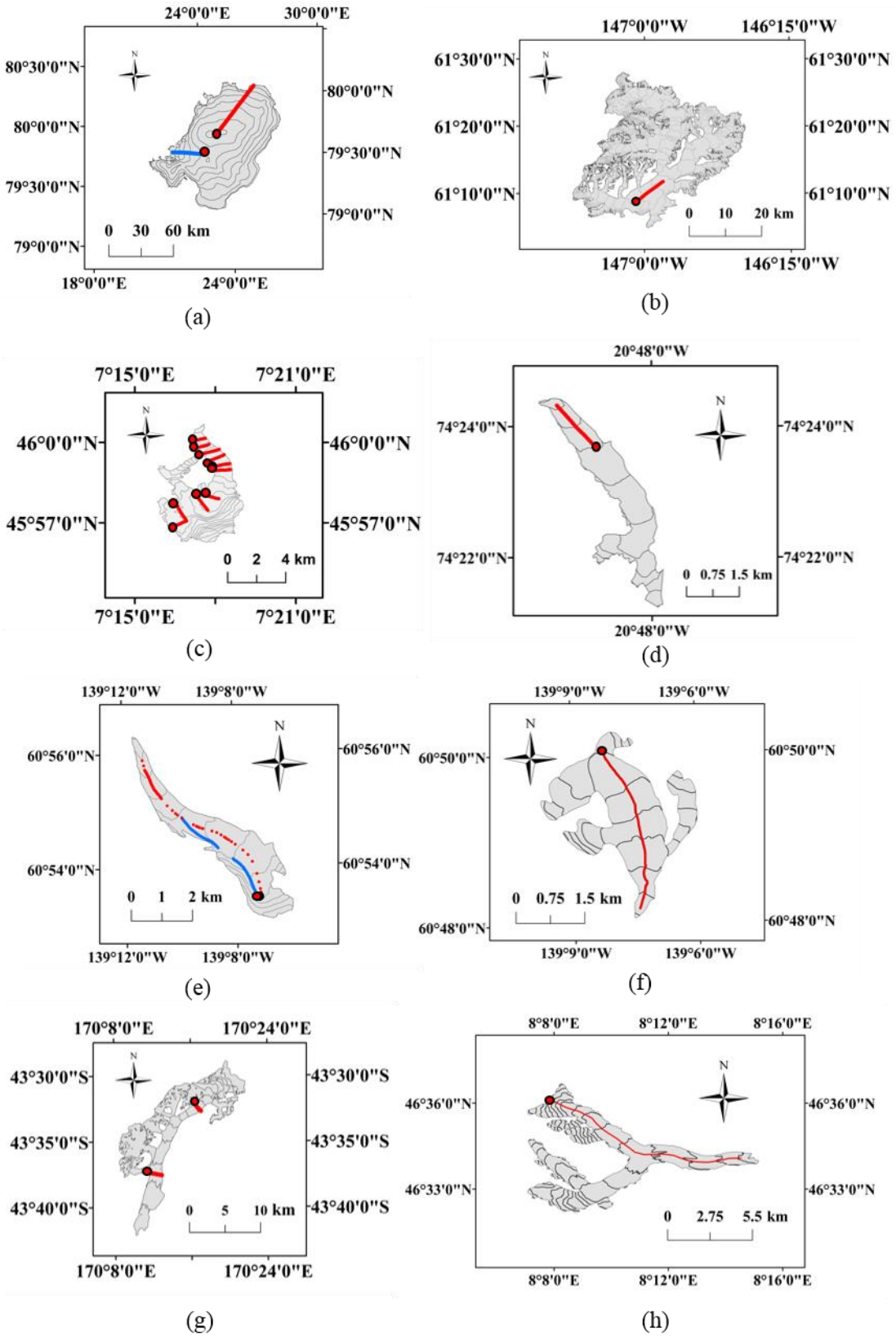

Figure 3-7 Glacier outlines and selected profiles for (a) Austfonna, (b) Columbia, (c) Corbassière, (d) Freya, (e) NorthGlacier, (f) SouthGlacier, (g) Tasman, (h) Unteraar.

3.4.2 Comparison with Existing Methods

(a). Temperate Glaciers

A total of 2,249 samples from in-situ data obtained from *Farinotti et al.* (2017) were used for the comparison over 6 temperate glaciers in this study, with 5 along-flow profiles and 12 cross-sectional profiles. Considering the fact that glacier thickness changes over time, the bedrock topography, obtained by subtracting the thickness from the surface elevation, was used for comparison assuming bedrock remains unchanged. Even though the observation dates of the ALOS SAR images were chosen close to that of the DEM, a temporal inconsistency between surface velocity and the DEM still exists as all of the velocity estimates are obtained only during the winter-spring season. However, since only the contour line from the DEM is used in the proposed method to obtain the surface slope, the estimated thickness is not influenced by a temporal inconsistency. Still, this inconsistency leads to an error when using the DEM to calculate bedrock elevation. An error at the magnitude of 10 m is introduced due to the inconsistency considering the temporal change of DEM for worldwide glaciers (*Moholdt et al.*, 2010; *Nuth and Kääb*, 2011; *Paul and Haeberli*, 2008). The thickness estimates using the "Gantayat" method were independently obtained using the same surface velocity and surface slope as the proposed method in this study following *Gantayat et al*. (2014), and the estimates using the "McNabb" method are obtained from *McNabb et al*. (2012). "Gantayat-v2" method are obtained from *Gantayat et al*. (2017). All the other results were obtained from *Farinotti et al*. (2017).

The bedrock elevations along 5 along-flow profiles and 2 of 12 cross-sectional profiles over 5 different glaciers (Columbia, South Glacier, North Glacier, Unteraar,

Tasman) were obtained and compared with the estimates using 14 existing methods as shown in Figure 3-8. The thick blue and red lines represent the surface and in-situ bedrock elevations, respectively. The other colorful lines represent the bedrock estimates from previous methods which are obtained from ITMIX. We calculated the error by comparing the estimated bedrock elevations from the thickness estimates and the in-situ bedrock elevations. The mean error, mean MAE, relative mean error and relative MAE were computed with their ranks as shown in Tables 3-5 to 3-8. Based on these statistics, our method shows agreement with in-situ measurement as the previous SMB methods except for Unteraar and Tasman glaciers. These two notable exceptions were also mentioned in *Farinotti et al.* (2017) due to debris cover. As mentioned in section 3.4.2, significant debris led to a large discrepancy between the surface slope and bedrock slope, that ultimately resulted in a significant underestimation of thickness. Another notable finding at Unteraar was that the previous velocity-based method (*Gantayat et al*., 2014) led to a smaller error than our method. This is largely due to the balance between the overestimated thickness from the rate factor bias and the underestimated thickness from the slope bias. As our model excluded the rate factor bias, the solution, therefore, obtained a larger underestimated error with only the contribution from slope bias. However, the ”Gantayat” method is influenced by both the underestimated error from the slope bias and an overestimated error from the rate factor bias. The combination of these two errors led to a better estimate using the ”Gantayat” method. Additionally, we observed a poor performance for Tasman. Since only 30 samples are available for the Tasman site, the relatively poor performance might be related to the bias caused by an insufficient number of in-situ measurements.

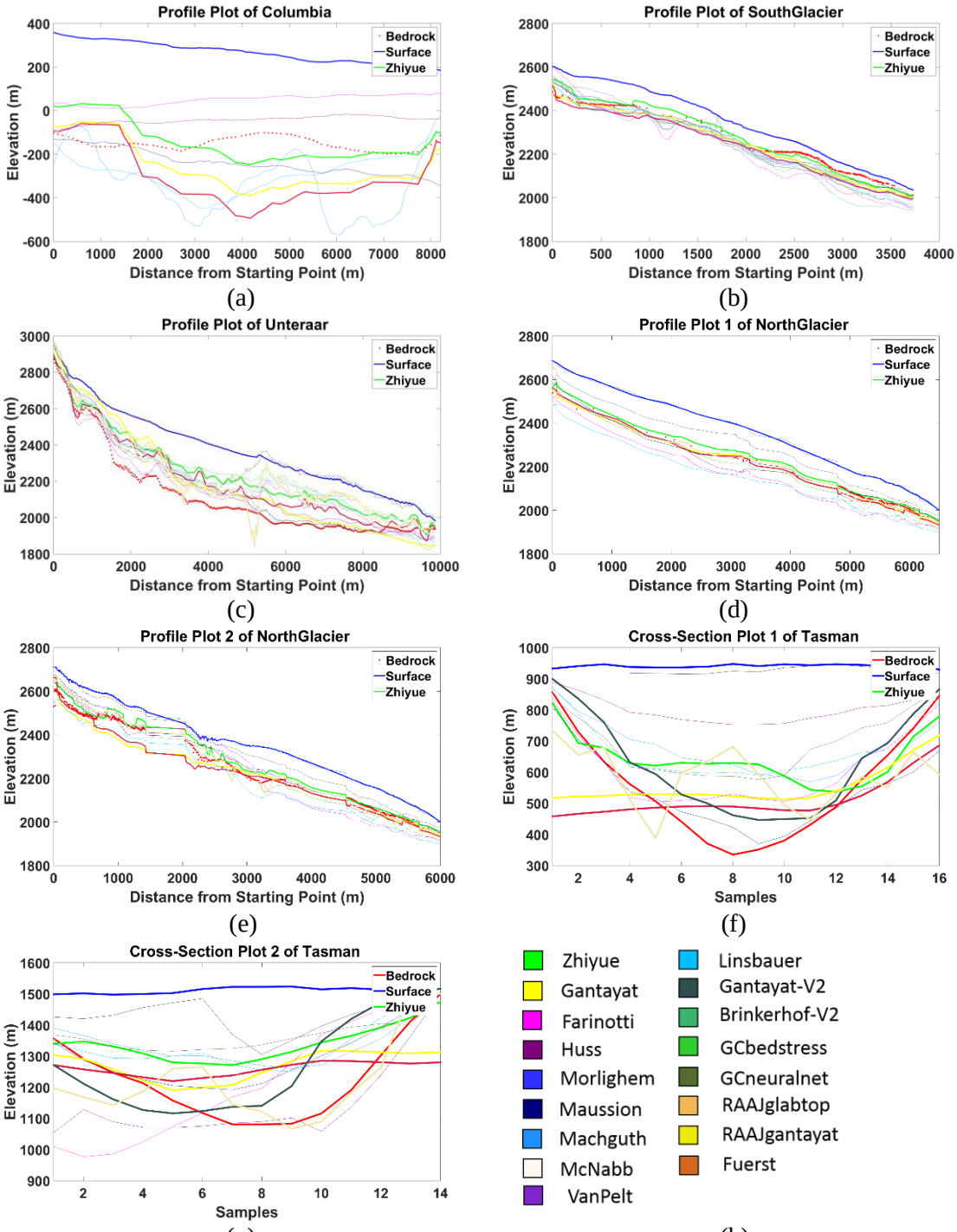

Figure 3-8 Comparison of bedrock elevations obtained from the glacier thickness estimates of this study (thick green line) and other previous methods along 5 along-track profiles (from Columbia, South Glacier, North Glacier, Unteraar) and 2 cross-sectional profiles (from Tasman).

Table 3-5 Comparison of mean error of thickness estimates (unit: m). '-' represents no value, Italic results are from velocity-based methods. Numbers within the brackets represent the rank in individual profiles. Red results have the top 3 performance.

Name	Corbassière	Columbia	SouthGlacier	NorthGlacier_1	NorthGlacier_2	Tasman	Unteraar
This Study	*4.94 (1)*	*14.82 (1)*	*-3.05 (1)*	*8.53 (2)*	*-18.49 (5)*	*92.28 (6)*	*120.75 (10)*
Gantayat	*-5.20 (2)*	*-109.48 (5)*	*-27.54 (3)*	*-13.37 (4)*	*-32.54 (7)*	*-68.52 (5)*	*69.54 (5)*
Farinotti	-	202.6 (8)	-60.51 (9)	-64.63 (9)	-8.00 (2)	24.84 (3)	57.73 (4)
Huss	-	108.92 (4)	-34.12 (6)	-18.03 (5)	-0.98 (1)	93.79 (7)	48.85 (2)
Morlighem	-	-	-44.44 (8)	-	-	316.02 (12)	-
Maussion	-	-183.98 (7)	-23.16 (2)	7.27 (1)	27.40 (6)	24.68 (2)	49.12 (3)
Machguth	-	-86.23 (3)	-27.87 (4)	-	-	121.41 (10)	122.27 (11)
Linsbauer	-	-136.22 (6)	-33.66 (5)	-63.76 (8)	-52.18 (8)	108.19 (8)	105.92 (7)
Gantayat-v2	-	-	-	-	-	*58.56 (4)*	*71.93 (6)*
Brinkerhof-v2	-	-	-67.46 (10)	-	-	-	37.51 (1)
GCbedstress	-	-	-42.9 (7)	-35.81 (6)	-11.23 (4)	-	134.90 (12)
GCneuralnet	-	-	-15.23 (2)	36.87 (7)	67.51 (9)	136.27 (11)	167.65 (13)
RAAJglabtop	-	-	-	-	-	117.56 (9)_	108.66 (8)
RAAJgantayat	-	-	-	*-12.75 (3)*	*10.13 (3)*	*12.68 (1)*	*112.13 (9)*
MvNabb	-	-17.46 (2)	-	-	-	-	-

Table 3-6 Comparison of MAE of thickness estimates (unit: m). '-' represents no value, Italic results are from velocity-based methods. Numbers within the brackets represent the rank in individual profiles. Red results have the top 3 performance.

Name	Corbassière	Columbia	SouthGlacier	NorthGlacier_1	NorthGlacier_2	Tasman	Unteraar
This Study	*46.49 (2)*	*75.24 (2)*	*27.18 (1)*	*9.76 (1)*	*20.17 (1)*	*124.37 (8)*	*121.60 (10)*
Gantayat	*40.41 (1)*	*143.33 (6)*	*28.85 (2)*	*14.59 (3)*	*37.48 (6)*	*110.91 (4)*	*89.18 (5)*
Farinotti	-	202.60 (8)	75.00 (11)	67.8 (9)	51.46 (7)	112.13 (5)	70.41 (4)
Huss	-	108.92 (4)	39.91 (7)	19.29 (5)	21.62 (2)	169.21 (10)	58.53 (2)
Morlighem	-	-	54.82 (9)	-	-	-	-
Maussion	-	198.38 (7)	29.93 (3)	12.14 (2)	28.65 (5)	63.43 (1)	58.79 (3)
Machguth	-	89.19 (3)	36.09 (4)	-	-	122.91 (7)	125.09 (11)
Linsbauer	-	140.50 (5)	36.33 (5)	63.76 (8)	52.27 (8)	117.72 (6)	108.57 (7)
Gantayat-v2	-	-	-	-	-	*93.91 (3)*	*91.55 (6)*
Brinkerhof-v2	-	-	70.36 (10)	-	-	-	57.03 (1)
GCbedstress	-	-	47.40 (8)	36.54 (6)	27.86 (4)	-	134.90 (12)
GCneuralnet	-	-	36.80 (6)	36.87 (7)	67.51 (9)	138.37 (9)	168.13 (13)
RAAJglabtop	-	-	-	-	-	643.91 (11)	110.56 (8)
RAAJgantayat	-	-	-	*15.81 (4)*	*24.93 (3)*	*69.46 (2)*	*118.17 (9)*
McNabb	-	57.69 (1)	-	-	-	-	-

Table 3-7 Comparison of relative mean error of thickness estimates (unit: m). '-' represents no value, Italic results are from velocity-based methods. Numbers within the brackets represent the rank in individual profiles. Red results have the top 3 performance.

Name	Corbassière	Columbia	SouthGlacier	NorthGlacier_1	NorthGlacier_2	Tasman	Unteraar
This Study	*2.75% (1)*	*1.52% (1)*	*-24.26% (1)*	*8.35% (2)*	*17.76% (5)*	*12.45% (4)*	*46.34% (11)*
Gantayat	*-14.38% (2)*	*-28.73% (5)*	*-68.13% (4)*	*-14.20% (3)*	*-34.63% (7)*	*-53.64% (11)*	*23.02% (5)*
Farinotti	-	49.14% (8)	-157.14% (10)	-71.75% (9)	-11.14% (3)	-0.73% (1)	17.93% (3)
Huss	-	26.26% (4)	-86.04% (6)	-18.46% (5)	-2.98% (1)	15.65% (5)	13.16% (2)
Morlighem	-	-	-120.80% (9)	-	-	-	-
Maussion	-	-44.24% (7)	-56.35% (2)	8.16% (1)	25.18% (6)	-1.95% (2)	18.06% (4)
Machguth	-	-22.45% (3)	-78.17% (5)	-	-	33.87% (9)	46.30% (10)
Linsbauer	-	-32.78% (6)	-89.21% (7)	-66.65% (8)	-52.99% (8)	28.31% (7)	39.72% (7)
Gantayat-v2	-	-	-	-	-	*18.96% (6)*	*23.74% (6)*
Brinkerhof-v2	-	-	-178.54% (11)	-	-	-	6.83% (1)
GCbedstress	-	-	-111.12% (8)	-38.83% (7)	-13.49% (4)	-	51.07% (12)
GCneuralnet	-	-	-57.11% (3)	36.73% (6)	64.61% (9)	37.33% (10)	72.00% (13)
RAAJglabtop	-	-	-	-	-	32.39% (8)	41.36% (8)
RAAJgantayat	-	-	-	*-14.20% (3)*	*8.00% (2)*	*-11.54% (3)*	*45.31% (9)*
McNabb	-	-4.08% (2)	-	-	-	-	-

Table 3-8 Comparison of relative MAE of thickness estimates (unit: m). '-' represents no value, Italic results are from velocity-based methods. Numbers within the brackets represent the rank in individual profiles. Red results have the top 3 performance.

Name	Corbassière	Columbia	SouthGlacier	NorthGlacier_1	NorthGlacier_2	Tasman	Unteraar
This Study	*32.70% (2)*	*17.65% (2)*	*63.63% (2)*	*9.58% (1)*	*19.49% (1)*	*39.11% (6)*	*47.50 (9)*
Gantayat	*31.57% (1)*	*35.72% (6)*	*69.25% (3)*	*15.12% (3)*	*37.48% (6)*	*62.19% (11)*	*42.68 (5)*
Farinotti	-	49.14% (8)	168.95% (10)	71.27% (9)	54.67% (8)	44.33% (8)	30.33 (4)
Huss	-	26.26% (4)	90.70% (6)	19.29% (5)	21.15% (2)	53.44% (10)	23.89 (1)
Morlighem	-	-	129.26% (9)	-	-	-	-
Maussion	-	47.90% (7)	61.78% (1)	12.52% (2)	26.53% (4)	26.53% (1)	28.08 (3)
Machguth	-	23.05% (3)	84.84% (5)	-	-	35.64% (3)	50.70 (11)
Linsbauer	-	33.99% (5)	91.28%(7)	66.65% (8)	53.03% (7)	37.17% (5)	43.76 (7)
Gantayat-v2	-	-	-	-	-	*31.00% (2)*	*43.40 (6)*
Brinkerhof-v2	-	-	180.80% (12)	-	-	-	26.98 (2)
GCbedstress	-	-	114.72% (8)	39.34% (7)	27.94% (5)	-	51.07 (12)
GCneuralnet	-	-	75.74% (4)	36.73% (6)	64.61% (9)	39.94% (7)	72.40 (13)
RAAJglabtop	-	-	-	-	-	36.26% (4)	44.34 (8)
RAAJgantayat	-	-	-	*16.68% (4)*	*23.51% (3)*	*45.93% (9)*	*48.03 (10)*
McNabb	-	14.36% (1)	-	-	-	-	-

Secondly, comparisons of the other 10 cross-sectional profiles were performed for Corbassière; it is clear that our model can restore most of the bedrock topography at Corbassière as shown in Figure 3-9. The statistical results are summarized in Tables 3-5 to 3-8. Although only *Gantayat et al.* (2014) and our method were implemented in this case. Our method provides better estimates of ice thickness.

In summary, over all of the 6 temperate glaciers, our method yielded an average error of 21.61 m (–0.57 m when excluding Unteraar). The average MAE was 46.61 m (24.28 m when excluding Unteraar). Among all the methods, we achieved top ranks in terms of both mean error and MAE for most of the tested glaciers. Additionally, we noticed that most of the thickness estimates from the previous velocity based method (*Gantayat et al*. (2014)) were overestimated which led to negative mean errors as can be seen from Figure 3-8. This was due to the different rate factor used in *Gantayat et al.* (2014). Overall, our proposed method provided more accurate ice thickness estimates in temperate glaciers using the same inputs used for other velocity-based methods.

(b). Nontemperate Glacier and Ice Cap

The proposed method was also tested for one non-temperate ice cap, Austfonna and one non-temperate glacier, Freya (see Figure 1 for their locations). Unlike temperate glaciers, a constant temperature offset of 7° C between the englacial temperature and the mean annual air temperature at equilibrium line altitude (ELA) was used to calculate the rate factor, A in non-temperate glaciers as discussed in section 3.3. The method was implemented over Austfonna and Freya as shown in Figure 3-10 and Table 3-9. The blue and red thick lines represent the surface and in-situ bedrock elevations, respectively. The other colorful lines represent the bedrock elevation estimates from other previous methods.

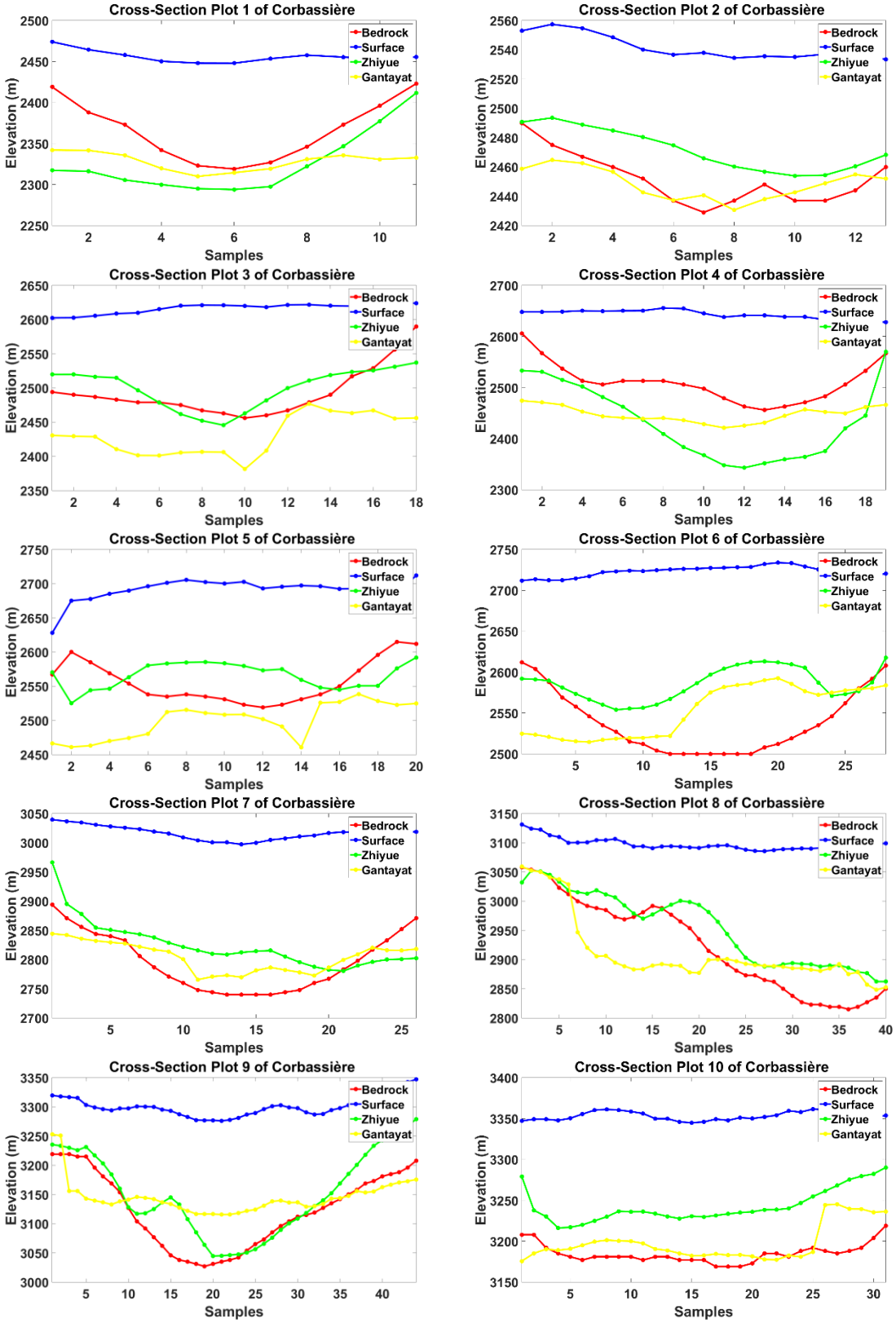

Figure 3-9 Comparison of bedrock elevations obtained from the glacier thickness estimates of this study (Zhiyue; green) and previous velocity-based method (Gantayat, yellow) along 4 cross-sectional profiles at Corbassière.

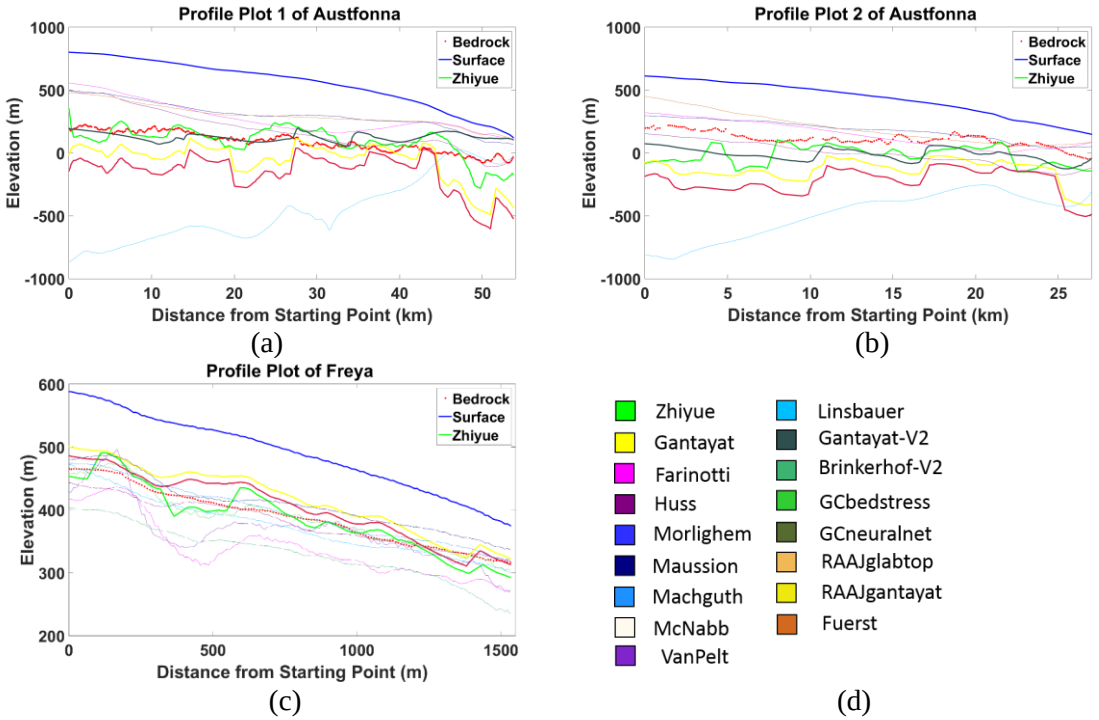

Figure 3-10 Comparison of bedrock elevations obtained from the estimated glacier thicknesses from this study (thick green line) and other previous methods (colorful lines) along 3 along-flow profiles (Austfonna, Freya).

The thick colorful lines are obtained using other velocity-based methods which are obtained from ITMIX (*Farinotti et al.*, 2017).

For Austfonna and Freya, our method achieved a high rank (top 5) for all of the statistics. Compared with the other three velocity-based approaches (Gantayat, Gantayat-v2, RAAJGantayat), our method showed better agreement with in-situ measurements. Thus, the proposed is promising for estimating thickness for non-temperate glaciers. However, more case studies are needed to validate the temperature offset for calculating T_{OET} for non-temperate glaciers.

3.4.3 Selection of Contour Interval

As described in section 3.4.1, we calculated the surface slope similar to the method

Table 3-9 Performance of thickness estimates from different method in Austfonna and Freya (unit: m). Italic results are from velocity-based methods. Numbers within the brackets represent the rank in individual profiles. Red results have the top 3 performance

Austfonna

Name	Mean Error (unit: m)		Relative Mean Error		MAE (unit: m)		Relative MAE	
	Profile 1	Profile 2	Profile 1	Profile 2	Profile 1	Profile 2	Profile 1	Profile 2
This Study	*73.96 (2)*	*-60.46 (2)*	*13.86% (2)*	*-21.95% (3)*	*93.38 (2)*	*74.36 (2)*	*21.92% (2)*	*25.86% (2)*
Gantayat	*-121.62 (4)*	*-248.12 (7)*	*-28.80% (4)*	*-82.36% (7)*	*132.54 (4)*	*248.12 (7)*	*31.75% (4)*	*82.36% (7)*
Farinotti	189.94 (5)	34.64 (1)	43.27% (5)	5.26% (1)	189.94 (5)	78.79 (3)	43.27% (5)	26.15% (3)
Huss	94.93 (3)	-117.56 (5)	17.28% (3)	-47.96% (6)	101.93 (3)	117.56 (5)	20.27% (3)	47.96% (6)
Linsbauer	-548.56 (8)	-590.04 (8)	-104.56% (8)	-189.08% (8)	554.78 (8)	590.04 (8)	106.79% (8)	189.08% (8)
Maussion	211.55 (7)	70.23 (3)	46.64% (6)	19.26% (2)	211.55 (6)	74.34 (1)	46.64% (6)	21.58% (1)
Gantayat-v2	*36.81 (1)*	*-121.19 (6)*	*13.42% (1)*	*-41.01% (5)*	*70.05 (1)*	*121.55 (6)*	*19.54% (1)*	*41.19% (5)*
Fuerst	209.86 (6)	86.81 (4)	47.91% (7)	22.42% (4)	209.86 (7)	98.47 (4)	47.91% (7)	28.34% (4)

Freya

Name	Mean Error (unit: m)	Relative Mean Error	MAE (unit: m)	Relative MAE
This Study	*-1.82 (1)*	*-3.29% (2)*	*14.63 (4)*	*17.92% (5)*
Gantayat	*23.01 (8)*	*21.82% (8)*	*23.15 (7)*	*23.15% (7)*
Farinotti	-50.27 (9)	-50.27% (9)	50.27 (9)	50.27% (9)
Huss	-9.48 (4)	-8.50% (4)	10.47 (3)	9.86% (3)
Linsbauer	-14.54 (5)	-14.64% (5)	14.77 (5)	14.83% (4)
Machguth	6.76 (3)	6.82% (3)	7.09 (1)	7.17% (2)
Maussion	20.13 (6)	21.24% (6)	20.13 (6)	21.24% (6)
VanPelt	-21.90 (7)	-21.74% (7)	25.23 (8)	24.78% (8)
GCbedstress	-2.35 (2)	-2.46% (1)	7.24 (2)	7.06% (1)
Brinkerhof	-57.26 (10)	-58.70% (10)	57.26 (10)	58.70% (10)

by *Gantayat et al.* (2014). However, instead of a 100 m contour interval, a combination of 20 m and 100 contour intervals was empirically chosen to calculate the slope. Different contour intervals from 20 m to 100 m were tested for along-flow profiles over the South Glacier and cross-sectional profiles of Corbassière as shown in Figure 3-11. For cross-sectional profiles, the 20 m contour lines led to more accurate thickness estimates with better spatial detail. The mean error of two cross-sectional profiles using 20 m, 30 m, 50 m, and 100 m contour lines was 19.92 m, 30.07 m, 35.14 m, and 45.79 m, respectively. Although differences over the along-flow profiles were not that significant, the error was reduced from –8.47 m to –3.05 m. However, it could be challenging to use 20 m contour intervals for debris-covered glaciers, such as Unteraar and Tasman. Due to the debris-

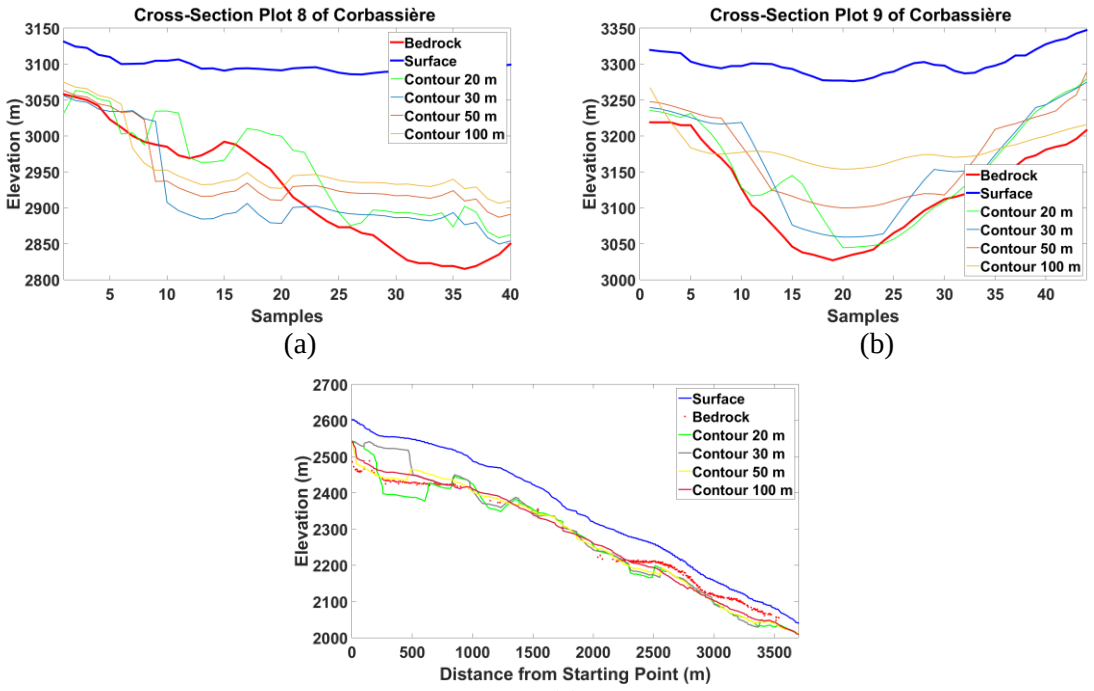

Figure 3-11 Comparison of bedrock elevations using different contour intervals along two cross-sectional profiles of Corbassière ((a) and (b)) and one along-flow profile in South Glacier (c).

covered features, it is difficult to directly use 20 m contour lines as the contour lines may merge (*Kamb and Echelmeyer*, 1986). In this case, we manually divided the glacier segments into different parts based on the shape of the contour lines and separately used 20 m and 100 m contour lines to calculate surface slopes.

3.4.4 Error Analysis

From all of the temperate and non-temperate glaciers, the overall mean error, relative mean error, MAE and relative MAE were 20.32 m, 8.55 %, 52.23 m and 30.59 %, respectively. As a comparison, the velocity-based method presented in *Gantayat et al.* (2014) yielded –39.26 m, –26.84 %, 71.07 m and 41.47 %, respectively. Additionally, the error distribution was summarized according to different velocities and slopes as shown in Figure 3-12. As the surface velocity increased, the mean error did not have a significant variation in the range of 0 m/year to 100 m/year. Since the number of estimates in fast-

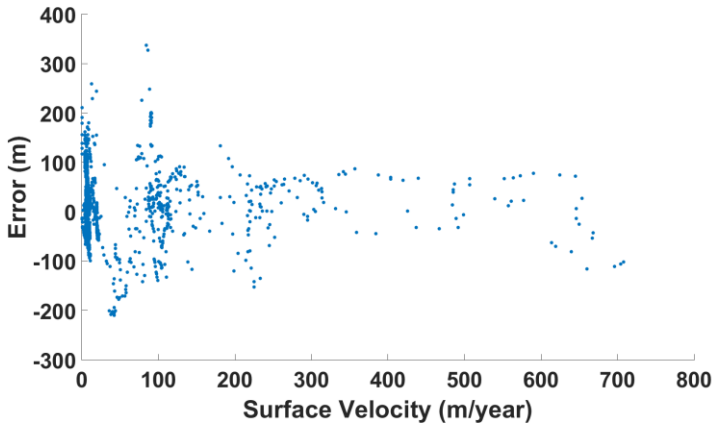

(a)

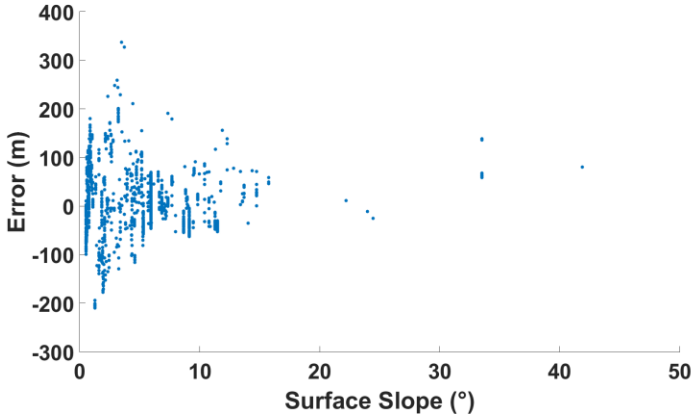

(b)

Figure 3-12 Distribution of deviation of thickness estimate error with respect to surface velocity (a) and surface slope (b). A total of 3023 samples are included in this figure covering all 8 test glaciers.

moving regions (velocity > 100 m/year) was insufficient, more case studies are required to determine the relationship between surface velocity and with thickness estimation error. On the other hand, the error decreased dramatically concerning the increasing surface slope, especially when the slope > 5°. To explain this finding, we examined the sensitivity of the thickness estimates with respect to the slopes, and performed a simulation using Eq. (3-9). The thickness variation versus the englacial temperature and f are displayed in Figure 3-13. The parameters used in the simulation are as follows: surface velocity $U_s = 80$ m/year; Glen's flow law rate factor $A = 2.4 \times 10^{-24}$ $\text{Pa}^{-3}\text{s}^{-1}$; $f = 0.8$; and density $\rho = 900$ kg m^{-3}, and slopes range from 0° to 70°. This indicates that for each component, the thickness

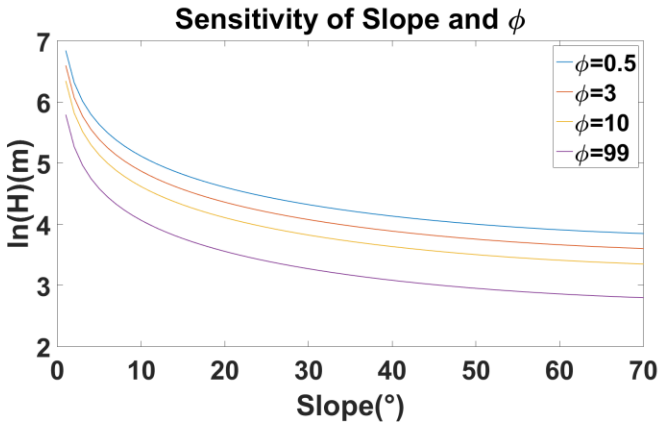

(a)

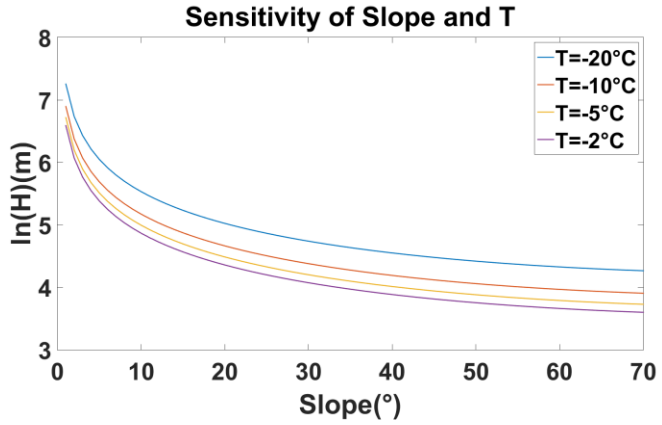

(b)

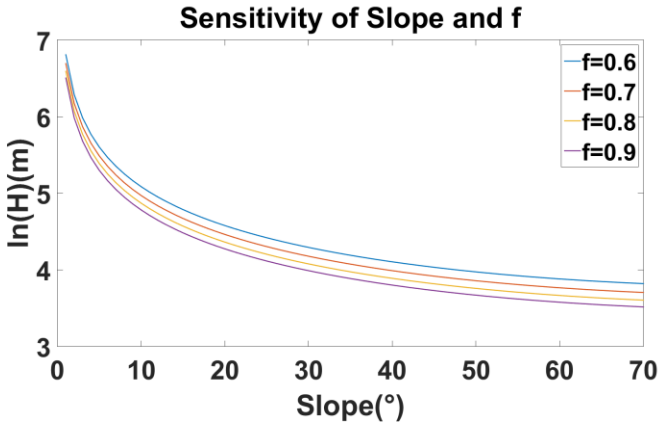

(c)

Figure 3-13 Logarithmic plot of simulated thickness estimate with respect to (a) surface slope and shape ratio ϕ, (b) surface slope and englacial temperature T, (c) surface slope and Nye shape factor f.

estimate become extremely sensitive as the slopes approach 0°. For example, if the slope is less than 5°, the magnitude difference between a different set of parameters could reach

hundreds of meters while this difference becomes negligible in steep regions (> 45°). Therefore, the proposed method is expected to provide better estimates for glaciers with larger surface slopes.

3.5 Conclusion

In this chapter, a new velocity-based iterative method was presented to estimate glacier thickness using surface velocity, surface topography and a pre-determined Glen's flow law rate factor as inputs. The surface velocities used in this study were either obtained via the speckle matching technique using ALOS PALSAR image pairs or provided by previous studies. The surface slopes were calculated using 20 m contour intervals derived from a DEM. The flow rate factor was found to be related to the englacial temperature. For temperate glaciers, an empirical englacial temperature of 273.0 K was obtained based on case studies over 6 different glaciers, corresponding to a rate factor of 11.38×10^{-24} $Pa^{-3}s^{-1}$. For non-temperate glaciers, a temperature offset of 7 °C between the englacial temperature and the surface air temperature was used, following the assumption of *Huss and Farinotti* (2012). The englacial temperature was therefore calculated using the annual surface air temperature acquired from the ERA-Interim reanalysis dataset. Then, we performed a comparison of estimated bedrock elevations obtained from our method and previous methods over 8 along-flow and 12 cross-sectional profiles of 6 temperate glaciers, 1 non-temperate glacier and 1 non-temperate ice cap. Besides the underestimated error from our method over Unteraar due to its significant debris cover, the proposed method obtained better estimates than most of the previous methods and significantly improved the mean error and mean relative error from –39.26 m, –26.84 % to 20.32 m, 8.55 %, compared to

the previous velocity-based method from *Gantayat et al*. (2014). However, as an empirical parameter, the rate factors for both temperate and non-temperate glaciers are expected to be improved once more in-situ data become available.

Additionally, the selection of the contour line interval for calculating surface slope was discussed. The 20 m contour line used in this study is found to preserve more spatial details of the ice thickness, especially in the cross-sectional direction. However, for certain cases, such as debris-covered surfaces, a combination of 20 m and 100 contour lines was suggested. Finally, an error analysis was performed on surface velocity and slope. The influence of velocity was not clear and more tests are needed for fast-moving glaciers.

Surface slope turned out to have a significant influence on thickness estimates. The error decreases dramatically as a function of increasing surface slope. Furthermore, a sensitivity analysis on the slopes was performed, and similarly, the estimated thickness was very sensitive to surface slope in relatively flat areas (slope < 5°). Therefore, our proposed method is expected to have better performance in steep regions.

Compared with previous velocity-based methods, the proposed approach improved the accuracy of ice thickness estimate without introducing additional inputs. As this method is based on spaceborne remote sensing observations, it is promising that the proposed method can provide a spatial distribution map of ice thickness estimates in multiple glacierized areas where in-situ data are limited, such as over the Himalaya region.

4 Traditional Technique of Estimating Ice Loss in Glaciers: Case study in Novaya Zemlya.

4.1 Background & Data

The Russian Arctic contains the 6th largest glacierized area (51,784 km^2) with more than 1,000 glaciers (*Radić et al.*, 2014). Recent studies indicate that the Russian Arctic has experienced an ice mass loss rate of –6.6 Gt year^{-1} during 2012–2014 (*Melkonian et al.*, 2016). For a 60-year analysis from 1952–2012, the glaciers exhibited half the retreat speed compared with the recent 3-year observation from 2012–2014 (*Melkonian et al.*, 2016). In this century, the contribution of the mountainous glaciers and ice caps to global ice mass loss is expected to increase by 200–300 %. Ice melt in the Russian Arctic would be the 3rd largest contributor among all glacierized regions by 2100, which will perhaps increases the sea level rise by 20.29 to 28.31 mm (*Melkonian et al.*, 2016; *Radić et al.*, 2014). The Russian Arctic consists of three major glacier regions, Franz Josef Land, Severnaya Zemlya and Novaya Zemlya (NVZ). Of these three areas, NVZ contains the largest glacier area (22,100 km^2) and has been experiencing the greatest ice mass loss of –5.8 Gt year^{-1} from 2004 to 2009 (*Moholdt et al.*, 2012). Figure 4-1 presents the location and surface features of NVZ with 22,100 km^2 glaciated area shown in white. The red and blue outlines indicate basin areas of marine-terminating glaciers for our study and Melkonian et al. (2016) respectively. Topography and bathymetry are both from the International Bathymetric Chart of the Arctic Ocean (IBCAO, http://www.ngdc.noaa.gov/mgg/ bathymetry /arctic/), and glacier outlines are from National Snow and Ice Data Center (NSIDC) GLIMS glacier database (http://glims.colorado.edu/glacierdata/). The star indicates the location of the

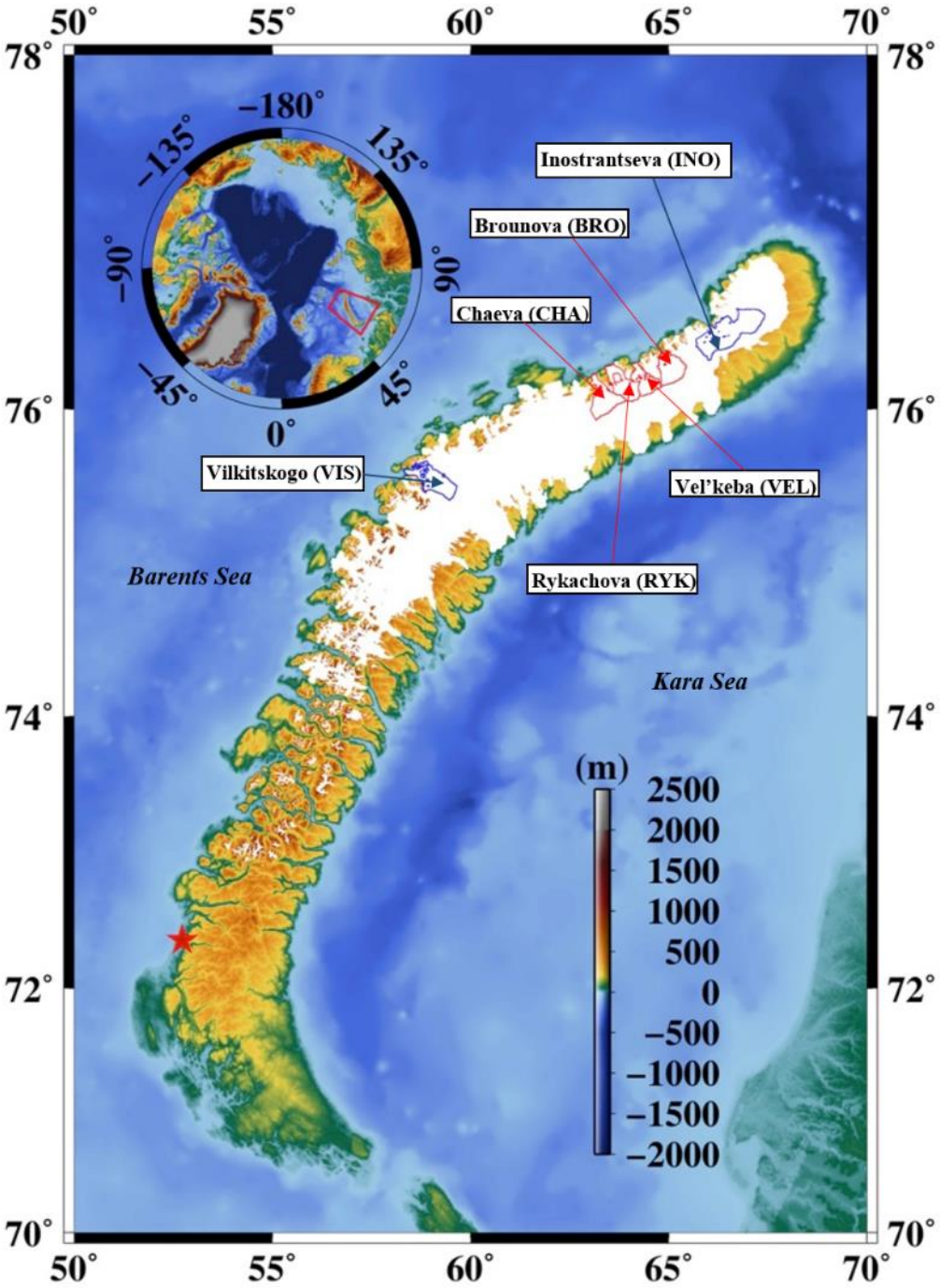

Figure 4-1 Location and surface features of Novaya Zemlya (NVZ)

Malye Karmakuly meteorological station. For NVZ, there is only one meteorological station with long-term records at Malye Karmakuly (star in Figure 4-1) (*Carr et al.*, 2014; *Zhao et al.*, 2014). Sparse temperature data are available for NVZ after 2000 (*Zhao et al.*, 2014). Moreover, there is no long-term in situ snowfall or snow depth data available in NVZ. Only a few glacier observation campaigns have provided observations on the retreat of the frontal positions (*Sharov*, 2005). In essence, spaceborne geodetic and remote sensing data become the only viable data source to investigate the dynamics of the ice mass changes in NVZ. For example, *Sharov* (2005) investigated the velocity variation of the frontal position of six glaciers in NVZ using Interferometric Synthetic Aperture Radar (InSAR) techniques with ERS-1/2 tandem (1-day temporal baseline) pairs. This study also indicated a substantial decrease in ice coastline length of –7.9 % from 1950 to 2000. On the other hand, the offset-tracking method (*Strozzi et al.*, 2002) has been more commonly used to estimate glacier velocity due to decorrelations in interferograms, especially over fast-moving glaciers. Over NVZ, *Strozzi et al.* (2008) used L-band JERS-1 SAR images to estimate the glacier velocities along the northern coast. The estimated frontal position velocity reached about 250 m $year^{-1}$. Although the weather conditions (persistent cloud cover) of NVZ leads to limited availability of satellite optical images, *Melkonian et al.* (2016) combined all available optical image pairs between 2000 and 2014 from WorldView, Landsat and ASTER, and estimated the stream velocities over 4 glaciers along NVZ's northern Barents Sea coast. The maximum frontal velocity reached 1 km year-1. However, the glacier velocities in the period of 2007–2010 were not generated due to the lack of data. Glacier elevation changes have also been obtained with Ice Cloud and land Elevation Satellite (ICESat) data and were estimated to be –0.38 ± 0.06 m year-1 from 2003 to 2009 over the

entire island (*Moholdt et al.*, 2012). Besides the ICESat data, Digital Elevation Models (DEMs) generated from WorldView, and ASTER images have been co-registered to ICESat dataset and produced additional elevation change rates (*Melkonian et al.*, 2016). *Matsuo and Heki* (2013) obtained an ice mass loss rate of –5.2 ± 3.9 Gt year-1 from 2004 to 2012 using GRACE data while Moholdt et al. (2012) obtained ice mass loss of –9.8 ± 1.9 Gt year-1 and –7.1 ± 5.5 Gt year-1 for the period of 2004–2009 using ICESat and GRACE data, respectively.

A recent study indicates that the marine-terminating glaciers experienced an accelerated retreat in NVZ, especially the ones on the Barents Sea coast (*Carr et al.*, 2014; *Carr et al.*, 2017). *Melkonian et al.* (2016) proposed that the calving flux made a major contribution to the glacier retreat of Barents coast marine-terminating glaciers. However, the influence of influx on mass change has not been discussed. Hence, in this study, the contributions of influx and outflow to ice loss are fully investigated for marine-terminating glaciers, and 4 marine-terminating glaciers were chosen on the Barents Sea coast as study areas (red outlines in Figure 4-1). These 4 glaciers are located between the two marine-terminating glaciers studied by *Melkonian et al.* (2016) (blue outlines in Figure 4-1). We calculated glacier stream velocity to represent the outflow, and air temperature and sea surface temperature (SST) were obtained to investigate their influences on velocity changes. In addition, snow depth estimates were used to represent the mass influx for the study glaciers, and changes in elevation and mass were obtained via radar altimeter and GRACE data, respectively. Combining the mass influx and the net change with the outflow represented by velocity variation, we were able to clarify the contribution of influx and outflow to mass changes in a more comprehensive way. Overall, observations from

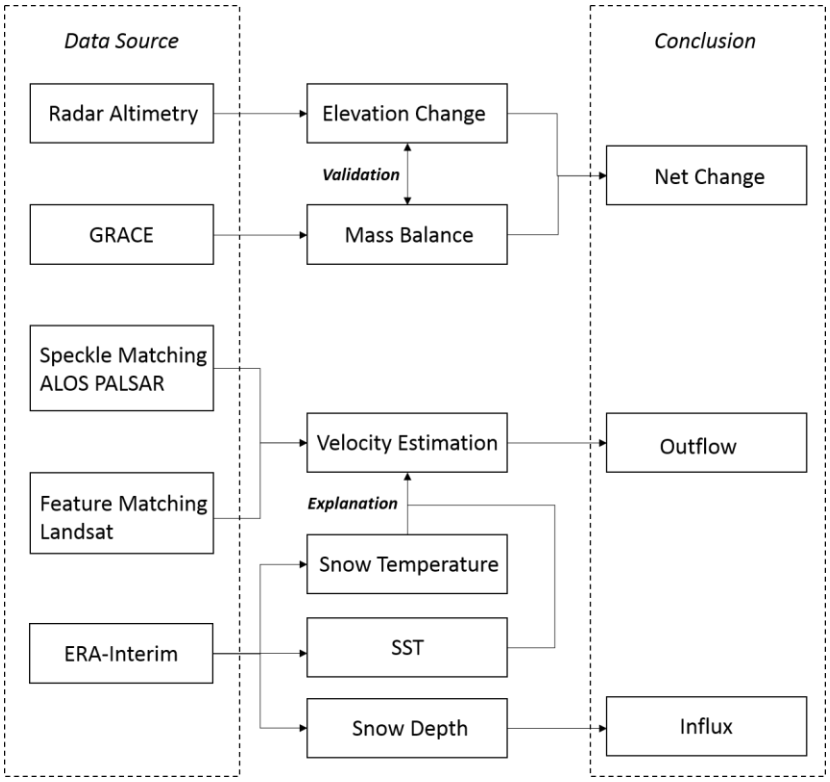

Figure 4-2 Overall flow chart of this case study.

multiple spaceborne geodetic instruments including Envisat RA-2, ALOS PALSAR, Landsat, and GRACE, and ERA-Interim model were processed from 2002 to 2014. Figure 4-2 summarize the overall analysis flow of this study.

4.2 Techniques & Data

4.2.1 Ice Mass Changes from GRACE

The GRACE Release 05 (RL05) data provided by the Center for Space Research (CSR) (ftp://podaac.jpl.nasa.gov/allData/grace/L2/CSR/RL05/) was used to generate a glacier mass change time series over the entire NVZ. The missing degree one coefficients (geocentric offset) in the data have been added using values calculated based on ocean and atmospheric models and GRACE coefficients for degrees 2 and higher (*Swenson et al.*,

2008). The C20s (Earth's oblateness) are replaced by estimates from satellite laser ranging (*Cheng et al.*, 2013). Although some improvements have been made to RL05 data over previous versions resulting in reduced north/south stripes and east/west banded errors in the spatial domain (*Yi and Sun*, 2014), a filtering process is still needed to get clear signals. Consequently, we applied a decorrelation filter (*Duan et al.*, 2009), and a Gaussian smoothing with a 300 km radius (*Guo et al.*, 2010). Since the signals over land and ocean are both averaged for the smoothing, there is signal leakage from land to ocean. To eliminate this leakage error, a ocean signal is assumed to be significantly smaller than the land signal, and the effect of stripes was eliminated during the smoothing procedure (*Guo et al.*, 2010). The leakage signal was recovered by rescaling the Gaussian-smoothed mass change result (*Guo et al.*, 2010). This was done in order to obtain a similar result similar to applying Gaussian smoothing separately to land and ocean signals. The contribution of Glacial Isostatic Adjustment (GIA) was also removed using the model provided by *Geruo et al.* (2013).

4.2.2 Elevation Changes from Envisat RA-2 Radar Altimetry

Satellite radar altimetry has been extensively used to estimate ice-sheet elevation changes through either crossover or collinear analysis (*Davis*, 2005; *Lee et al.*, 2012; *Wingham et al.*, 1998). Although it is challenging to obtain reliable altimeter measurements over mountain glaciers with rough terrain and steep slopes due to its large footprint size (3–5 km in radius), *Lee et al.* (2013) have successfully applied a collinear method with TOPEX/Poseidon and Envisat RA-2 radar altimetry data over the Bering Glacier in Alaska and observed changes in its elevation trends during the period from 1992–2010. In this study, due to the lack of crossover points, a collinear analysis was adopted with Envisat

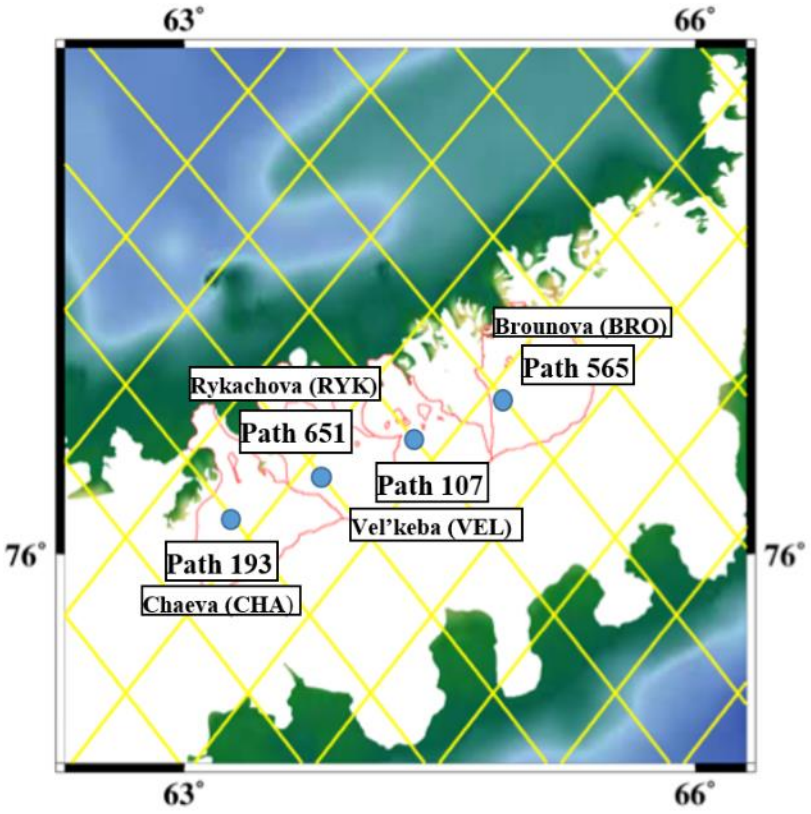

Figure 4-3 Envisat altimetry ground tracks (yellow lines) over the northern NVZ.

RA-2 data and a time series of elevation changes over the glaciers in NVZ (Figure 4-3) was generated. Blue circles indicate the locations where Envisat altimetry time series were generated. Red outlines represent our study glacier basins. All of these 4 glaciers are marine-terminating. A summary of the collinear method is provided here.

The 18-Hz (~350 m along-track sampling) ICE-1 retracked measurements from the Envisat RA-2 Geophysical Data Record (GDR) were used to obtain elevation changes in this case study. The observation period was from cycle 9 to 93 (April 2002–September 2010) with a 35-day repeat period. Figure 4-3 shows the coverage of Envisat altimetry tracks over NVZ with 4 locations where successful elevation change time series were obtained. The collinear method simply stacks the altimetry data obtained from repeated

Table 4-1 List of available ALOS PALSAR images over study area.

Scene No.	Observation Date
ALPSRP100161530	2007/12/11
ALPSRP106871530	2008/01/26
ALPSRP153841530	2008/12/13
ALPSRP160551530	2009/01/28
ALPSRP214231530	2010/01/31
ALPSRP220941530	2010/03/18

cycles. Nonetheless, a surface gradient error is introduced due to the drift in satellite tracks between cycles (*Lee et al.*, 2008). Typically, this error can be eliminated by using a DEM for the so-called surface gradient correction (*Lee et al.*, 2012, 2008). However over mountainous regions, as the altimeter presents the average elevation within one footprint, the error caused by the spatial difference between DEM and altimeter footprint increases due to surface roughness (*Lee et al.*, 2013). Therefore, *Lee et al.* (2013) proposed a method to use the average of all of the available altimeter elevations as the reference DEM to apply the surface gradient correction which would eliminate the error due to the differences between the DEM spatial resolution and altimetry footprint size. For more details, readers are referred to *Lee et al.* (2013).

4.2.3 Glacier Velocity from PALSAR Speckle-matching

In the previous study done by *Melkonian et al.* (2016), the glacier velocities at NVZ for the period from 2007–2010 were not generated using optical image pairs. To fill this gap, we estimated the velocities by applying a speckle matching method to pairs of ALOS PALSAR fine-beam mode images (Table 4-1). For each glacier, three pairs of PALSAR images were available between 2007 and 2010. In this study, different patch window sizes (20×60, 10×30, 5×15, 3×9) were examined, and a size of 5×15 pixels was found to be the define suitable. Next, the search area size was set based on an initial estimation of the

glacier velocity. For NVZ, the velocity can reach as fast as 400 m/year near the frontal position (*Strozzi et al.*, 2008). This maximum velocity corresponds to 100×300 pixels after converting it into a pixel scale. In this study, the search area was slightly increased to 120×360 pixels to avoid any potential systematic error. To determine the relative SNR threshold, the values from 0.05 to 1.0 were iteratively tested with 0.05 increment to ascertain the most suitable value, and the correlation SNR threshold was set to 0.2, which corresponds to a SNR of 2.0.

4.2.4 Glacier Velocity from Landsat Feature Offset-tracking

Feature tracking was applied to obtain surface velocity using Landsat 7 ETM+ images. The principles of feature tracking are given in section 2.1. The application of this approach with Landsat 7 ETM+ images is complicated by the fact that the scan line corrector (SLC) had failed on Landsat 7 as of May 31, 2003. The SLC failure, or SLC-off, results in a blank strip pattern within Landsat scenes that is subject to approximately 20% data loss. These stripes effects the computation of correlation because the blank is considered as ‘zero’, producing a correlation peak that is much less distinct. ETM+ pairs (Pairs 2 and 3 in Table 4-2) and FFT based cross-correlation for 2002 Landsat 7 and Landsat 8 pairs (Pairs 1 and 4 in Table 4-2), were calculated. Image registration was applied once the displacements were computed. This process removed the registration error between pairs and is known to be 2 – 3 times larger than sole correlation error. This was done by removing any motion in known stationary areas, and these x-y offsets were then applied to the displacements.

Table 4-2 List of Landsat pairs. Landsat 7 ETM+ for pair 1, 2 and 3 and Landsat 8 for pair 4.

Pair	Image 0	Image 1	Year	Day separation (days)
1	LE71770062002088EDC00	LE71760062002145SGS00	2002	58
2	LE71770062004190ASN01	LE71780062004229ASN01	2004	40
3	LE71790052006113ASN00	LE71770062006179ASN00	2006	67
4	LC81760062013083LGN02	LC81760062013119LGN01	2013	37

4.2.5 Atmospheric and Oceanic Observations from ERA-Interim

According to a recent study, ice dynamics have been the major contribution to mass loss and frontal retreat in the glaciers along NVZ's Barents Sea coast, and these mass losses and frontal position retreats were influenced by atmospheric and oceanic conditions (*Carr et al.*, 2014). Therefore, an attempt was made to discover the relationship between glacier stream velocity and these contributing factors. In order to obtain the atmospheric and oceanic parameters, ERA-Interim reanalysis data (http://apps.ecmwf.int/datasets/) was used. Three monthly-mean-of-daily- mean products, namely, air temperature, SST and snow depth were extracted from the period from January 1979 to June 2015. The air temperature data represents the temperature at 700 hPa geopotential height instead of at 2 m height. This set of data presents a higher correlation with ground station data in the Arctic (*Carr et al.*, 2014; *Moholdt et al.*, 2012). The spatial boundary was set to be from 63.9°E to 64.6°E and 76°N to 76.4°N with a 0.1°×0.1° grid of the Gridded Binary (GRIB) data processed by the portal. 40 grids were averaged to obtain mean air temperatures. For SST estimation, a part of the Barents Sea (49.5°E to 70.5°E, 75°N to 78°N) was selected, and 145 grids were averaged to obtain mean SSTs with a resolution of 0.75°×0.75°. On the other hand, the grid resolution for snow depth was set to be 1.5°×1.5° due to limitations of data quality and accuracy. The spatial boundary was set to be from 54°E to 65°E and 72°N

to 78°N in order to obtain more grid samples. For all three climatic variables, the Grid Analysis and Display System (GrADS) was utilized for analysis and post-processing (*Doty and Kinter III*, 1995).

4.3 Results and discussion

4.3.1 NVZ Mass Changes

To understand the contribution of outflow and influx to mass loss, it is necessary to assess the mass changes over the study area. To obtain monthly mass balance estimates, GRACE EWH anomalies were multiplied by the entire NVZ area (79,970 km^2) and a time series of mass changes was generated as in Fig. 4-4. A mass loss of –1.04 ± 0.25 Gt/year was observed in 2003–2014. In order to analyze the details of mass changes, the entire 2003–2014 period was divided into three periods: two strong interannual negative mass trends from 2003–2007 (–5.94 ± 0.97 Gt/year) and 2010–2014 (–7.06 ± 1.04 Gt/year), and a relatively weak interannual positive mass trend in 2007–2010 (4.26 ± 0.96 Gt/year). The mass loss in the period of 2003–2007 was also observed by Moholdt et al. (2010) with a rate of –5.8 ± 3.0 Gt/year from 2004–2009, while the mass loss in 2012–2014 was reported by *Melkonian et al.* (2016) with a rate of –6.6 ± 1.4 Gt/year. Therefore, the mass change estimates from GRACE in this study agree well with previous studies. However, the slight mass gain from 2007–2010 has not been reported in previous studies.

4.3.2 NVZ Surface Elevation Changes

Besides the mass anomalies obtained from GRACE data, the trends in elevation changes can also indicate the trends in mass change. The elevation change time series

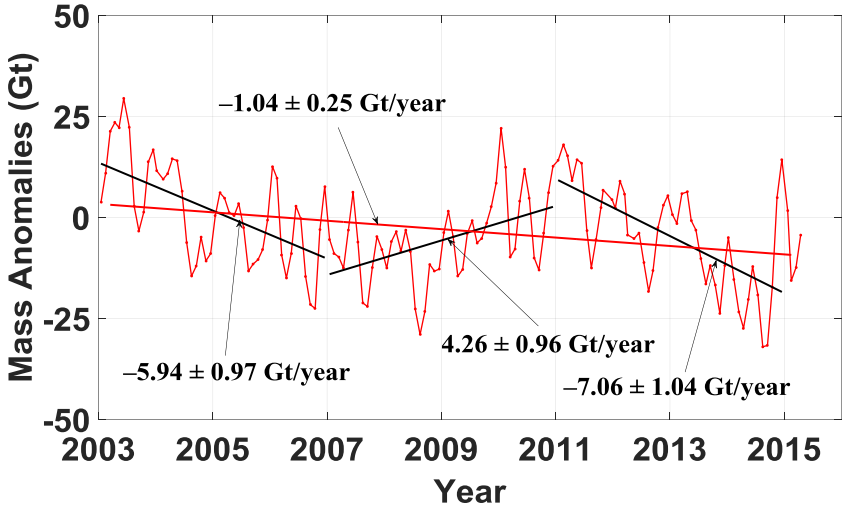

Figure 4-4 Time series of mass changes over the entire NVZ observed by GRACE in 2003–2014. The uncertainty represent 1–σ error from least squares.

obtained from Envisat radar altimeter over the 4 study glaciers are shown in Fig. 4-5. An overall decrease in elevation was observed from 2003 to 2007, followed by an increase. The decreasing trends range between –0.66 to –1.56 m/year, and the increasing trends range between 0.74 to 0.96 m/year. Although the drop between 2003–2007 has also been observed in a previous study (*Moholdt et al.*, 2010), the notable increase in 2007–2010 has not been reported.

Similarly, *Moholdt et al.* (2012) estimated the average elevation change rate over the entire NVZ's glacierized area using ICESat data from October 2003 to October 2009 with a rate of –0.38 m/year. For the purpose of comparison, an elevation change rate of –0.29 m/ was obtained during the same period using the average of all 4 Envisat time series. Although the difference in the elevation change rates may be due to the different spatial and temporal coverages of ICESat and Envisat time series, they agree reasonably well.

From Figure 4-4 and Figure 4-5, it is evident that similar trend variations from 2003–2010 are observed in both the altimeter elevation changes and GRACE mass changes.

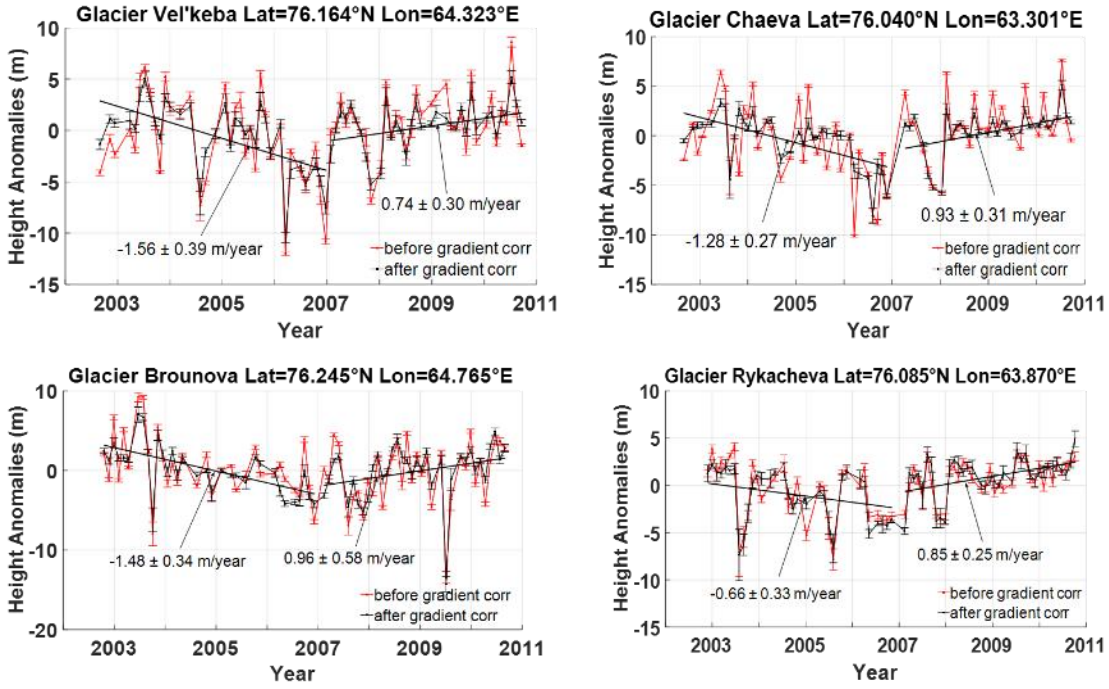

Figure 4-5 Time series of elevation changes over the 4 glaciers in northern NVZ using Envisat RA-2 data.

In addition to the comparison with the previous studies, this qualitative consistency between these two independent datasets suggests that both the Envisat and GRACE time series estimated can be considered reliable.

4.3.3 NVZ Glacier velocity

Figure 4-6 and Figure 4-7 illustrate horizontal velocity vectors and velocity variations extracted along the profile lines (light blue lines in Fig. 4-6) over each glacier. The backgrounds in Figure 4-6 are PALSAR amplitude images. The red circles in each plot in Figure 4-6 represents the locations where Envisat time series have been generated using PALSAR speckle matching. In Figure 4-7, the velocities were sampled at an interval of 100 m (orange points in Figure 4-6) along the profile lines. The stream velocity was observed to be about 150 m/year, while at the frontal position, the velocity may reach over

400

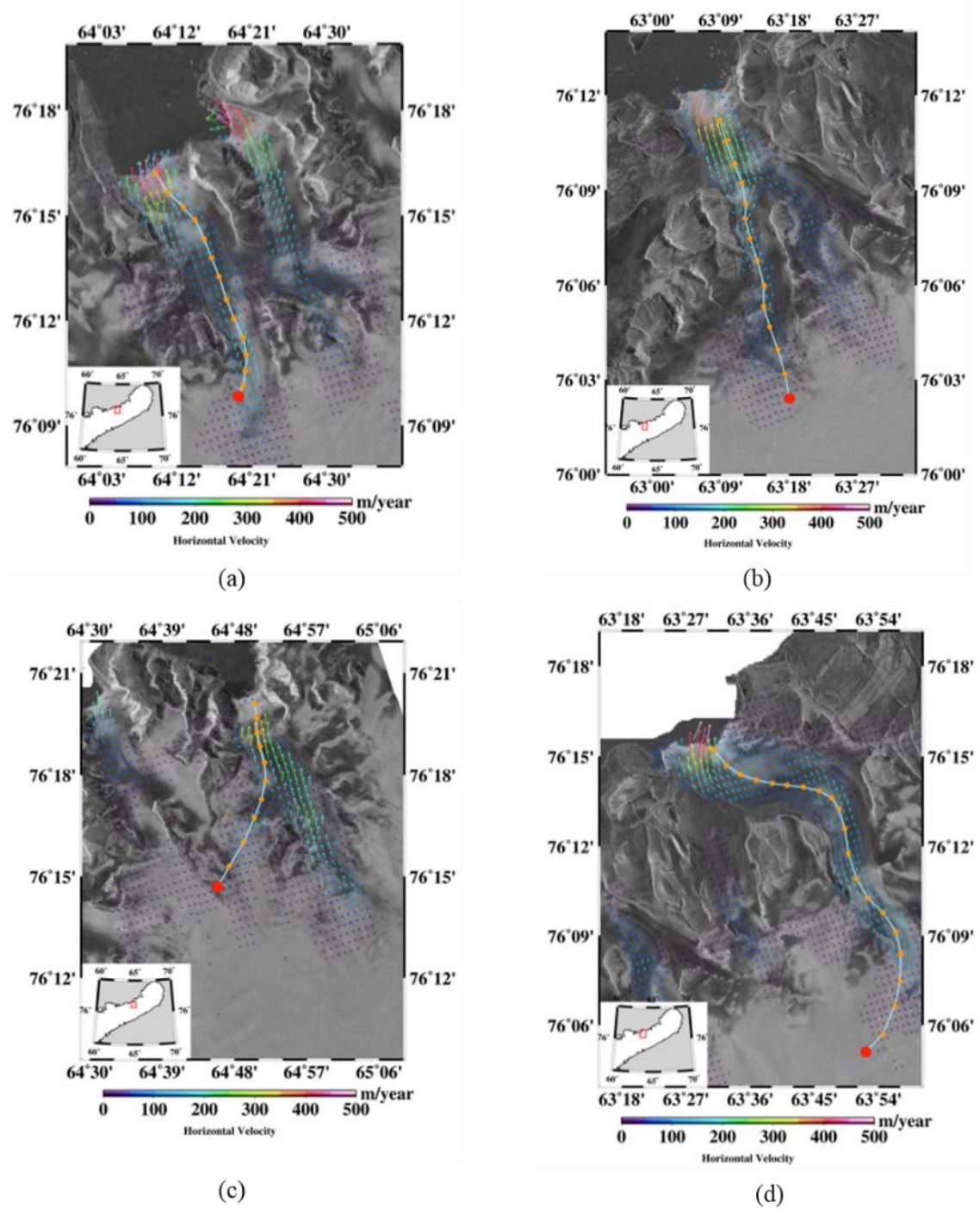

Figure 4-6 2007 winter velocity vector plots of (a) Glacier Vel'keba, (b) Glacier Chaeva, (c) Glacier Brounova, (d) Glacier Rykacheva generated from the speckle matching technique.

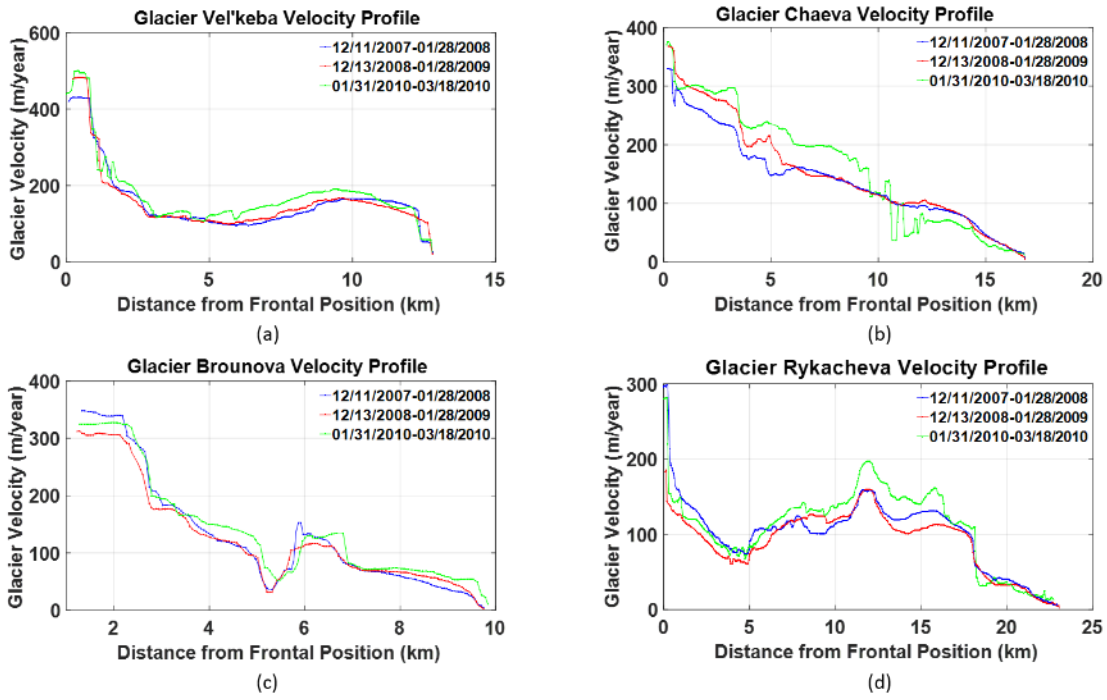

Figure 4-7 Velocity profiles for 2007–2010 on 4 study glaciers, (a) Glacier Vel'keba, (b) Glacier Chaeva, (c) Glacier Brounova and (d) Glacier Rykacheva from PALSAR speckle matching.

m/year.

By comparing velocity changes between December of 2007 and March of 2010, over all 4 NVZ glaciers, the velocities between December and January of both 2007 and 2008 were discovered to be approximately identical, and January–March of 2010 had a slight increase of about 50 m year^{-1}. However, since the observation periods are different, differences in temperature could play a significant role in these velocity variations (see section 4.3.4).

The random error in the cross-correlation speckle matching was derived by Bamler (2000) as

$$\sigma_{x,y} = \sqrt{\frac{3}{2N}} \frac{\sqrt{1-\gamma^2}}{\pi\gamma} \mathrm{osf}^{3/2} , \qquad (4\text{-}1)$$

where $\sigma_{x,y}$ represents the standard deviation of the range or azimuth offset estimate (unit:

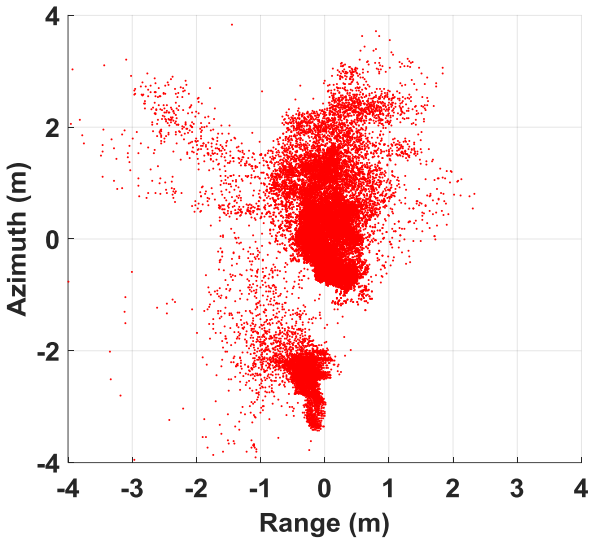

Figure 4-8 Estimated displacement error from speckle matching using three PALSAR 46-days pairs (2007–2010) over a stationary region.

pixel), N is the number of pixels in the matching window (5×15=75), γ is the coherence of the corresponding interferometric window data pair, and osf is the oversampling factor. Using Eq. (4-1), mean uncertainty of about 0.15 pixels was obtained, which corresponds to about 6 m year^{-1} and the maximum random error reached 30 m year^{-1}. In addition to the statistical error estimation, we also estimated the error using a stationary region of NVZ. The large rocky region (14.54 km^2) near Glacier Rykacheva was selected to plot the displacements along the range and azimuth directions over 40,033 points (Figure 4-8). The mean stationary error was 4, 26, and 4 m/year for 2007, 2008, and 2010, respectively. The overall mean stationary error was estimated to be approximately 10 m/year.

To obtain more estimates of glacier velocities, Landsat images (available from http://glovis.usgs.gov) were also processed using the feature tracking method. In total, 4 pairs (listed in Table 4-2) were used in this study. The size of the master subset was 101×101 pixels, and the size of the slave subset was set according to temporal separation, not exceeding 800 m/year. The reason for using a larger subset than the usual size of 31×31

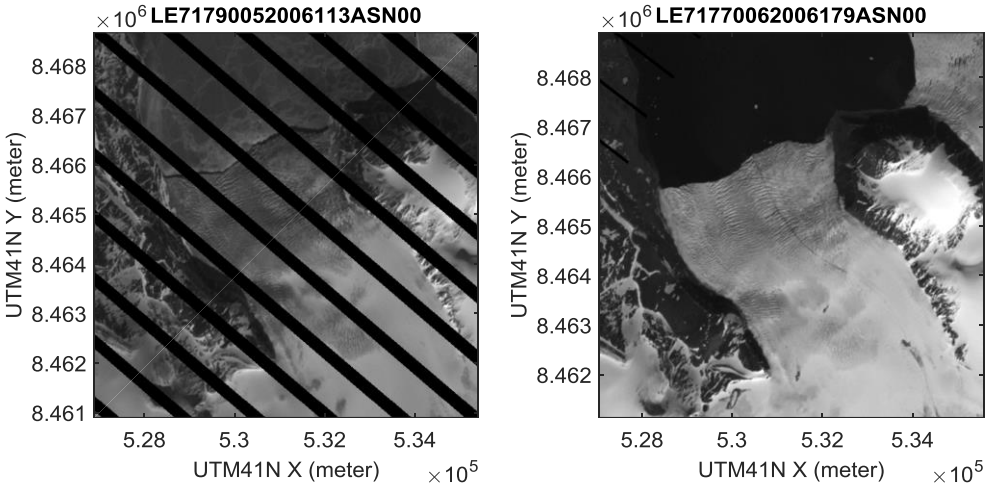

Figure 4-9 Landsat ETM+ SLC off pair 3.

to 51×51, was to ensure obtaining unique SLC-off image correlation (Figure 4-9).

Figure 4-10 shows a cross section of 4 velocity profiles from 2002 to 2013 obtained by bilinear interpolation. It can be seen that the velocity profile around 6 km upstream shows that the feature tracking failed mostly due to the featureless smooth glacier surface. The profiles from 2002, 2004 and 2006 showed no change in speeds. On the other hand, the speed increased by almost a factor of two in 2013 compared to the previous three velocity profiles.

Errors in feature tracking can be divided into two parts – image registration error and correlation error. Registration error comes mainly from the ortho-rectification process and can be removed by analyzing motion of stationary features such as rocks. *Dietrich et al.* (2007), *Lee et al.* (2004) and *Skvarca et al.* (2003) estimated the registration error to be 0.1, 0.3 and 1.5 pixels respectively. The correlation error comes from a quadratic surface fitting of the correlation map around a peak and has been shown to be 0.1–0.3 pixels by *Dietrich et al.* (2007), *Heid and Kääb* (2012), and *Berthier et al.* (2005).

A simple x – y offset registration technique was used due to difficulties in obtaining a good distribution of control points, poor image quality and outliers in velocity extraction.

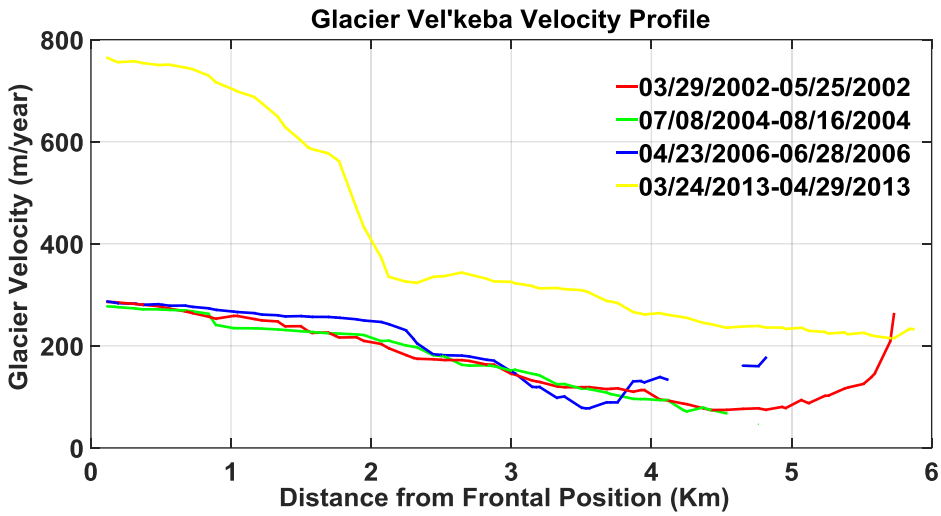

Figure 4-10 Velocity profiles over Glacier Vel'keba using feature offset-tracking from 2002–2013.

However, an affine or polynomial transformation would more effectively remove registration errors if multiple control points were used (*Ahn and Howat*, 2011). A common area (green rectangle in Figure 4-11 that is near the area of interest was used, for all pairs and computed their means (1.7, 0.79, 3.9 and 3.5 pixels) and standard deviations (0.08, 0.17, 0.08 and 0.06 pixels)), were computed for 2002, 2004, 2006 and 2013, respectively. Control point registration error has been estimated to be 0.1 pixels. However, considering the poor distribution of control points and the simple offset registration method, an uncertainty of 0.5 pixels was adopted as for a conservative registration error. Since one single correlation peak is searched using a 3×3 quadratic surface fitting, it is difficult to quantify the correlation error. Consequently, 0.2 pixels was used for the correlation-matching uncertainty as a conservative estimate following (*Ahn and Howat*, 2011).

The total uncertainty, which is the squared sum of these two uncertainties, is 0.54 pixels. For conversion of pixel displacements to metric units, we used the Landsat pixel resolution (15 meters) and the time separation of each pair. Combining these two errors

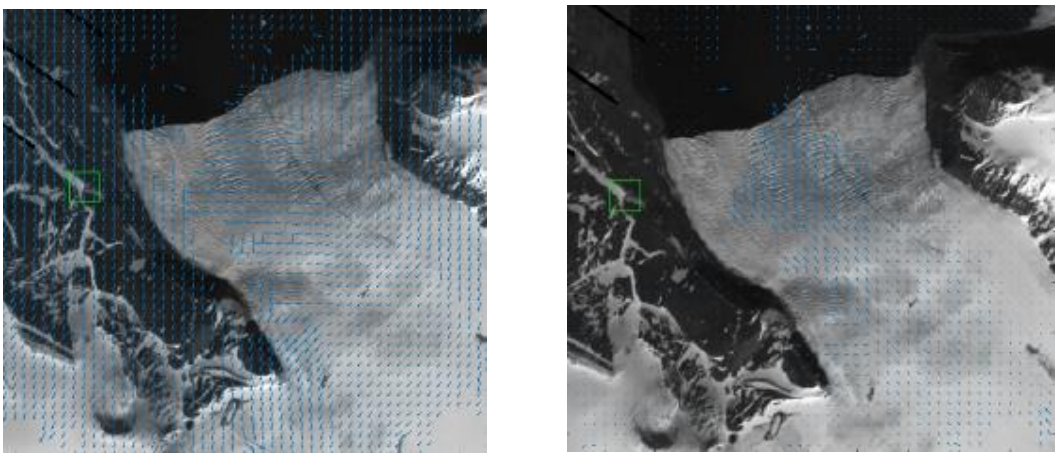

Figure 4-11 Registration example of 2013 pairs – before registration (left) and after registration (right).

provided 1-σ errors of 34, 50, 30, and 54 m/year for 2002, 2004, 2006 and 2013, respectively.

4.3.4 Atmospheric and Oceanic Influence on Glacier Stream Velocity

The air temperatures from ERA-Interim were examined to investigate whether the glacier velocity was influenced by seasonal air temperature variation. According to Glen's flow law, glacier velocity correlates with surface temperature. Also, since most of the velocity estimates were obtained during the winter period for NVZ (October to March), the winter season 700 hPa air temperature was chosen to compare with glacier velocities as this product correlates better with Arctic ground station data elsewhere (*Carr et al.*, 2014). Winter temperature variation (Figure 4-12) was generated by averaging all pixels within the spatial boundary. The red line represents monthly temperature variation and the blue line represents annual winter temperature variation (November to March). As can be seen from Figure 4-12, between 2001 and 2003, a slight decrease in winter temperature was observed. This was followed by an increase in winter air temperature of approximately

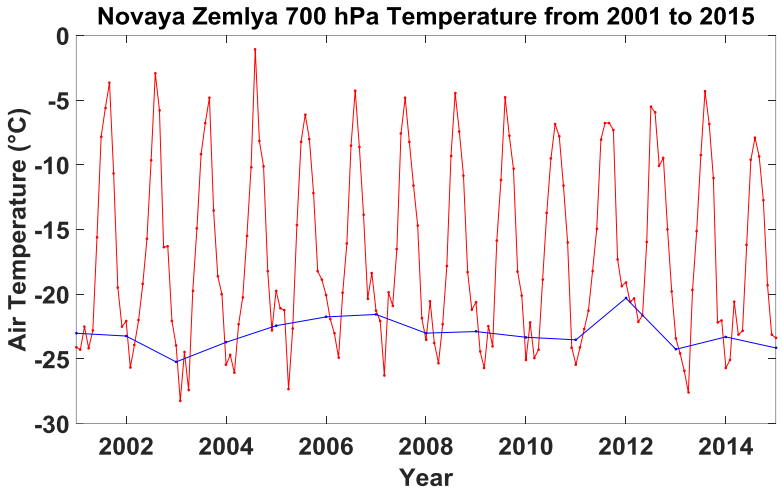

Figure 4-12 Time series of air temperature obtained from ERA-Interim data in 2000–2014 over the NVZ northern glacier area (63.9°–64.6°E, 76°–76.4°N).

5 °C between 2003 and 2007. After that, the winter air temperature was stable except for a slight increase in 2012. Overall, the winter air temperature in the period of 2001–2014 has not experienced a significant change.

In order to investigate correlation between air temperature and velocity, the velocities were collected over the Glacier Vel'keba which were estimated from speckle matching for 2007, 2008, and 2010 and feature tracking for 2002, 2004, 2006, and 2013 (Figure 4-13). The dash-dot lines represent the velocities generated using feature tracking, and the solid lines represent velocities generated using speckle matching. The velocity in 2013 was significantly faster than other years. Green square indicates control point area. Since the data observation dates for each velocity estimate are not identical, we need to eliminate the effect of seasonal temperature variations on estimated velocity. According to Glen's flow law, the glacier flow velocity can be described as (*Glen*, 1959)

$$u = k \cdot \tau^n , \tag{4-2}$$

where u is the glacier shear strain (flow) rate, k is a temperature-dependent constant which varies due to local conditions, τ is the glacier stress, and n is a constant between 2–4

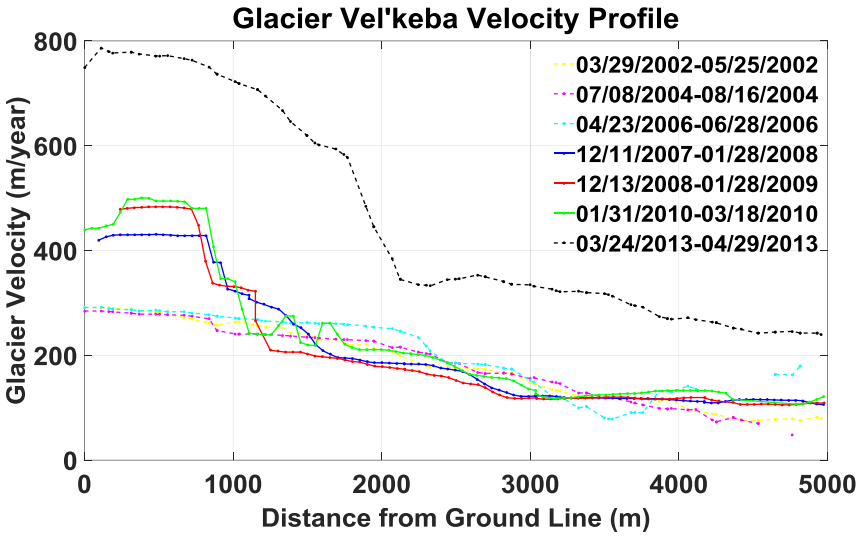

Figure 4-13 Velocity variations for Glacier Vel'keba from 2002 to 2013.

(typically 3 for most glaciers). A previous study demonstrated that the minimum octahedral shear strain rate shows a positive correlation with temperature (*Budd and Jacka*, 1989). When the stress does not change, the velocity and the temperature should have a linear relationship. Figure 4-14 shows all of the estimated velocities and monthly air temperatures. The area from 2.5 km to 3.5 km from the frontal position was chosen as the reference area to avoid the influence of calving flux on velocity variation, and the mean value was used as the reference. It is evident that, besides the observation in 2013, the velocity and temperature values have a linear relationship. This indicates that from 2002 to 2010, the stress contribution to the velocity profile for Glacier Vel'keba was relatively constant, and air temperature drove the velocity changes during this period.

However, air temperature change is not sufficient to explain the large increase between 2010 and 2013 because we observed no dramatic change in the air temperature (Figure 4-12). Since Glacier Vel'keba is a marine-terminating glacier, the nearby SST could have an impact on velocity change, especially on the seasonal retreat of the frontal position (*Howat et al.*, 2010). Therefore, SST near the Barents Sea was examined from

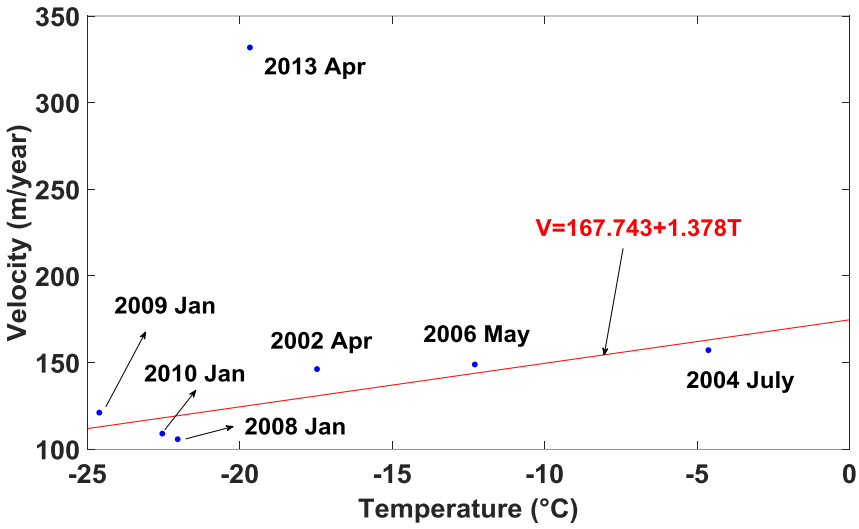

Figure 4-14 Correlation between velocity and air temperature at Glacier Vel'keba.

ERA-Interim reanalysis data (Figure 4-15). The result shows that SST in NVZ experienced a rise from 2002–2014 in general. The summer SST has an increase of about 3–5 °C while the winter SST stays steady. This period can be divided into two phases due to the change in summer SST variation. From 2002 to 2010, the summer SST has a slight increase of less than 2 °C. After 2010, a significant increase of about 3 °C occurred. The velocity increase from 2010 to 2013 is consistent with the increase of SST from 2010. Since oceanic warming could also cause retreat via waterline melting and undercutting of the terminus, the SST increase would accelerate fontal retreat. In addition, this may cause physical changes along the glacier stream, which corresponds to a change of stress contribution in Figure 4-14 (*Benn et al.*, 2007; *Carr et al.*, 2014; *Vieli et al.*, 2002).

To explain the sudden increase in SST, the Arctic Oscillation (AO) index in 2002–2014 (Figure 4-16) was checked from the Climate Change Center (CPC) database (http://www.cpc.ncep.noaa.gov/products/precip/CWlink/daily_ao_index/ao.shtml). The blue bars represent the AO index and the red line represents the winter AO variation trend.

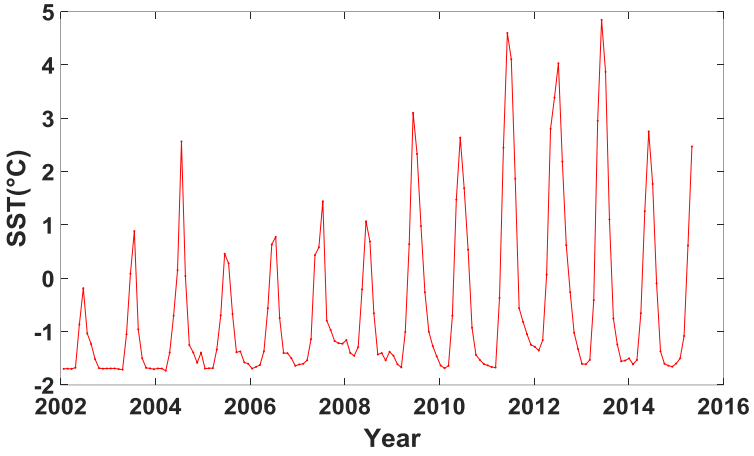

Figure 4-15 ERA-Interim monthly SST in 2002–2014.

A significant increase in SST was noticed in 2010, which is attributed to the AO negative phase in 2010.This agrees with the conclusion that the negative AO would increase the Atlantic waters penetration and bring warmer Atlantic water into the Barents Sea, which would cause such an increase of SST (*Ingvaldsen et al.*, 2004; *Oziel and Sirven*, 2011). In summary, both SST and air temperature have influenced the velocity of the Glacier Vel'keba. It is expected that SST and air temperature had a similar impact on the other three adjacent marine-terminating glaciers which showed similar elevation trends from 2002–2010 (see Figure 4-5) and experienced similar velocity increases of 50 m year^{-1} in 2007–2010 (see Figure 4-7).

Given that we obtained a linear correlation between velocity and air temperature, we could adjust the observation months of all pairs to be April to coincide with the 2013 PALSAR pair. Consequently, stream velocities were compared without the influence of seasonal variation in temperatures. Figure 4-17 shows that the velocity profile in 2004 is relatively slower than in 2002 and 2006. On the other hand, in 2008, the frontal velocity exhibited an increase compared to 2006. Similar trends were then observed in 2008–2010.

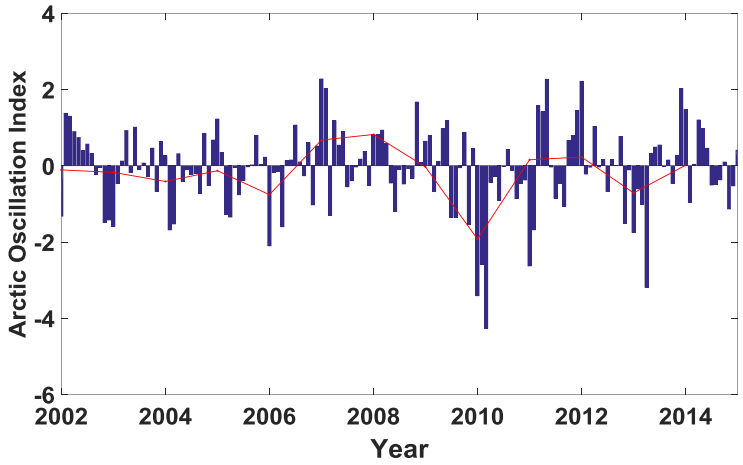

Figure 4-16 Time series of AO Index in 2002–2014.

In summary, two significant velocity increases were discovered in the period from 2002–2013 in Figure 4-17. The first was in 2004–2008, while the second was 2010–2013. It is also noticed that most of the acceleration occurred in the frontal position. Based on the correlation between frontal acceleration and calving flux increase, the calving flux increase in 2000–2010 proposed by *Carr et al.* (2014) and *Melkonian et al.* (2016) appear to be confirmed

4.3.5 Contribution of Outflow on NVZ Marine-terminating Glacier Retreat

To assess the contribution of outflow for mass balance, the mass influx, i.e., snowfall, is also required. Snow depth anomalies from ERA-Interim was used to represent snowfall variations (Figure 4-18). The blue bars represent monthly snow depth anomalies during the winter (November to March), and the red line represents mean snow depth anomalies during the winter. The snow depth anomalies were obtained by subtracting the average monthly value from each month. This average was calculated using the monthly values for the period from 1979–2014. For example, to generate the monthly anomalies for

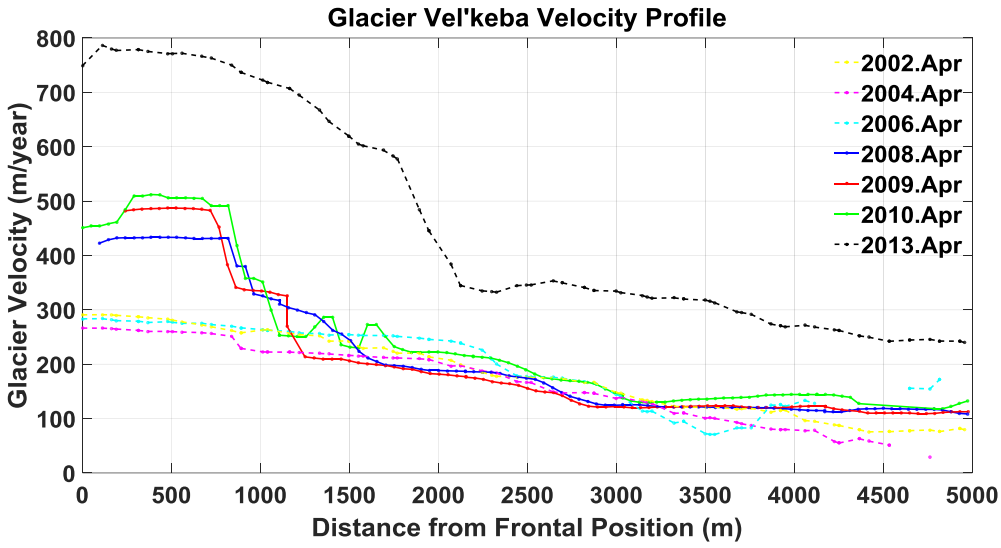

Figure 4-17 Velocity profiles for the period of 2002–2013 over Glacier Vel'keba after unifying the observation months to April.

2002 January, the average monthly value was calculated using the January values for 1979–2014. Then, the difference between the averaged January value and 2002 January value was calculated to be the anomaly. From Figure 4-18, it is evident that there is a period of positive anomalies from 2003 to 2013. During these years, it is expected that a larger amount of snowfall occurred.

From previous sections, multiple observations are available over the 4 glaciers in northern NVZ using different geodetic techniques and the ERA-interim climate model including the glacier velocity variations, elevation changes, mass changes and snowfall anomalies. These changes from 2002 to 2014 could be classified into three categories of influx, outflow, and net change as in Table 4-3. "+" indicates an increasing trend, "–" indicates a decreasing trend, "0" indicates no significant change. "*" indicates not available in selected period. The velocity variation represents the variation of glacier outflow. The snowfall anomalies represent the anomalies for glacier influx. The elevation and mass changes represent the net loss or gain of ice mass. Since the net loss or gain should be equal

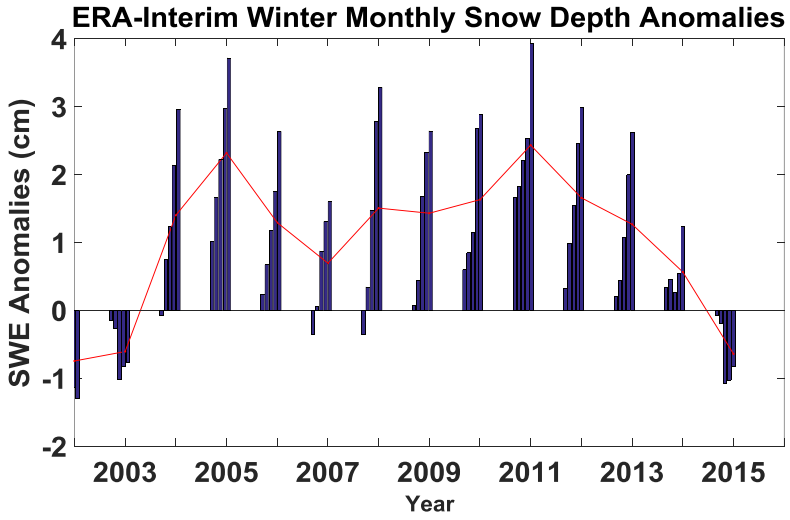

Figure 4-18 ERA-Interim monthly snow depth anomalies (mean removed) for 2002–2014.

to the difference between influx and outflow, the relationship can be examined between these three factors. The positive mass trend observed from GRACE and altimetry data for the period from 2007–2010 can be explained by the increase in snowfall while the change in outflow was negligible. However, for periods from 2004–2007 and 2010–2013, while both the influx and outflow changes were positive, a negative net change was observed. This indicates that during these two periods, outflow variation played a more significant role in the net mass change than influx, which resulted in a mass loss. In addition, accelerated flow velocity was observed mostly at the frontal position as can be seen from Figure 4-17 especially in the period 2004–2007, which would be mostly due to a significant calving flux increase (*Howat et al.*, 2005; *Melkonian et al.*, 2016). Therefore, considering the influence of snowfall, the conclusion of previous studies by Carr et al. (2014) and Melkonian et al. (2016) was confirmed that calving flux made a significant contribution to glacier retreat for NVZ Barents Sea coast marine-terminating glaciers.

Table 4-3 The glacier states relationship in NVZ from 2002 to 2014.

	2002–2004	2004–2007	2007–2010	2010–2013	2013–2014
Influx	–	+	+	+	–
Outflow	0	+	0	+	*
Net change	–	–	+	–	–

4.4 Conclusions

In this case study, the state change of marine-terminating glaciers over NVZ Barents Sea coast was explored. The velocity variation, elevation, and mass change rates from 2002 to 2014 were obtained using different spaceborne geodetic techniques. Over the entire NVZ, the average mass change rate of –1.04 ± 0.25 Gt/year was obtained for 2003–2014 from GRACE data. Interannual variations of mass change at –5.94 ± 0.97 Gt/year and –7.06 ± 1.04 Gt/year were observed in the periods from 2003–2007 and 2010–2014, respectively. In addition, interannual variations in the form of positive mass change of 4.26 ± 0.96 Gt/year was estimated for 2007–2010. The temporal variations in mass change trends in 2003–2010 were confirmed with the altimetry-derived elevation change rates. Two steam velocity increasing periods from 2004–2007 and 2010–2013 were also reported. The slight increase of 50 m $year^{-1}$ in 2004–2007 was driven by air temperature increase, and the relatively larger increase of 100 m $year^{-1}$ in 2010–2013 was likely caused by the rise of SST in the Barents Sea. These velocity estimates indicate that both air temperature and SST influence the glacier velocity of NVZ marine-terminating glaciers along the Barents Sea coast. Since most of the velocity acceleration from 300 m $year^{-1}$ to 800 m $year^{-1}$ from 2002 to 2013 occurred in the frontal position, it was identified that the calving flux has increased during the same period (*Carr et al.*, 2014; *Melkonian et al.*, 2016). The variation in mass influx was investigated using snow depth anomalies obtained from ERA-Interim. Two periods of negative anomalies were observed for 2002–2004 and 2013–2014.

With these mass influx and outflow variations, and net mass changes over our study area, we have a better understanding of the states of the marine-terminating glaciers. The increase in 2007–2010 can be explained by the positive snowfall anomalies and negligible outflow. However, in the periods from 2004–2007 and 2010–2013, both the mass influx and outflow have an increasing trend and a negative net change. Therefore, it can be concluded that the changes in the outflow contributed to the mass net change rather than the changes in influx. Also, since most of the velocity acceleration occurred in the frontal position, we suggest that calving flux had a significant impact on acceleration. Therefore, most of the outflow influence on net change can be attributed to the calving flux. Consequently, the conclusion is confirmed that calving flux for the NVZ Barents Sea coast has made the major contribution to local ice loss is confirmed (*Carr et al.*, 2014; *Melkonian et al.*, 2016).

5 Mass Balance Estimates Using Thickness Change: Case Study in Nyainqen Tanglha, Himalaya

5.1 Background & Data

The melting of glaciers and ice caps makes a significant contribution to present-day sea level rise (*Zemp et al*., 2019; *Cogley*, 2009). As the largest glacierized region outside of the Arctic and Antarctica, the glaciers in HMA are the 5th largest contribution to global glacier melting (*Zemp et al*., 2019; *Gardner et al*., 2013; *Jacob et al*., 2012). In spite of spatially heterogeneous glacier changes, estimates of mass loss have relied on the interpolation of sparse glaciological and local geodetic data at annual resolution (*Dyurgerov and Meier*, 2005; *Mark F. Meier et al.*, 2007; *Ohmura*, 2006). Only recently, several studies have reported a negative mass budget during the last decade in HMA using different spaceborne geodetic techniques. *Matsuo et al.* (2010) and *Jacob et al.* (2012) used measurements from GRACE over the entire HMA region, and yet reported different mass balance estimates of –47 ± 12 Gt/year and –4 ± 20 Gt/year, respectively from 2003 to 2009. *Jacob et al.* (2012) claimed that this significant difference was due to uncorrected substantial groundwater estimation over the Indian plains in *Matsuo et al.* (2010)'s mass change estimation. On the other hand, *Kääb et al.* (2012) used ICESat data to generate elevation changes over the Hindu Kush-Karakoram-Himalaya (HKKH) region for the period from 2003 – 2009 and obtained a mass balance of –12.8 ± 3.5 Gt/year. Gardelle et al. (2013) used both GRACE and ICESat data and obtained the mass balance over the entire HMA for the period from 2003 – 2009. However, the GRACE results obtained by *Gardelle*

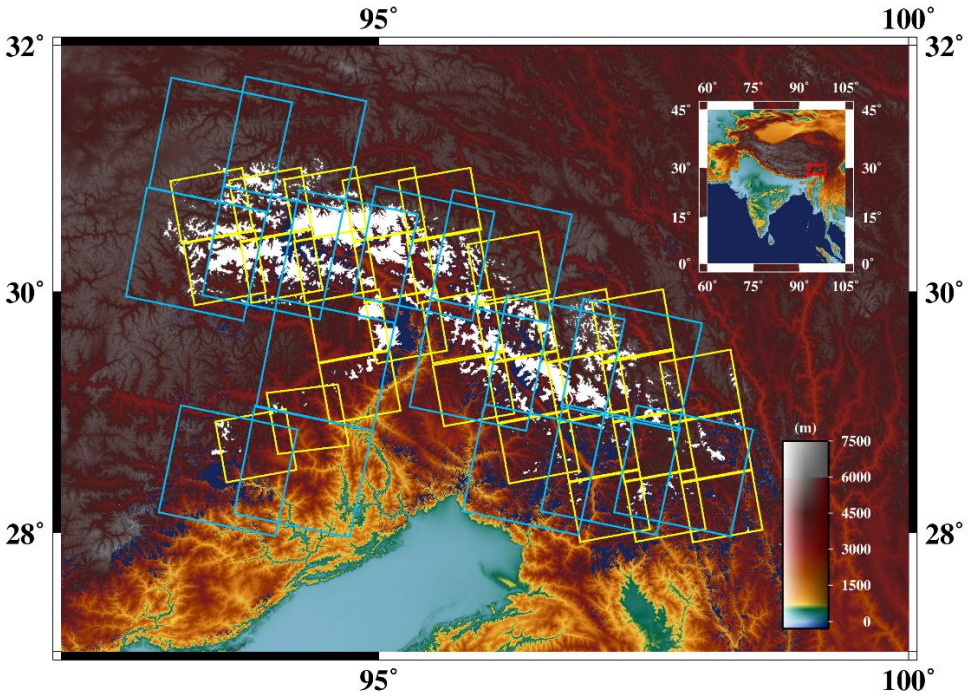

Figure 5-1 Map of Nyainqen Tanglha region with Envisat ASAR (blue outlines) and ALOS PALSAR (yellow outlines) image coverages. White regions represent glacier coverage. The background is topography from SRTM DEM.

et al. (2013) (–14 ± 17 Gt/year) differs from that of *Jacob et al.* (2012) (−4 ± 20 Gt/year) despite using the same data and methods. Perhaps, the disparity in their results is due to the different version of the Global Land Data Assimilation System (GLDAS) hydrologic models they used. *Gardelle et al.* (2013) obtained ice thickness and volume changes over multiple glaciers in HKKH from 1999 to 2011 based on Digital Elevation Model (DEM) differencing. Their estimates over the Karakoram agreed with *Kääb et al.* (2012) within the error bar. In *Kääb et al.* (2015), the study area was expanded to the Pamir and Hengduan Shan and a larger negative mass budget of –24 ± 2 Gt/year was obtained. *Kääb et al.* (2015) compared their result using ICESat data (−19 ± 3 Gt/year) with that of *Jacob et al.* (2012) using GRACE data (−3 ± 12 Gt/year) and claimed the disagreement of 16 Gt/year over the Nyainqen Tanglha region. Given the approaches are fundamentally different, *Kääb et al.*

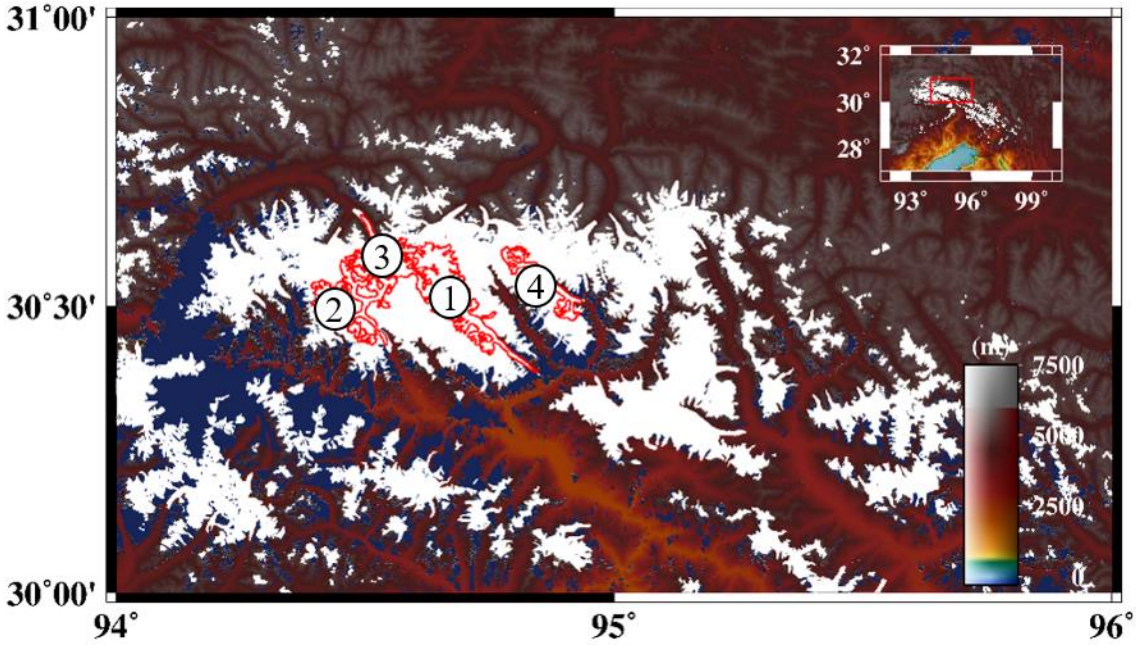

Figure 5-2 Location of 4 selected glaciers (red outlines) in the Nyainqen Tanglha region.

(2015) did not discuss the potential sources of this disagreement.

5.2 Study Area and Data

Nyainqen Tanglha is chosen as the study region considering the large discrepancy of ice loss between GRACE and ICESat derived estimates (*Kääb et al.*, 2015). Figure 5-1 presents the location of Nyainqen Tanglha. Four of the largest glaciers were selected in this region as the test cases shown in Figure 5-2. White regions represent glacier coverage, the background is topography from SRTM DEM, and black numbers over the selected glaciers in Figure 5-2 are the inventory numbers in this study. To implement the method proposed in section 3, surface velocity and surface slope are required to calculate the ice thickness. The available SAR images pairs over the selected glaciers has the largest quantity for Nyainqen Tanglha. With sufficient availability of ALOS/ALOS-2 PALSAR image pairs, surface velocity was estimated by applying speckle matching in the period of 2008–2016.

Table 5-1 List of available ALOS/ALOS-2 PALSAR images over study area.

Observation Approaches	Scene No.	Observation Date
ALOS	ALPSRP076670600	2007/07/03
ALOS	ALPSRP083380600	2007/08/18
ALOS	ALPSRP090090600	2007/10/03
ALOS	ALPSRP103510600	2008/01/03
ALOS	ALPSRP110220600	2008/02/18
ALOS	ALPSRP116930600	2008/04/04
ALOS	ALPSRP123640600	2008/05/20
ALOS	ALPSRP130350600	2008/07/05
ALOS	ALPSRP137060600	2008/08/20
ALOS	ALPSRP157190600	2009/01/05
ALOS	ALPSRP163900600	2009/02/20
ALOS	ALPSRP184030600	2009/07/08
ALOS	ALPSRP197450600	2009/10/08
ALOS	ALPSRP210870600	2010/01/08
ALOS	ALPSRP217580600	2010/02/23
ALOS	ALPSRP237710600	2010/07/11
ALOS	ALPSRP244420600	2010/08/26
ALOS	ALPSRP251130600	2010/10/11
ALOS	ALPSRP264550600	2011/01/11
ALOS-2	ALOS2017390600-140918	2014/09/18
ALOS-2	ALOS2027740600-141127	2014/11/27
ALOS-2	ALOS2060860600-150709	2015/07/09
ALOS-2	ALOS2071210600-150917	2015/09/17
ALOS-2	ALOS2081560600-151126	2015/11/26
ALOS-2	ALOS2114680600-160707	2016/07/07
ALOS-2	ALOS2120890600-160818	2016/08/18

Table 5-1 gives the details for images used; a total of 26 images, which are converted into 17 pairs from 2007 summer to 2016 winter. The images pairs from ALOS in the summer season were acquired in Fine Beam Double polarization (FBD) mode. Due to the low resolution and poor quality of images in FBD mode, null pixels exist in the distribution map of the surface velocity for several summer pairs as the upper reach region in Figure 5-3 (a). Besides the null pixels, blunder pixels with extremely large surface velocity are also observed adjacent to the null pixels. To improve the velocity result, a median filter was applied with a window of 5*5 km. The original and filtered surface velocity estimates from September 2017 are presented in Figure 5-3. It is clear that the velocity gap is reasonably

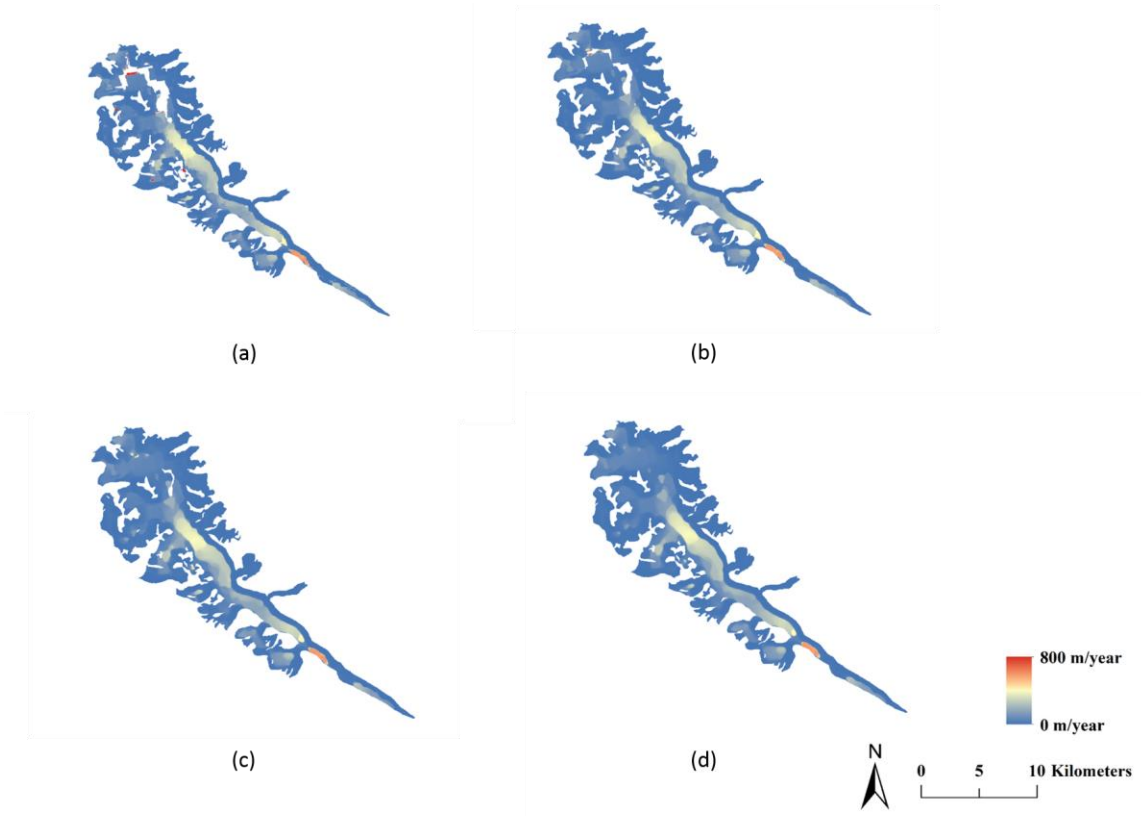

Figure 5-3 (a) Original surface velocity distribution for Glacier No.1 from 2007/08/18 to 2007/10/03; (b)-(d) the corrected surface velocity after applying 1 to 3 median filtering process for the same glacier during the same period.

filled and that the error pixels in the upper reach are filtered. However, the velocity results in several image pairs remain unreasonable after applying the median filter (Figure 5-4). To identify outliers in surface velocity estimates, a stationary method was applied to calculate the velocity errors for each pair of SAR images. A nearby region of rock, consisting of 63,772 pixels was selected as a stable area. Residual movement over the stable areas are considered to be velocity errors. The mean error of the image σ_V was then calculated by averaging the errors for all pixels in the stable area. σ_V of each velocity estimate from 2007 summer to 2016 winter are calculated and summarized in Table 5-2. The Interquartile Range (IQR) of σ_V was used to identify outliers as shown in Figure 5-4.

Table 5-2 Mean velocity estimated errors. The red color represents periods identified as outliers.

Observation Period	Velocity Error (Unit:m/year)	Observation Period	Velocity Error (Unit:m/year)
2007-07	1.35	2010-01	6.41
2007-09	3.04	2010-07	1.84
2008-01	5.07	2010-09	2.44
2008-03	2.46	2010-11	9.43
2008-04	2.79	2014-10	1.67
2008-06	13.57	2015-08	1.67
2008-07	14.21	2015-10	6.25
2009-01	2.35	2016-07	10.21
2009-09	4.96		

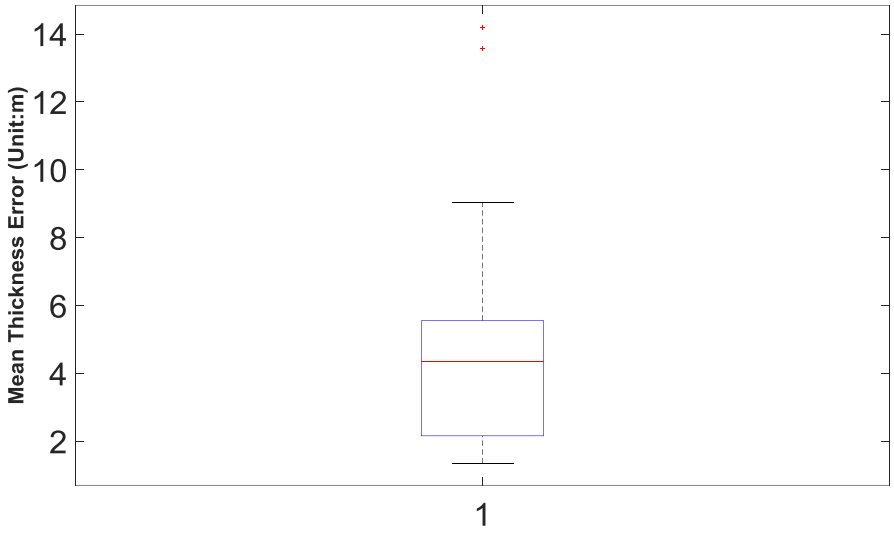

Figure 5-4 IQR plot of the surface velocity errors in the stable region for all 18 pairs of ALOS/ALOS-2 SAR images from 2008 to 2016.

The two red points at the top represent two major outliers observed in June, 2008 and July 2008. Moreover, the observations from September, 2010 and July, 2016 were also identified as outliers

Advanced Spaceborne Thermal Emission and Reflection Radiometer (ASTER) GDEM v2 with 30-meter resolution was used to generate surface slope following the contour method introduced in chapter 3. A Gaussian filter with a 3×3 window was applied to smooth the slope distribution map (Figure 5-5). Since the 4 selected test glaciers are all

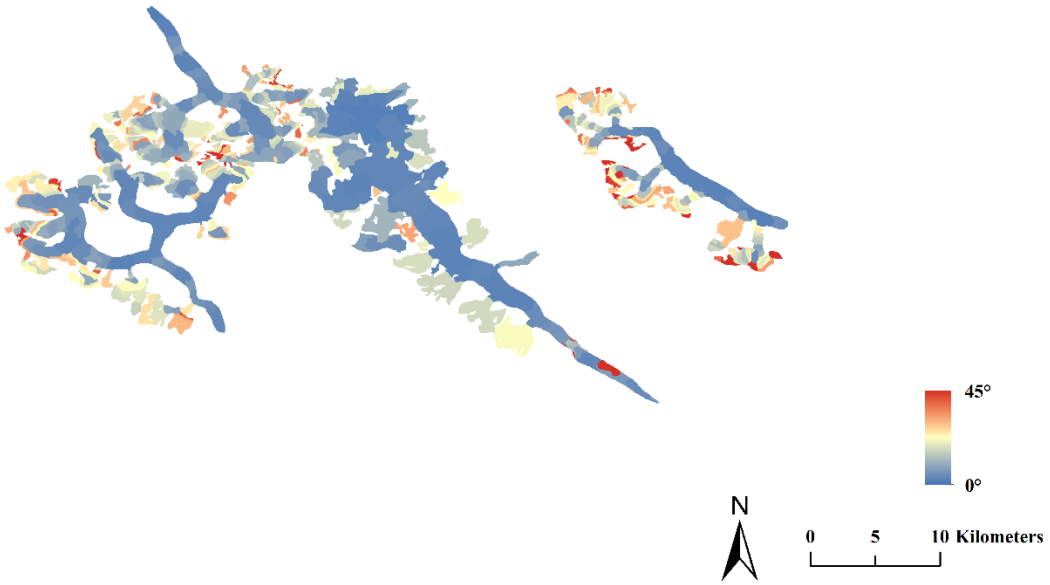

Figure 5-5 Slope distribution map for the 4 test glaciers in Eastern Nyainqen Tanglha based on ASTER GDEM V2 data.

temperate glaciers, the surface air temperature is not required in this study.

5.3 Results & Discussions

By using the methods introduced in chapter 3, 13 ice thickness observations were obtained for the period from 2008 – 2016 over the 4 test glaciers. The thickness distribution maps over Glacier No.1 are shown in Figure 5-6 as an example to illustrate the variation in thickness. A series of similar distribution maps were generated covering all seasons. The most rapidly-changing area is determined to be the thick region at the lower reach, where the thickness distributions in summer and winter are different. The thickness distribution map covering all 4 test cases during July 2017 is illustrated in Figure 5-7. The thickness estimates are observed to be larger along the main trunks of glaciers in all test cases. The thickness estimates for Glacier No.1 are observed to be much larger than the other 3 glaciers. The peak value for Glacier No.1 is close to 400 m, while it is 200 m in the others.

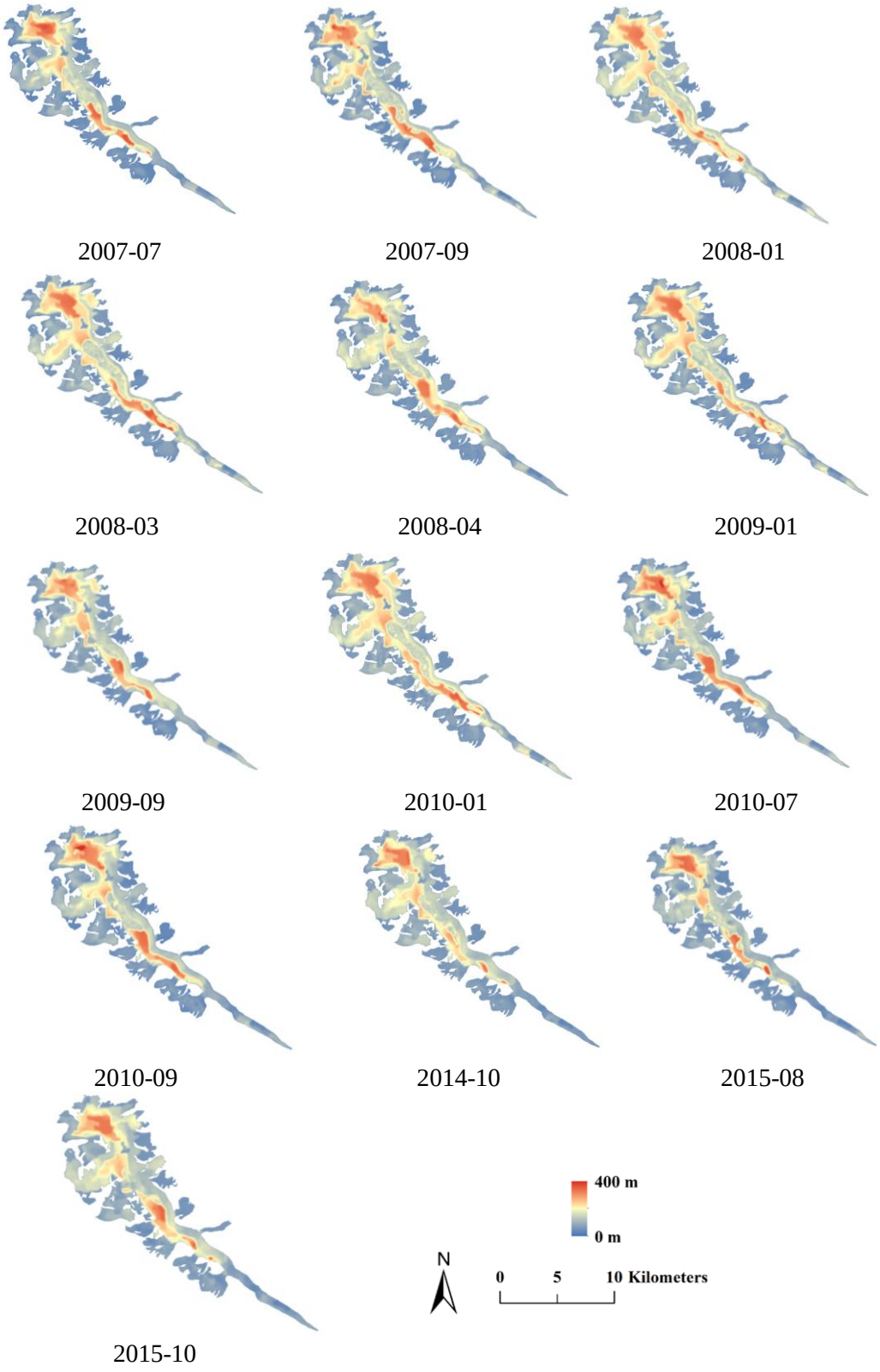

Figure 5-6 Distribution maps of thickness in Glacier No.1 from 2008 to 2016.

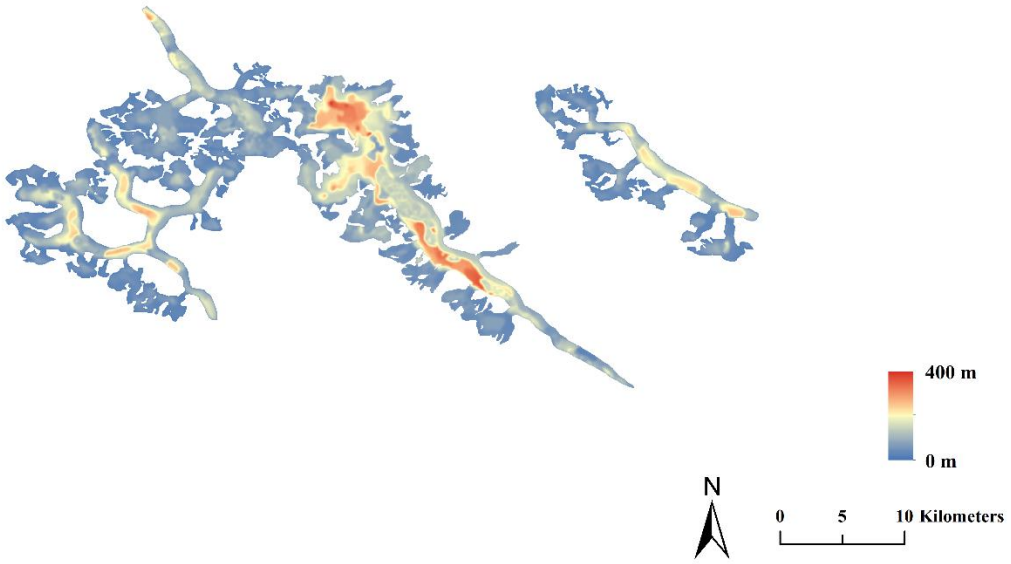

Figure 5-7 Thickness distribution map of the four selected glaciers during 2007/07

Additionally, the thickness estimates for all pixels were averaged in each test case and generated the mean thickness variation trend of each glacier was generated in Figure 5-8. Decreasing trends were observed as –0.47 ± 0.61 m/year, –0.57 ± 0.46 m/year, –0.69 ± 0.32 m/year and –1.17 ± 0.64 m/year for the period from 2008–2016 for Glacier No.1 to Glacier No.4, respectively. Due to the lack of observations, seasonal variations of thickness are not fully discussed in this study. However, a large inter-annual difference was observed in thickness estimates of up to 10 meters. This large inter-annual variability of the surface elevation was also found in the previous study (*Brun et al.*, 2017).

5.3.1 Comparison of Thickness Change Estimates with DEM Difference Approach

From previous studies, it is well established that Nyainqen Tanglha experienced one of the largest ice losses. This ice loss corresponds to an elevation decrease rate of 1.34 ± 0.29 m/year for the period from 2003–2009, based on ICESat observations that show a greater decrease than our estimates ranging from –0.47 m/year to –1.17 m/year for the

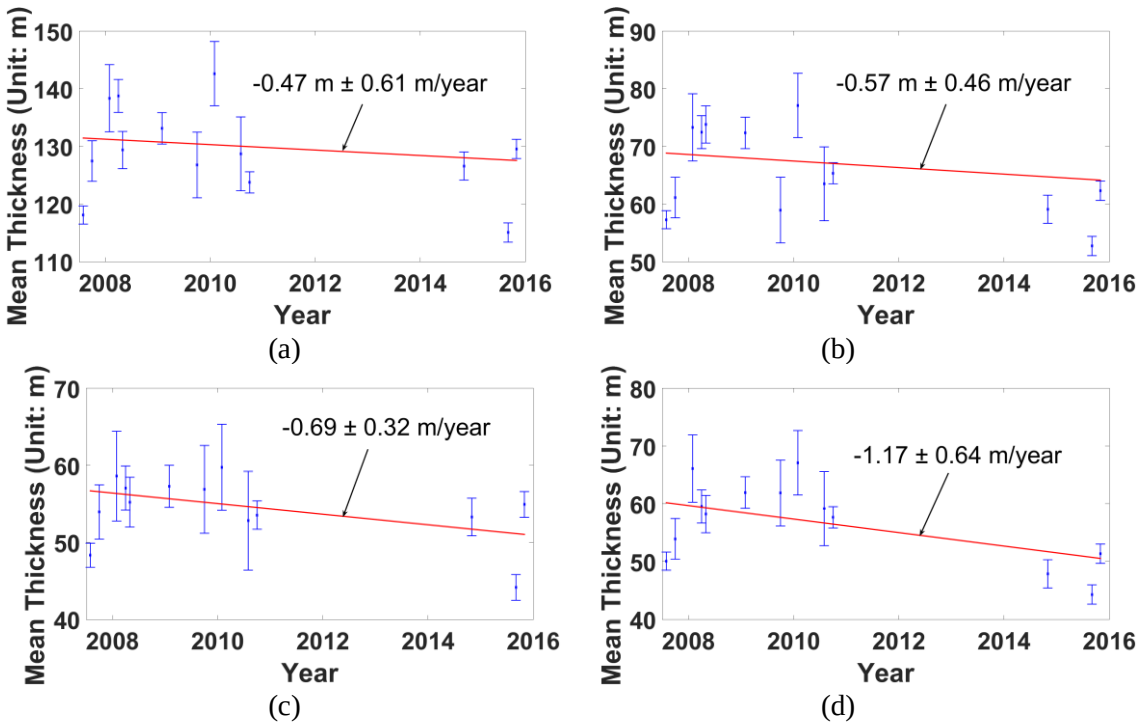

Figure 5-8 Variation of mean thickness estimates for the 4 test glaciers from 2008 – 2016. The blue error bars represent the estimates errors introduced by surface velocity errors. (a) to (d) are Glacier No.1 to No.4, respectively.

period from 2008–2016. However, since the observation period of this study (2008–2016) does not overlap enough with the ICESat mission period (2003–2009), these two estimates cannot be directly compared. Therefore, the estimates from the proposed method was compared with a previous result from a DEM differencing approach. *Brun et al.* (2017) applied a fully automated differencing method to L1A ASTER optical images and calculated the thickness distribution map for all glaciers which are larger than 2 km^2 in HMA from 2000 to 2016. A decreasing trend of mean ice thickness with a rate of –0.72 ± 0.27 m/year was observed over Nyainqen Tanglha for the period from 2000 to 2016. Similarly, *Brun et al.* (2017) validated the estimates and found disagreement with ICESat estimates. This discrepancy was mostly explained by the high inter-annual variability of surface elevation in Nyainqen Tanglha. This means that removing one-year of observations from the trend fit can significantly change the result. Therefore, ICESat derived estimates

Table 5-3 Variation of ice thickness using proposed method and the ASTER DEM differencing approach

Data Source and Observation Period	Glacier No.1 (Unit: m/year)	Glacier No.2 (Unit: m/year)	Glacier No.3 (Unit: m/year)	Glacier No.4 (Unit: m/year)
ASTER DEM Differencing (2000–2016)	-0.74 ± 0.23	-0.94 ± 0.23	-0.74 ± 0.23	-1.08 ± 0.23
This study (2008–2016)	-0.47 ± 0.61	-0.57 ± 0.46	-0.69 ± 0.32	-1.17 ± 0.64

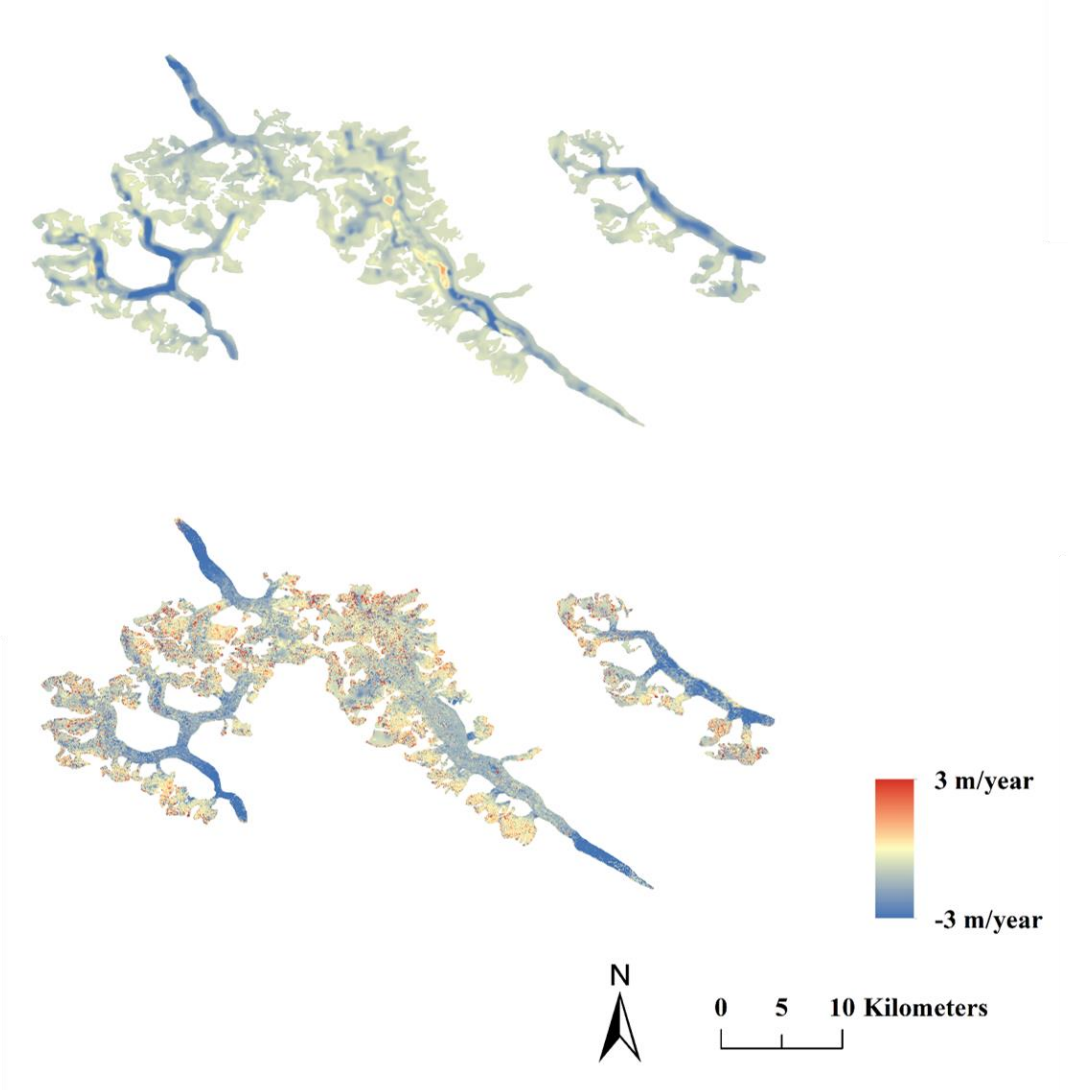

Figure 5-9 Comparison of thickness difference estimate between our estimates in the period from 2008 to 2016 (top) and the ASTER DEM difference estimates in the period from 2000 to 2016 (bot).

can be more biased since the repeat cycle is 91 days.

The distribution maps of thickness changes from the proposed method and the

DEM differencing method are displayed in Figure 5-9. Although the observation periods of these two approaches are not identical, similar distributions were observed. Additionally, the mean thickness change rate for each test glacier using these two approaches were calculated and compared in Table 5-3. Notably, only the total difference of thickness estimates was provided by *Brun et al.* (2017) for the period from 2000 to 2016. Without estimates during this period, it is impossible to calculate the standard error. Therefore, the error of the entire Nyainqen Tanglha (0.23 m/year) provided in *Brun et al.* (2017) was used as the error for each glacier. An agreement within the range of uncertainty was found for all 4 test glaciers. This indicates that there is no significant change in the mass loss rate between the periods from 2000–2006 and 2008–2016. Still, we found a few disagreement pixels in the middle part of Glacier No.1. This may be due to the fact that the observation periods for these two approaches are different. Another potential explanation is due to the assumptions we made about the bedrock slope. The surface and bedrock slopes can be different for steep regions, but were assumed identical in the method. This inconsistency may lead to an overestimated error as we have in the Unteraar case estimates presented chapter 3.

5.3.2 Comparison of Mass Balance Estimates with GRACE Data

A consistent mass loss rate was identified between 2000–2016 and 2008–20016 based on the comparison of thickness changes with the DEM approach in the previous section. To validate this finding, we examined GRACE observations around our study region (Fig 5-10). The selected glaciers are included in two GRACE pixels. The average estimates for the two pixels are used to represent the mass balance around our study region.

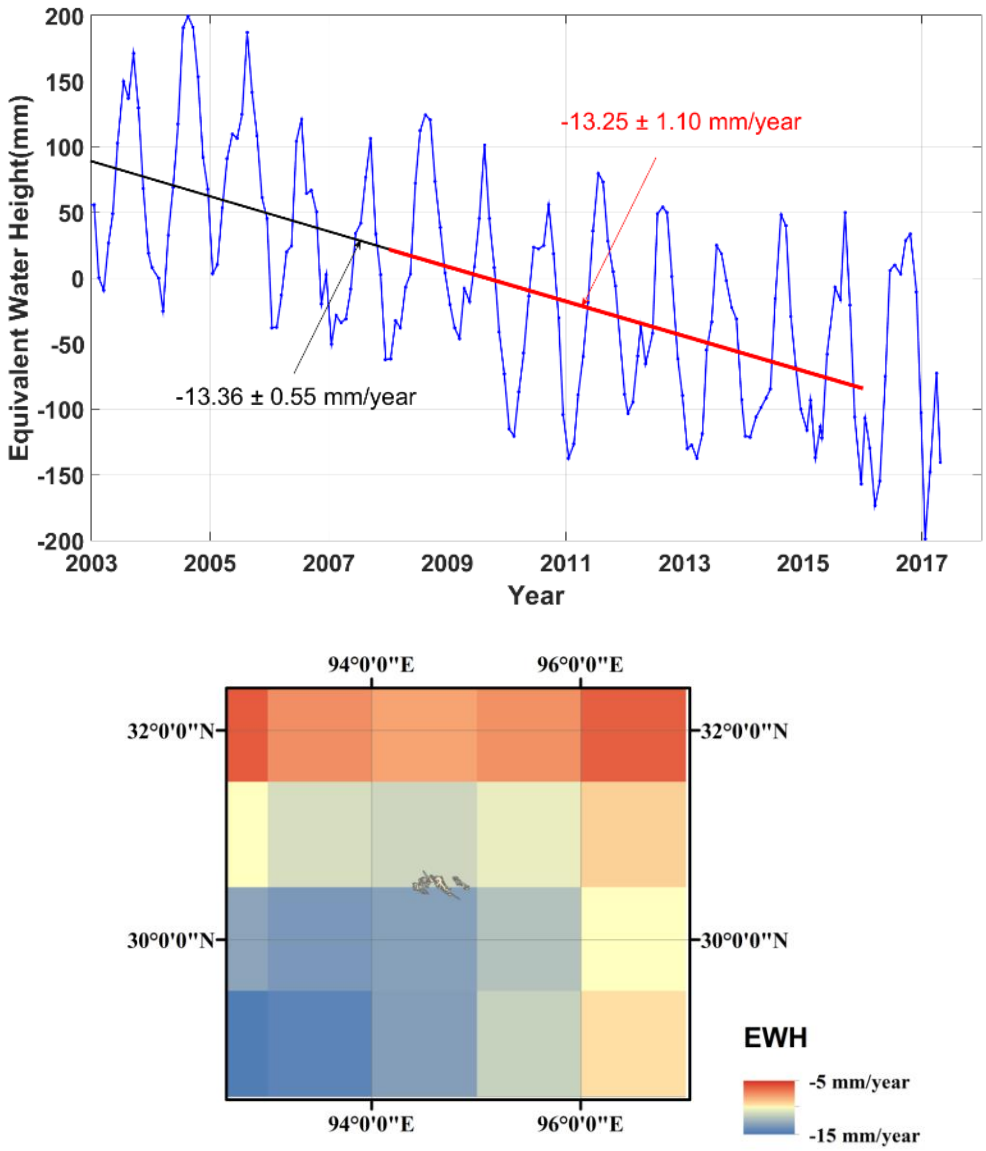

Figure 5-10 The variation of surface mass balance around 4 selected glaciers using GRACE from 2003 to 2016 (black line) and from 2008 to 2016 (red line) (top). The distribution map of surface mass change around 4 selected glaciers (bot).

The ice loss trend in 2000–2016 and 2008–2016 are obtained as –13.36 ± 0.55 mm/year and –13.25 ± 1.10 mm/year in EWH, respectively. The identical estimates from GRACE confirm the conclusion that the mass loss rate for 2008–2016 is consisted with that for 2000–2016. Furthermore, we computed the surface mass loss over the 4 selected glaciers as -0.19 ± 0.09 Gt/year based on estimated thickness and the glacier area from the Randolph

Glacier Inventory (RGI) 6.0 database. If the rest of the glacierized areas (60%) within the two surrounding GRACE pixels are assumed to have a similar mass balance as the average of the selected glaciers, the total mass balance result for the glaciers within the two GRACE pixels is –0.47 ± 0.21 Gt/year from 2008 to 2016, while this number in GRACE is –0.28 ± 0.02 Gt/year. It is evident that even though the coarse mass loss estimate is only calculated based on observation from 40% of the glacierized area, the mass balance based on thickness estimates still agrees with GRACE-derived estimates within the range of uncertainty. Based on the thickness change, it is clear that the estimates in this study agree better with GRACE estimates rather than ICESat estimates. The agreement of mass balance and ice thickness with previous techniques show that our method is promising to be implemented in the Himalaya region to obtain accurate ice thickness distribution maps and mass balance estimates.

5.4 Conclusion

In this section, the proposed thickness estimate method was successfully implemented for 4 selected test glaciers in the Eastern Nyainqen Tanglha region from 2008 to 2016. Surface velocity was obtained using 17 pairs of ALOS/ALOS-2 PALSAR images from 2007 summer to 2016 summer via speckle matching. 13 of 17 velocity observations were finally used in this study while the other 4 estimates were filtered as outliers based on IQR analysis of errors. A surface slope distribution map was generated by applying the contour method, provided in chapter 3 to ASTER DEM data. The thickness distribution map during the observation period was obtained with observed decreasing trends in thickness of –0.47 ± 0.61 m/year, –0.57 ± 0.46 m/year, –0.69 ± 0.32 m/year and –1.17 ±

0.64 m/year for Glaciers No.1 to No.4, respectively. A distribution map of thickness changes was directly compared with the estimates from the ASTER DEM differencing approaches. The similar distribution of thickness changes and the consistent mean thickness change rates indicate that mass loss rate remains the same between 2008 – 2016 and 2000 – 2016. GRACE observations for these two periods confirm this conclusion. The mass balance estimates over the 4 selected glaciers were calculated from 2008 to 2016 as –0.19 ± 0.09 Gt/year. To validate our estimates with GRACE observations, an extrapolation of the mass balance was applied to the entire glacierized area. The mass balance was estimated as –0.47 ± 0.21 Gt/year by assuming the mass loss rate is identical to that for the 4 selected glaciers. By contrast, the mass balance from GRACE is –0.28 ± 0.02 Gt/year which agrees with our estimates within errors. Overall, our method is shown to be a reliable approach to obtain the ice thickness distribution map. The accurate thickness and mass balance estimates should be implemented in other undermined or controversial glacierized region in the Himalayas.

6. Conclusion & Future Work.

6.1 Contribution of Dissertation and Conclusion

Sea level rise due to glacier melt has been a critical global issue during the past two decades. To identify this contribution, it is critical to have a comprehensive understanding and accurate estimate of glacier ice thickness and mass balance. However, the lack of in-situ data limits the study of glacier mass balance for a number of remote glaciers. Spaceborne techniques such as GRACE and ICESat expand the observations over regions where traditional in-situ measurements are not available. These new techniques are still limited by estimation accuracy, spatial resolution, and temporal coverage. Moreover, the observations from different sensors may have large discrepancies over a certain area, like the Himalaya region. To clarify such discrepancies and obtain accurate mass balance estimates, in this dissertation, a new iterative method to estimate ice thickness and calculate the mass balance in glaciers was developed.

In chapter 3, a new iterative method of estimating ice thickness was presented using surface velocity, surface topography, and a pre-defined englacial temperature. Local surface velocity and surface topography measurements were provided from previous studies. Additionally, extra surface velocity estimates were obtained using ALOS PALSAR image pairs via a speckle-matching technique. For temperate glaciers, an empirical englacial temperature was determined as 273.0 K, which corresponds to a rate factor of 11.38×10^{-24} $Pa^{-3}s^{-1}$. For non-temperate glaciers, the assumption of the previous study was followed. A temperature offset of 7 °C was applied between the englacial temperature and the surface air temperature. The proposed method was validated over 8

along-flow and 12 cross-sectional profiles of 6 temperate glaciers, 1 non-temperate glacier, and 1 non-temperate ice cap. The proposed method provided thickness estimates with a better agreement with in-situ measurement compared with most of the previous methods. The mean error and mean relative error was improved from –39.26 m, –26.84 % to 20.32 m, 8.55 % compared with a previous velocity-based method. Based on sensitivity analysis, the error decreases significantly with an increase of surface slope. Therefore, the proposed method is expected to have a better performance in steep regions, such as the Himalayas.

In chapter 4, multiple geodetic observations from 4 selected glaciers were presented for the Novaya Zemlya along the Barents Sea coast to determine the influence of glacier outflow on net mass change by considering mass gain from snowfall. Traditional techniques of observing surface mass balance such as GRACE and radar altimeter have been used in Novaya Zemlya. An average ice loss rate of -1.04 ± 0.25 Gt/year was obtained between 2003 and 2014 from GRACE data. An interannual increase of mass was also observed at the rate of 4.30 ± 0.97 Gt/year for 2007–2010. Two other interannual variations of negative mass changes were found from GRACE data during the periods from 2004–2007 and 2010–2014. Speckle matching and feature tracking techniques were applied on several pairs of SAR and Landsat images to obtain glacier velocities. With the velocity representing the outflow and the snowfall from ERA-interim data representing the influx, the mass increase from 2007–2010 was due to the increase in influx while the change in outflow was negligible. In addition, a similar analysis was applied to the periods from 2002–2007 and 2010–2014, and the contribution of outflow and influx to the mass change were identified for Novaya Zemlya.

In chapter 5, the proposed method in chapter 3 was applied to 4 selected glaciers in

the Nyainqen Tanglha where a large discrepancy exists between the estimates of different techniques. ALOS/ALOS-2 PALSAR FBS/FBD images were used to obtain surface velocities from 2008 to 2016 via speckle matching and feature tracking techniques. An ASTER DEM was used to derive the surface slopes. Trends of thickness decrease between –0.47 m/year and –1.17 m/year were observed for the 4 selected glaciers from 2008 to 2016. These estimates were compared with the ones using the ASTER DEM differencing approach with an agreement within the uncertainty level. It indicates that the mass loss rate during 2000 – 2016 and 2008 – 2016 are identical. This conclusion is confirmed by the GRACE observations. Ultimately, the mass balance of the 4 glaciers for the period from 2008 to 2016 is in agreement with the GRACE estimates.

6.2 Future Work

In this dissertation, a new iterative method is proposed which uses surface velocity and surface topography to estimate ice thickness and mass balance for glacierized area. However, various areas are identified where further research is needed: (1) improve the accuracy of the surface slope; (2) determine Glen's flow law factor (A) for non-temperate glaciers; (3) identify ice loss for the rest of the areas in Himalayas.

6.2.1 Improve the Contour Line Method for Calculating Surface Slope

In this dissertation, both 20 m and 100 m contour lines were applied to generate a surface slope distribution map considering the characteristics of the glacier surface features. For clean surfaces, 20 m contours can provide estimates with a better agreement with the in-situ measurements. However, for debris-covered surfaces, 100 m contour lines are recommended to use instead since the debris cover can lead to outliers in slope estimates

when using 20 m contour lines. Therefore, for each glacier, the contour line type used to generate slope was manually determined according to the surface features which is not efficient and accurate. Recently, a new released dataset in RGI 6.0 provides the outlines of the supraglacial debris cover (*Scherler et al.,* 2018). For further study, the decision of surface feature can be automatically made based on this debris cover outlines.

6.2.2 Determine Seasonal Influence on the Thickness Change in Nyainqen Tanglha

In chapter 5, the thickness distribution maps and the trend of thickness change were obtained using the surface velocity estimates from ALOS/ALOS SAR images via speckle matching, and the surface slope estimates from an ASTER DEM from 2008 – 2016. However, due to the lack of surface velocity estimates, a gap of thickness estimates exists from 2011 to 2014. To fill this gap, optical images from Landsat 7/8 will be used to generate additional surface velocity estimates via feature tracking in the future study. The seasonal influence on thickness change of glaciers in the Nyainqen Tanglha can be determined thereafter.

6.2.3 Identify Ice loss in Other Glacierized Area of Himalaya.

The proposed method was successfully implemented for Nyainqen Tanglha. Both the thickness change and mass loss were estimated in this region with better agreement with the GRACE and DEM differencing results than the ICESat estimates. Based on the previous studies, similar discrepancies between the estimates from ICESat, GRACE and other approaches in multiple Himalaya regions, such as Eastern Himalaya and Pamir (*Brun et al.*, 2017; *Gardelle et al.*, 2013; *Jacob et al.*, 2012; *Kääb et al.*, 2015; *Neckel et al.*, 2014). It is promising to apply this method to these other glacierized regions in the Himalayas

where discrepancies of mass balance estimates exist. The agreement of mass balance estimates using the proposed method with GRACE results needs further examinations in other cases.

References

Adhikari, S., Marshall, S.J., 2012. “Parameterization of lateral drag in flowline models of glacier dynamics.” *Journal of Glaciology*. 58, 1119–1132. doi:10.3189/2012JoG12J018

Adhikari, S., Marshall, S.J., 2011. “Improvements to shear-deformational models of glacier dynamics through a longitudinal stress factor.” *Journal of Glaciology*. 57, 1003–1016. doi:10.3189/002214311798843449

Agassiz, L., 1842. “On glaciers, and the evidence of their having once existed in Scotland, Ireland, and England.” *Proceedings of the Geological Society of London*. 327–332.

Ahn, Y., Howat, I.M., 2011. “Efficient automated glacier surface velocity measurement from repeat images using multi-image/multichip and null exclusion feature tracking.” *IEEE Transactions on Geoscience and Remote Sensing*. 49, 2838–2846. doi:10.1109/TGRS.2011.2114891

Anderson, E. A., 1972. “Techniques for predicting snow cover runoff.” *Procceeding of the Banff Symposium*. 840–863.

Anderson, E. A., 1973. “National Weather Service River Forecast System - Snow Accumulation and Ablation Model.” *NOAA Technical Memorandum NWS HYDRO-17*. 1–87.

Armstrong, R.L., Rittger, K., Brodzik, M.J., Racoviteanu, A., Barrett, A.P., Khalsa, S.J.S., Raup, B., Hill, A.F., Khan, A.L., Wilson, A.M., Kayastha, R.B., Fetterer, F., Armstrong, B., 2018. “Runoff from glacier ice and seasonal snow in High Asia: separating melt water sources in river flow.” *Regional Environmental Change*.

doi:10.1007/s10113-018-1429-0

Bahr, D.B., Pfeffer, W.T., Kaser, G., 2015. “A review of volume-area scaling of glaciers.” *Reviews of Geophysics*. 53, 95–140. doi:10.1002/2014RG000470

Baltsavias, E.P., Favey, E., Bauder, A., Bosch, H., Pateraki, M., 2001. “Digital surface modelling by airborne laser scanning and digital photogrammetry for glacier monitoring.” *The Photogrammetric Record*. 17, 243–273. doi:10.1111/0031-868X.00182

Bamber, J.L., 1994. “Ice sheet altimeter processing scheme.” *International Journal of Remote Sensing*. 15, 925–938. doi:10.1080/01431169408954125

Bamber, J.L., Krabill, W., Raper, V., Dowdeswell, J.A., Oerlemans, J., 2005. “Elevation changes measured on Svalbard glaciers and ice maps from airborne laser data.” *Annals of Glaciology*. 42, 202–208. doi:10.3189/172756405781813131

Bamler, R., 2000. “Interferometric stereo radargrammetry: absolute height determination from ERS-ENVISAT interferograms.” *IGARSS 2000. IEEE 2000 International Geoscience and Remote Sensing Symposium*. 2, 742–745. doi:10.1109/igarss.2000.861689

Barry, R.G., 2006. “The status of research on glaciers and global glacier recession: A review.” *Progress in Physical Geography*. 30, 285–306. doi:10.1191/0309133306pp478ra

Beljaars, A., Bechtold, P., Orr, A., Tompkins, A., 2006. “Developments in model physics after ERA-40.” *Proceedings of the ECMWF/GEO Workshop on Atmospheric Reanalysis*. 19–22.

Benn, D.I., Warren, C.R., Mottram, R.H., 2007. “Calving processes and the dynamics of

calving glaciers." *Earth-Science Reviews*. 82, 143–179. doi:10.1016/j.earscirev.2007.02.002

Berthier, E., Raup, B., Scambos, T., 2004. "New velocity map and mass-balance estimate of Mertz Glacier, East Antarctica, derived from Landsat sequential imagery." *Journal of Glaciology*. 49, 503–511. doi:10.3189/172756503781830377

Berthier, E., Vadon, H., Baratoux, D., Arnaud, Y., Vincent, C., Feigl, K.L., Rémy, F., Legrésy, B., 2005. "Surface motion of mountain glaciers derived from satellite optical imagery." *Remote Sensing of Environment*. 95, 14–28. doi:10.1016/j.rse.2004.11.005

Bindschadler, R., Scambos, T., 1991. "Satellite-image-derived velocity field of an Antarctic ice stream." *Science*. 252, 242–246. doi:10.1126/science.252.5003.242

Bindschadler, R., Vornberger, P., Blankenship, D., Scambos, T., Jacobel, R., 1996. "Surface velocity and mass balance of ice streams D and E, West Antarctica." *Journal of Glaciology*. 42, 461–475. doi:10.1017/S0022143000003452

Bolch, T., Kulkarni, A., Kääb, A., Huggel, C., Paul, F., Cogley, J.G., Frey, H., Kargel, J.S., Fujita, K., Scheel, M., 2012. "The state and fate of Himalayan glaciers." *Science*. 336, 310–314. doi:10.1126/science.1215828

Braithwaite, R.J., Olesen, O.B., 1990. "Response of the energy balance on the margin of the Greenland ice sheet to temperature changes." *Journal of Glaciology*. 36, 217–221.

Braithwaite, R.J., Zhang, Y., 1999. "Modelling changes in glacier mass balance that may occur as a result of climate changes." *Geografiska Annaler Series A-Physical Geography*. 81a, 489–496. doi:10.1111/1468-0459.00078

Braun, L.N., Aellen, M., Funk, M., Hock, R., Rohrer, M.B., Steinegger, U., Kappenberger, G., Müller-Lemans, H., 1994. “Measurements and simulation of high alpine water balance components in the Linth-Limmern head watershed (north-eastern Switzerland).” *Zeitschrift für Gletscherkd. und Glazialgeol*. 30, 161–185.

Brinkerhoff, D.J., Aschwanden, A., Truffer, M., 2016. “Bayesian Inference of Subglacial Topography Using Mass Conservation.” *Frontiers in Earth Science*. 4, 1–15. doi:10.3389/feart.2016.00008

Brun, E., Martin, E., Simon, V., Gendre, C., Coleou, C., 1989. “An energy and mass model of snowcover suitable for operational avalanche forecasting.” *Journal of Glaciology*. 35, 333–342. doi:10.1017/S0022143000009254

Brun, F., Berthier, E., Wagnon, P., Kääb, A., Treichler, D., 2017. “A spatially resolved estimate of High Mountain Asia glacier mass balances from 2000 to 2016.” *Nature Geoscience*. 10, 668–673. doi:10.1038/ngeo2999

Budd, W.F., Jacka, T.H., 1989. “A review of ice rheology for ice sheet modelling.” *Cold Regions Science and Technology*. 16, 107–144. doi:10.1016/0165-232X(89)90014-1

Carr, J.R., Stokes, C., Vieli, A., 2014. “Recent retreat of major outlet glaciers on Novaya Zemlya, Russian Arctic, influenced by fjord geometry and sea-ice conditions.” *Journal of Glaciology*. 60, 155–170. doi:10.3189/2014JoG13J122

Carr, J.R., Bell, H., Killick, R., Holt, T., 2017. "Exceptional retreat of Novaya Zemlya's marine-terminating outlet glaciers between 2000 and 2013." *The Cryosphere*. 11.5, 2149-2174.

Chao, B.F., 2005. “On inversion for mass distribution from global (time-variable) gravity field.” *Journal of Geodynamics*. 39, 223–230. doi:10.1016/j.jog.2004.11.001

Chao, B.F., Gross, R.S., 1987. “Changes in the Earth’s rotation and low- degree gravitational field induced by earthquakes.” *Geophysical Journal of the Royal Astronomical Society*. 91, 569–596. doi:10.1111/j.1365-246X.1987.tb01659.x

Chen, J., Ohmura, A., 1990. “Estimation of Alpine glacier water resources and their change since the 1870s.” *IAHS publ*. 193, 127–136.

Cheng, M., Tapley, B.D., Ries, J.C., 2013. “Deceleration in the Earth’s oblateness.” *Journal of Geophysical Research: Solid Earth.* 118, 740–747. doi:10.1002/jgrb.50058

Clarke, G.K.C., Anslow, F.S., Jarosch, A.H., Radić, V., Menounos, B., Bolch, T., Berthier, E., 2013. “Ice volume and subglacial topography for western Canadian glaciers from mass balance fields, thinning rates, and a bed stress model.” *Journal of Climate.* 26, 4282–4303. doi:10.1175/JCLI-D-12-00513.1

Clarke, G.K.C., Berthier, E., Schoof, C.G., Jarosch, A.H., 2009. “Neural networks applied to estimating subglacial topography and glacier volume.” *Journal of Climate*. 22, 2146–2160. doi:10.1175/2008JCLI2572.1

Cogley, G., 2012. “The Future of the World’s Glaciers.” *The Future of the World's Climate*. 197–222. doi:10.1016/B978-0-12-386917-3.00008-7

Cogley, J.G., 2009. “Geodetic and direct mass-balance measurements: comparison and joint analysis.” *Annals of Glaciology*. 50, 96–100. doi:10.3189/172756409787769744

Crawford, N.H., 1973. “Computer simulation techniques for forecasting snowmelt runoff.” *The role of snow and ice in hydrology*. 1062–1072.

Cuffey, K., Paterson, W., 2010. “The physics of glaciers, 4th ed”. *Butterworth-*

Heinemann, Oxford.

Davis, C.H., 2005. "Snowfall-Driven Growth in East Antarctic Ice Sheet Mitigates Recent Sea-Level Rise". *Science*. 308, 1898–1901. doi:10.1126/science.1110662

Davis, C.H., 1996. "A robust threshold retracking algorithm for extracting ice-sheet surface elevations from satellite radar altimeters." *IGARSS'96. 1996 International Geoscience and Remote Sensing Symposium, IEEE*. 3, 1783–1787. doi:10.1109/igarss.1996.516800

Dee, D.P., Uppala, S.M., Healy, S.B., Balmaseda, M.A., de Rosnay, P., Isaksen, L., van de Berg, L., Geer, A.J., McNally, A.P., Matricardi, M., Haimberger, L., Dragani, R., Bormann, N., Hersbach, H., Vitart, F., Kobayashi, S., Andrae, U., Beljaars, A.C.M., Poli, P., Monge-Sanz, B.M., Peubey, C., Thépaut, J. N., Delsol, C., Hólm, E. V., Simmons, A.J., Köhler, M., Bechtold, P., Berrisford, P., Balsamo, G., Park, B.-K., Fuentes, M., Bidlot, J., Bauer, P., Tavolato, C., Kållberg, P., Morcrette, J. J., 2011. "The ERA-Interim reanalysis: configuration and performance of the data assimilation system." *Quarterly Journal of the Royal Meteorological Society*. 137, 553–597. doi:10.1002/qj.828

Dietrich, R., Maas, H.G., Baessler, M., Rülke, A., Richter, A., Schwalbe, E., Westfeld, P., 2007. "Jakobshavn Isbræ, West Greenland: Flow velocities and tidal interaction of the front area from 2004 fleld observations." *Journal of Geophysical Research: Earth Surface.* 112, F03S21. doi:10.1029/2006JF000601

Doty, B.E., Kinter III, J.L., 1995. "Geophysical data analysis and visualization using GrADS. Visualization techniques in space and atmospheric sciences." *National Aeronautics and Space Administration*. Washington, DC (United States).

Dowdeswell, J.A., 1986. “Remote sensing of ice cap outlet glacier fluctuations on Nordaustlandet, Svalbard.” *Polar Research*. 4, 25–32. doi:10.1111/j.1751-8369.1986.tb00515.x

Duan, J., 2014. “Global Ice Mass Balance and its Contribution to Early Twenty-first Century Sea Level Rise.” *The Ohio State University*.

Duan, X.J., Guo, J.Y., Shum, C.K., Van der Wal, W., 2009. “On the postprocessing removal of correlated errors in GRACE temporal gravity field solutions.” *Journal of Geodesy*. 83, 1095–1106. doi:10.1007/s00190-009-0327-0

Dyurgerov, M.B., Meier, M.F., 2005. “Glaciers amd the Changing Earth System: A 2004 Snapshot.” *Boulder:Institute of Arctic and Alpine Research, University of Colorado*.

Erten, E., Reigber, A., Hellwich, O., Prats, P., 2009. “Glacier velocity monitoring by maximum likelihood texture tracking.” *IEEE Transactions on Geoscience and Remote Sensing*. 47(2), 394–405. doi:10.1109/TGRS.2008.2009932

ESA. 2007. “ENVISAT RA2/MWR Product Handbook.”

Espizua, L.E., 2010. “Fluctuations of the Rio Del Plomo Glaciers.” *Geografiska Annaler: Series A, Physical Geography*. 68, 317–327.

Farinotti, D., Brinkerhoff, D.J., Clarke, G.K.C., Fürst, J.J., Frey, H., Gantayat, P., Gillet-Chaulet, F., Girard, C., Huss, M., Leclercq, P.W., Linsbauer, A., Machguth, H., Martin, C., Maussion, F., Morlighem, M., Mosbeux, C., Pandit, A., Portmann, A., Rabatel, A., Ramsankaran, R., Reerink, T.J., Sanchez, O., Stentoft, P.A., Singh Kumari, S., Van Pelt, W.J.J., Anderson, B., Benham, T., Binder, D., Dowdeswell, J.A., Fischer, A., Helfricht, K., Kutuzov, S., Lavrentiev, I., McNabb, R., Hilmar Gudmundsson, G., Li, H., Andreassen, L.M., 2017. “How accurate are estimates of

glacier ice thickness? Results from ITMIX, the Ice Thickness Models Intercomparison eXperiment.” *Cryosphere.* 11, 949–970. doi:10.5194/tc-11-949-2017

Farinotti, D., Huss, M., Bauder, A., Funk, M., Truffer, M., 2009. “A method to estimate the ice volume and ice-thickness distribution of alpine glaciers.” *Journal of Glaciology*. 55, 422–430. doi:10.3189/002214309788816759

Finsterwalder, S., 1897a. “Mechanische Beziehungen bei der Flächen-Deformation.” *Jahresbericht der Dtsch. Math*.

Finsterwalder, S., 1897b. “Die geometrischen Grundlagen der Photogrammetrie.” *Jahresbericht der Deutschen Mathematiker-Vereinigung.* 6, 43-90.

Fowler, A.C., 2011. “Weertman, Lliboutry and the development of sliding theory.” *Journal of Glaciology*. 56, 965–972. doi:10.3189/002214311796406112

Frey, H., Machguth, H., Huss, M., Huggel, C., Bajracharya, S., Bolch, T., Kulkarni, A., Linsbauer, A., Salzmann, N., Stoffel, M., 2014. “Estimating the volume of glaciers in the Himalayan–Karakoram region using different methods.” *Cryosphere*. 8, 2313–2333. doi:10.5194/tc-8-2313-2014

Gabbi, J., Farinotti, D., Bauder, A., Maurer, H., 2012. “Ice volume distribution and implications on runoff projections in a glacierized catchment.” *Hydrology and Earth System Sciences*. 16, 4543–4556. doi:10.5194/hess-16-4543-2012

Gantayat, P., Kulkarni, A. V., Srinivasan, J., 2014. “Estimation of ice thickness using surface velocities and slope: Case study at Gangotri Glacier, India.” *Journal of Glaciology*. 60, 277–282. doi:10.3189/2014JoG13J078

Gao, J., Liu, Y., 2001. “Applications of remote sensing, GIS and GPS in glaciology: a

review.” *Progress in Physical Geography*. 25, 520–540. doi:10.1177/030913330102500404

Gardelle, J., Berthier, E., Arnaud, Y., 2012. “Slight mass gain of Karakoram glaciers in the early twenty-first century.” *Nature Geoscience*. 5, 322–325. doi:10.1038/ngeo1450

Gardelle, J., Berthier, E., Arnaud, Y., Kääb, A., 2013. “Region-wide glacier mass balances over the Pamir-Karakoram-Himalaya during 1999–2011.” *Cryosphere*. 7, 1263–1286. doi:10.5194/tc-7-1263-2013

Gardner, A.S., Moholdt, G., Cogley, J.G., Wouters, B., Arendt, A.A., Wahr, J., Berthier, E., Hock, R., Pfeffer, W.T., Kaser, G., Ligtenberg, S.R., Bolch, T., Sharp, M.J., Hagen, J.O., van den Broeke, M.R., Paul, F., 2013. “A reconciled estimate of glacier contributions to sea level rise: 2003 to 2009.” *Science*. 340, 852–857. doi:10.1126/science.1234532

Gärtner-Roer, I., Naegeli, K., Huss, M., Knecht, T., Machguth, H., Zemp, M., 2014. “A database of worldwide glacier thickness observations.” *Global and Planetary Change*. doi:10.1016/j.gloplacha.2014.09.003

Geruo, A., Wahr, J., Zhong, S., 2013. “Computations of the viscoelastic response of a 3-D compressible earth to surface loading: An application to glacial isostatic adjustment in Antarctica and Canada.” *Geophysical Journal International*. 192, 557–572. doi:10.1093/gji/ggs030

Glen, J.W., 1959. “The flow law of ice: A discussion of the assumptions made in glacier theory, their experimental foundations and consequences.” *IASH Publ*. 47(171), e183.

Goldstein, R.M., Engelhardt, H., Kamb, B., Frolich, R.M., 1993. “Satellite radar interferometry for monitoring ice sheet motion: application to an Antarctic ice stream.” *Science*. 262, 1525–1530. doi:10.1126/science.262.5139.1525

Gudmundsson, G.H., 1999. “A three-dimensional numerical model of the confluence area of Unteraargletscher, Bernese Alps, Switzerland.” *Journal of Glaciology*. 45, 219–230. doi:10.3189/002214399793377086

Guo, J.Y., Duan, X.J., Shum, C.K., 2010. “Non-isotropic Gaussian smoothing and leakage reduction for determining mass changes over land and ocean using GRACE data.” *Geophysical Journal International*. 181, 290–302. doi:10.1111/j.1365-246X.2010.04534.x

Haeberll, W., Hoelzle, M., 1995. “Application of inventory data for estim . ating characteris - tics of and regional climate-change effects on mountain glaciers : a pilot study with the European Alps.” *Annals of Glaciology*. 21, 206–212. doi:10.3198/1995AoG21-1-206-212

Heid, T., Kääb, A., 2012. “Evaluation of existing image matching methods for deriving glacier surface displacements globally from optical satellite imagery.” *Remote Sensing of Environment*. 118, 339–355. doi:10.1016/j.rse.2011.11.024

Hock, R., 2005. “Glacier melt: a review of processes and their modelling.” *Progress in Physical Geography*. 29, 362–391. doi:10.1191/0309133305pp453ra

Hooke, R.L., 2005. “Principles of glacier mechanics.” *Cambridge University Press*. doi:10.1017/CBO9781107415324.004

Hooke, R.L., 1981. “Flow law for polycrystalline ice in glaciers: Comparison of theoretical predictions, laboratory data, and field measurements.” *Reviews of*

Geophysics. 19, 664–672. doi:10.1029/RG019i004p00664

Howat, I.M., Box, J.E., Ahn, Y., Herrington, A., McFadden, E.M., 2010. "Seasonal variability in the dynamics of marine-terminating outlet glaciers in Greenland." *Journal of Glaciology*. 56, 601–613. doi:10.3189/002214310793146232

Howat, I.M., Joughin, I., Tulaczyk, S., Gogineni, S., 2005. "Rapid retreat and acceleration of Helheim Glacier, east Greenland." *Geophysical Research Letters*. 32, 1–4. doi:10.1029/2005GL024737

Huang, M., 1990. "On the temperature distribution of glaciers in China." *Journal of Glaciology*. 36, 210–216.

Hughes, T. P., Seligman, Gerald, 1939. "The Temperature, Melt Water Movement and Density Increase in the Névé of an Alpine Glacier." *Geophysical Journal International*. 4, 616–647. doi:10.1111/j.1365-246X.1939.tb02922.x

Huss, M., Farinotti, D., 2012. "Distributed ice thickness and volume of all glaciers around the globe." *Journal of Geophysical Research: Earth Surface*. 117, 1–10. doi:10.1029/2012JF002523

Ingvaldsen, R.B., Asplin, L., Loeng, H., 2004. "Velocity field of the western entrance to the Barents Sea." *Journal of Geophysical Research: Oceans*. 109, 1–12. doi:10.1029/2003JC001811

Jacob, T., Wahr, J., Pfeffer, W.T., Swenson, S., 2012. "Recent contributions of glaciers and ice caps to sea level rise." *Nature.* 482, 514–518. doi:10.1038/nature10847

Joughin, I., 2002. "Ice-sheet velocity mapping: A combined interferometric and speckle-tracking approach." *Annals of Glaciology*. 34, 195–201. doi:10.3189/172756402781817978

Joughin, I., Abdalati, W., Fahnestock, M., 2004. “Large fluctuations in speed on Greenland’s Jakobshavn Isbræ glacier.” *Nature*. 432, 608–610. doi:10.1038/nature03130

Joughin, I., Smith, B.E., Howat, I.M., Scambos, T., Moon, T., 2010. “Greenland flow variability from ice-sheet-wide velocity mapping.” *Journal of Glaciology*. 56, 415–430. doi:10.3189/002214310792447734

Joughin, I., Tulaczyk, S., Fahnestock, M., Kwok, R., 1996. “A Mini-Surge on the Ryder Glacier, Greenland, Observed by Satellite Radar Interferometry.” *Science*. 274, 228–230. doi:10.1126/science.274.5285.228

Kääb, A., Berthier, E., Nuth, C., Gardelle, J., Arnaud, Y., 2012. “Contrasting patterns of early twenty-first-century glacier mass change in the Himalayas.” *Nature*. 488, 495–498. doi:10.1038/nature11324

Kääb, A., Treichler, D., Nuth, C., Berthier, E., 2015. “Brief Communication: Contending estimates of 2003-2008 glacier mass balance over the Pamir-Karakoram-Himalaya.” *Cryosphere.* 9, 557–564. doi:10.5194/tc-9-557-2015

Kamb, B., Echelmeyer, K.A., 1986. “Stress-Gradient Coupling in Glacier Flow: 1. Longitudinal Averaging of the Influence of Ice Thickness and Surface Slope.” *Journal of Glaciology*. 32, 267–284.

Kehrwald, N.M., Thompson, L.G., Tandong, Y., Mosley-Thompson, E., Schotterer, U., Alfimov, V., Beer, J., Eikenberg, J., Davis, M.E., 2008. “Mass loss on himalayan glacier endangers water resources.” *Geophysical Research Letters*. 35, L22503. doi:10.1029/2008GL035556

Knight, P.G., 1992. “Glaciers.” *Progress in Physical Geography*. 16, 85–89.

Krabill, W.B., Thomas, R.H., Martin, C.F., Swift, R.N., Frederick, E.B., 1995. "Accuracy of airborne laser altimetry over the Greenland ice sheet." *International Journal of Remote Sensing*. 16, 1211–1222. doi:10.1080/01431169508954472

Krimmel, R.M., Meier, M.F., 1975. "Glacier applications of ERTS images." *Journal of Glaciology*. 15, 391–402.

Laxon, S., 1994. "Sea ice altimeter processing scheme at the EODC." *International Journal of Remote Sensing*. 15, 915–924. doi:10.1080/01431169408954124

Lee, D.S., Storey, J.C., Choate, M.J., Hayes, R.W., 2004. "Four years of Landsat-7 on-orbit geometric calibration and performance." *IEEE Transactions on Geoscience and Remote Sensing*. 42, 2786–2795. doi:10.1109/TGRS.2004.836769

Lee, H., Shum, C.K., Howat, I.M., Monaghan, A., Ahn, Y., Duan, J., Guo, J.Y., Kuo, C.Y., Wang, L., 2012. Continuously accelerating ice loss over Amundsen Sea catchment, West Antarctica, revealed by intLee, H., Shum, C. K., Howat, I. M., Monaghan, A., Ahn, Y., Duan, J., Guo, J., Kuo, C., Wang, L. 2012. "Continuously accelerating ice loss over Amundsen Sea catchment, West Antarctica, revealed by integrating altimetry and GRACE data." *Earth and Planetary Science Letters*. 321–322, 74–80. doi:10.1016/j.epsl.2011.12.040

Lee, H., Shum, C.K., Tseng, K.H., Huang, Z., Sohn, H.G., 2013. "Elevation changes of bering glacier system, Alaska, from 1992 to 2010, observed by satellite radar altimetry." *Remote Sensing of Environment*. 132, 40–48. doi:10.1016/j.rse.2013.01.007

Lee, H., Shum, C.K., Yi, Y., Braun, A., Kuo, C.Y., 2008. "Laurentia crustal motion observed using TOPEX/POSEIDON radar altimetry over land." *Journal of*

Geodynamics. 46, 182–193. doi:10.1016/j.jog.2008.05.001

Legrésy, B., Rémy., F., 1997. "Surface characteristics of the arctarctic ice sheet and altimetric observations." *Journal of Glaciology*. 143, 265–275.

Linsbauer, A., Paul, F., Haeberli, W., 2012. "Modeling glacier thickness distribution and bed topography over entire mountain ranges with glabtop: Application of a fast and robust approach." *Journal of Geophysical Research: Earth Surface*. 117, 1–17. doi:10.1029/2011JF002313

Linsbauer, A., Paul, F., Hoelzle, M., Frey, H., Haeberli, W., 2009. "The Swiss Alps without glaciers -- a GIS-based modelling approach for reconstruction of glacier beds". *Proceedings of Geomorphometry 2009.* 243–247. doi:10.5167/uzh-27834

Loewe, F., 1935. "The exploration of the greenland ice-cap, 1929-1934." *Scottish Geographical Magazine*. 51, 347–353. doi:10.1080/00369223508734989

MacDonald, W.R., 1976. "Glaciology in Antarctica." *ERTS-1, a New Window on Our Planet.* 194–195.

Manley, G., Ahlmann, H.W., 2006. "Glaciological Research on the North Atlantic Coasts: A ReviewGlaciological Research on the North Atlantic Coasts." *Geographical Review*. 39, 136. doi:10.2307/211163

Matsuo, K., Heki, K., 2013. "Current ice loss in small glacier systems of the arctic islands (iceland, svalbard, and the russian high arctic) from satellite gravimetry." *Terrestrial, Atmospheric and Oceanic Sciences*. 24, 657–670. doi:10.3319/TAO.2013.02.22.01

Matsuo, K., Heki, K., 2010. "Time-variable ice loss in Asian high mountains from satellite gravimetry." *Earth and Planetary Science Letters*. 290, 30–36.

doi:10.1016/j.epsl.2009.11.053

McNabb, R.W., Hock, R., O'Neel, S., Rasmussen, L.A., Ahn, Y., Braun, M., Conway, H., Herreid, S., Joughin, I., Pfeffer, W.T., Smith, B.E., Truffer, M., 2012. "Using surface velocities to calculate ice thickness and bed topography: A case study at Columbia Glacier, Alaska, USA." *Journal of Glaciology*. 58, 1151–1164. doi:10.3189/2012JoG11J249

Meier, M.F., Dyurgerov, M.B., Rick, U.K., O'Neel, S., Pfeffer, W.T., Anderson, R.S., Anderson, S.P., Glazovsky, A.F., 2007. "Glaciers Dominate Eustatic Sea-level Rise in the 21st Century." *Science*. 317, 1064–1067. doi:10.1126/science.1143906

Melkonian, A.K., Willis, M.J., Pritchard, M.E., Stewart, A.J., 2016. "Recent changes in glacier velocities and thinning at Novaya Zemlya." *Remote Sensing of Environment*. 174, 244–257. doi:10.1016/j.rse.2015.11.001

Moholdt, G., Nuth, C., Hagen, J.O., Kohler, J., 2010. "Recent elevation changes of Svalbard glaciers derived from ICESat laser altimetry." *Remote Sensing of Environment*. 114, 2756–2767. doi:10.1016/j.rse.2010.06.008

Moholdt, G., Wouters, B., Gardner, A.S., 2012. "Recent mass changes of glaciers in the Russian High Arctic." *Geophysical Research Letters*. 39(10). doi:10.1029/2012GL051466

Mohr, J., Reeh, N., Madsen, S.N., 1998. "Three-dimensional glacial flow and surface elevation measured with radar interferometry." *Nature*. 39, 273–276. doi:10.1038/34635

Morlighem, M., Rignot, E., Seroussi, H., Larour, E., Ben Dhia, H., Aubry, D., 2011. "A mass conservation approach for mapping glacier ice thickness." *Geophysical*

Research Letters. 38, n/a-n/a. doi:10.1029/2011GL048659

Neckel, N., Kropáček, J., Bolch, T., Hochschild, V., 2014. "Glacier mass changes on the Tibetan Plateau 2003–2009 derived from ICESat laser altimetry measurements." *Environmental Research Letters*. 9, 014009. doi:10.1088/1748-9326/9/1/014009

Nuth, C., Kääb, A., 2011. "Co-registration and bias corrections of satellite elevation data sets for quantifying glacier thickness change." *Cryosphere*. 5, 271–290. doi:10.5194/tc-5-271-2011

Nye, J.F., 1965. "The flow of a glacier in a channel of rectangular, elliptic or parabolic cross-section." *Journal of Glaciology*. 5, 661–690.

Nye, J.F., 1952. "The mechanics of glacier flow." *Journal of Glaciology*. 2, 82–93. doi:10.3198/1952JoG2-12-82-93

Oerlemans, J., Fortuin, J.P.F., 1992. "Sensitivity of Glaciers and Small Ice Caps to Greenhouse Warming." *Science*. 258, 115–117. doi:10.1126/science.258.5079.115

Ohmura, A., 2006. "Changes in mountain glaciers and ice caps during the 20th century." *Annals of Glaciology*. 43, 361–368. doi:10.3189/172756406781812212

Oziel, L., Sirven, J., 2011. "The Barents Sea polar front and water mases." *Ocean Science Discussions*. 1–39.

Paul, F., Bolch, T., Kääb, A., Nagler, T., Nuth, C., Scharrer, K., Shepherd, A., Strozzi, T., Ticconi, F., Bhambri, R., Berthier, E., Bevan, S., Gourmelen, N., Heid, T., Jeong, S., Kunz, M., Lauknes, T.R., Luckman, A., Merryman Boncori, J.P., Moholdt, G., Muir, A., Neelmeijer, J., Rankl, M., VanLooy, J., Van Niel, T., 2015. "The glaciers climate change initiative: Methods for creating glacier area, elevation change and velocity products." *Remote Sensing of Environment*. 162, 408–426.

doi:10.1016/j.rse.2013.07.043

Paul, F., Haeberli, W., 2008. “Spatial variability of glacier elevation changes in the Swiss Alps obtained from two digital elevation models.” *Geophysical Research Letters*. 35, L21502. doi:10.1029/2008GL034718

Paul, F., Linsbauer, A., 2012. “Modeling of glacier bed topography from glacier outlines, central branch lines, and a DEM.” *International Journal of Geographical Information Science*. 26, 1173–1190. doi:10.1080/13658816.2011.627859

Pfeffer, W.T., Harper, J.T., O’Neel, S., 2008. “Kinematic Constraints on Glacier Contributions to 21st-Century Sea-Level Rise.” *Science*. 321, 1340–1343. doi:10.1126/science.1159099

Rabatel, A., Sanchez, O., Vincent, C., Six, D., 2018. “Estimation of Glacier Thickness From Surface Mass Balance and Ice Flow Velocities: A Case Study on Argentière Glacier, France.” *Frontiers in Earth Science*. 6, 1–16. doi:10.3389/feart.2018.00112

Radić, V., Bliss, A., Beedlow, A.C., Hock, R., Miles, E., Cogley, J.G., 2014. “Regional and global projections of twenty-first century glacier mass changes in response to climate scenarios from global climate models.” *Climate Dynamics*. 42, 37–58. doi:10.1007/s00382-013-1719-7

Ramillien, G., Bouhours, S., Lombard, A., Cazenave, A., Flechtner, F., Schmidt, R., 2008. “Land water storage contribution to sea level from GRACE geoid data over 2003-2006.” *Global and Planetary Change*. 60, 381–392. doi:10.1016/j.gloplacha.2007.04.002

Rignot, E.J., 1997. “North and northeast Greenland ice discharge from satellite radar interferometry.” *Science*. 276, 934–937. doi:10.1126/science.276.5314.934

Sandford, K.S., Seligman, G., Loewe, F., Glen, A., Wright, J., Ahlmann, H.W., Odell, N.E., 2006. “Contribution to the Physics of Glaciers: Discussion.” *The Geographical Journal*. 86, 107. doi:10.2307/1786586

Scambos, T.A., Dutkiewicz, M.J., Wilson, J.C., Bindschadler, R.A., 1992. “Application of Image Cross-Correlation to the Measurement of Glacier Velocity Using Satellite Image Data.” *Remote Sensing of Environment*. 42, 177–186.

Scherler D., Wulf H., Gorelick N., 2018. Global Assessment of Supraglacial Debris-Cover Extents. *Geophysical Research Letters*. 45(21), 11798-11805.

Schutz, B.E., Zwally, H.J., Shuman, C.A., Hancock, D., DiMarzio, J.P., 2005. “Overview of the ICESat mission.” *Geophysical Research Letters*. doi:10.1029/2005GL024009

Sharov, A.I., 2005. “Studying changes of ice coasts in the European Arctic.” *Geo-Marine Letters*. 25, 153–166. doi:10.1007/s00367-004-0197-7

Skvarca, P., Raup, B., De Angelis, H., 2003. “Recent behaviour of Glaciar Upsala, a fast-flowing calving glacier in Lago Argentino, southern Patagonia.” *Annals of Glaciology*. 36, 184–188. doi:10.3189/172756403781816202

Strozzi, T., Kouraev, A., Wiesmann, A., Wegmüller, U., Sharov, A., Werner, C., 2008. “Estimation of Arctic glacier motion with satellite L-band SAR data.” *Remote Sensing of Environment*. 112, 636–645. doi:10.1016/j.rse.2007.06.007

Strozzi, T., Luckman, A., Murray, T., Wegmüller, U., Werner, C.L., 2002. “Glacier motion estimation using SAR offset-tracking procedures.” *IEEE Transactions on Geoscience and Remote Sensing*. 40, 2384–2391. doi:10.1109/TGRS.2002.805079

Sun, Z., Lee, H., Ahn, Y., Aierken, A., Tseng, K.H., Okeowo, M.A., Shum, C.K., 2017. “Recent Glacier Dynamics in the Northern Novaya Zemlya Observed by Multiple

Geodetic Techniques." *IEEE Journal of Selected Topics in Applied Earth Observations and Remote Sensing*. 10, 1290–1302. doi:10.1109/JSTARS.2016.2643568

Swenson, S., Chambers, D., Wahr, J., 2008. "Estimating geocenter variations from a combination of GRACE and ocean model output." *Journal of Geophysical Research: Solid Earth*. 113, B08410. doi:10.1029/2007JB005338

Van der Veen, C.J., 2013. "Fundamentals of glacier dynamics." *Journal of Glaciology*. doi:10.3189/2014JoG13J214

Van Pelt, W.J.J., Oerlemans, J., Reijmer, C.H., Pettersson, R., Pohjola, V.A., Isaksson, E., Divine, D., 2013. "An iterative inverse method to estimate basal topography and initialize ice flow models." *Cryosphere* 7, 987–1006. doi:10.5194/tc-7-987-2013

Vieli, A., Jania, J., Kolondra, L., 2002. "The retreat of a tidewater glacier: Observations and model calculations on Hansbreen, Spitsbergen." *Journal of Glaciology*. 48, 592–600. doi:10.3189/172756502781831089

Williams, R.S., Bodvarsson, A., Rist, S., Saemundsson, K., Thorarinsson, S., 1975. "Glaciological studies in iceland with Erts-I imagery." *Journal of Glaciology*. 15, 465–466. doi:10.3189/S0022143000034638

Wingham, D.J., Rapley, C., H D, G., 1986. "New Techniques in Satellite Tracking Systems." *IGARSS '86 Symposium Digest 1:185-190, September in Zurich, Switzerland*. 1339–1344.

Wingham, D.J., Ridout, A.J., Scharroo, R., Arthern, R.J., Shum, C.K., 1998. "Antarctic elevation change from 1992 to 1996." *Science*. 282, 456–458. doi:10.1126/science.282.5388.456

World Resources Institute, 2003. “Watersheds of the World.” New York.

Wulf, H., Bookhagen, B., Scherler, D., 2016. “Differentiating between rain, snow, and glacier contributions to river discharge in the western Himalaya using remote-sensing data and distributed hydrological modeling.” *Advances in Water Resources*. 88, 152–169. doi:10.1016/j.advwatres.2015.12.004

Yi, S., Sun, W., 2014. “Evaluation of glacier changes in high-mountain Asia based on 10 year GRACE RL05 models.” *Journal of Geophysical Research: Solid Earth.* 119, 2504–2517. doi:10.1002/2013jb010860

Zemp, M., Thibert, E., Huss, M., Stumm, D., Rolstad Denby, C., Nuth, C., Nussbaumer, S.U., Moholdt, G., Mercer, A., Mayer, C., Joerg, P.C., Jansson, P., Hynek, B., Fischer, A., Escher-Vetter, H., Elvehøy, H., Andreassen, L.M., 2013. “Reanalysing glacier mass balance measurement series.“ *Cryosphere*. 7, 1227–1245. doi:10.5194/tc-7-1227-2013

Zemp, M., Huss, M., Thibert, E., Eckert, N., McNabb, R., Huber, J., Barandun, M., Machguth, H., Nussbaumer, S.U., Gärtner-Roer, I., Thomson, L., Paul, F., Maussion, F., Kutuzov S., Cogley, J.G., 2019. "Global glacier mass changes and their contributions to sea-level rise from 1961 to 2016." *Nature*. 1.

Zhang, G., Yao, T., Xie, H., Kang, S., Lei, Y., 2013. “Increased mass over the Tibetan Plateau: From lakes or glaciers.” *Geophysical Research Letters*. 40, 2125–2130. doi:10.1002/grl.50462

Zhao, L., Ding, R., Moore, J.C., 2016. “The High Mountain Asia glacier contribution to sea-level rise from 2000 to 2050.” *Annals of Glaciology*. 57, 223–231. doi:10.3189/2016AoG71A049

Zhao, M., Ramage, J., Semmens, K., Obleitner, F., 2014. “Recent ice cap snowmelt in Russian High Arctic and anti-correlation with late summer sea ice extent.” *Environmental Research Letters*. 9, 045009. doi:10.1088/1748-9326/9/4/045009